FEDERAL UNIVERSITY OF TECHNOLOGY - PARANÁ
GRADUATE PROGRAM IN ELECTRICAL AND COMPUTER ENGINEERING

ACÁCIO JOSÉ ZIMBICO

BAYESIAN-BASED BEAMFORMER WITH WIENER POST-FILTER FOR ADAPTIVE PROCESSING OF ULTRASOUND IMAGE USING COHERENT PLANE WAVE COMPOUNDING

THESIS

CURITIBA

2018

ACÁCIO JOSÉ ZIMBICO

BAYESIAN-BASED BEAMFORMER WITH WIENER POST-FILTER FOR ADAPTIVE PROCESSING OF ULTRASOUND IMAGE USING COHERENT PLANE WAVE COMPOUNDING

Thesis presented to the Graduate Program in Electrical and Computer Engineering of the Federal University of Technology - Paraná as a requirement for obtaining the degree of PhD – Concentration Area: Biomedical Engineering.

Supervisor: Prof. Dr. Fabio Kurt Schneider

Co-supervisor: Prof. Dr. Joaquim Miguel Maia

CURITIBA

2018

Dados Internacionais de Catalogação na Publicação

Z71b Zimbico, Acácio José
Bayesian-based beamformer with Wiener post-filter for adaptive processing of ultrasound image using coherent plane wave compounding / Acácio José Zimbico.-- 2018.
107 f.: il.

Disponível via World Wide Web.
Texto em inglês com resumo em português.
Tese (Doutorado) - Universidade Tecnológica Federal do Paraná. Programa de Pós-Graduação em Engenharia Elétrica e Informática Industrial. Área de Concentração: Engenharia Biomédica, Curitiba, 2018.
Bibliografia: f. 96-102.

1. Engenharia elétrica - Teses. 2. Ultrassom - Qualidade da imagem. 3. Processamento de sinal adaptativo. 4. Processamento de imagens - Modelos matemáticos. 5. Teoria bayesiana de decisão estatística. 6. Beamforming. 7. Filtros adaptativos. 8. Speckle. 9. Imagem de alta resolução. 10. Métodos de simulação. I. Schneider, Fábio Kurt, orient. II. Maia, Joaquim Miguel, coorient. III. Universidade Tecnológica Federal do Paraná. Programa de Pós-graduação em Engenharia Elétrica e Informática Industrial. IV. Título.

CDD: Ed. 23 -- 621.3

Biblioteca Central do Câmpus Curitiba – UTFPR
Bibliotecária: Luiza Aquemi Matsumoto CRB-9/794

Ministério da Educação
Universidade Tecnológica Federal do Paraná
Diretoria de Pesquisa e Pós-Graduação

TERMO DE APROVAÇÃO DE TESE Nº184

A Tese de Doutorado intitulada **"Bayesian-based Beamformer With Wiener Post-filter for Adaptive Processing of Ultrasound Image Using Coherent Plane Wave Compounding",** defendida em sessão pública pelo(a) candidato(a) **Acácio José Zimbico**, no dia 07 de dezembro de 2018, foi julgada para a obtenção do título de Doutor em Ciências, área de concentração Engenharia Biomédica, e aprovada em sua forma final, pelo Programa de Pós-Graduação em Engenharia Elétrica e Informática Industrial.

BANCA EXAMINADORA:

Prof(a). Dr(a). Fabio Kurt Schneider - Presidente – (UTFPR)
Prof(a). Dr(a). Altair Olivo Santin – (PUC-PR)
Prof(a). Dr(a). Amauri Amorin Assef – (UTFPR)
Prof(a). Dr(a). Solivan Arantes Valente – (UP)
Prof(a). Dr(a). Giselle Lopes Ferrari Ronque - (UFPR)

A via original deste documento encontra-se arquivada na Secretaria do Programa, contendo a assinatura da Coordenação após a entrega da versão corrigida do trabalho.

Curitiba, 07 de dezembro de 2018.

ACKNOWLEDGEMENT

I would like to thank my thesis advisor and co-advisor Prof. Dr. Fabio Kurt Schneider and Prof. Dr. Joaquim Miguel Maia, respectively, for the support of my investigation. They gave me the opportunity to develop research. They steered me the right direction whenever I needed.

Also, I would like to express my gratitude:

To all professors who helped me.

To my research team, Nivaldo Jr., Amauri Assef and Diogo Granado for their collaboration.

To my lab-colleagues, Eduardo Tondin, Charles Fung, Fabio Hadano, Ricardo Fantin da Costa, Flavio Grando and others for helping me whenever I needed.

To all of the Department of Electrical Engineering (DEEL) of Eduardo Mondlane University (UEM).

To my compatriots, Kenedy Silvério, Narciso Bila, Ivenso Sualehe for the coexistence and friendship we did.

To my parents Rosita João Muchave and José Benjamim Zimbico for continuous encouragement.

To all my brothers and friends.

This accomplishment would not have been possible without them. Finally, I would like to acknowledge to the CAPES and, the National Council for Scientific and Technological Development (CNPq) and Fundação Araucária do Paraná for the financial support.

ABSTRACT

Zimbico, Acácio José. BAYESIAN-BASED BEAMFORMER WITH WIENER POST-FILTER FOR ADAPTIVE PROCESSING OF ULTRASOUND IMAGE USING COHERENT PLANE WAVE COMPOUNDING. 107 f. Thesis – Graduate Program in Electrical and Computer Engineering, Federal University of Technology - Paraná. Curitiba, 2018.

Conventional Ultrasound (US) scanners still implement the non-adaptive Delay and Sum (DAS) technique due to easy implementation and low processing time, but it provides low resolution and image contrast. Adaptive techniques allow obtaining high resolution and high contrast at the cost of complex implementation and high processing time. In this work we suggest the implementation of a Bayesian Minimum Variance (MV-BY) beamformer combined with the Wiener post-filter (WPF) to form the MV-BY-WPF beamformer. The MV-BY-WPF results in a combination of the proposed Bayesian-based Minimum Variance (MV-BY) beamformer with the WPF for adaptive beamforming of US image using Coherent Plane Wave Compounding (CPWC). The CPWC imaging has low Signal-to-noise Ratio (SNR) due to the lack of focusing on the pulse emission. Different adaptive methods such Coherence Factor (CF) or WPF beamformer have been suggested to overcome such limitation, however they still present limitations. In this study, we have introduced the MV-BY beamformer which takes subtle advantages over the Minimum Variance (MV) beamformer by applying a Bayesian-based post-filter which improves the performance of the MV. The proposed MV-BY is combined with the WPF to form the MV-BY-WPF which outperforms the MV-WPF. The MV-BY-WPF provides better contrast while retaining the imaging brightness at comparable spatial resolution when compared to the beamformers such as the traditional MV-WPF. Using our proposed methods, improvements have been introduced in CPWC imaging with comparable computational complexity with the MV beamformer. The performance evaluation of the proposed techniques includes spatial resolution, contrast, and speckle statistics. Particular to our proposed methodology, we have found that approximately 5 emissions using available data for research in US imaging, we have reconstructed an image with quality comparable to that obtained when using a total amount of 75 emissions with DAS beamformer. The reconstructions using simulation, phantom, and *in-vivo* dataset reveal the effectiveness of our proposed beamformer in terms of array noise suppression abilities. For example, using human *in-vivo* data, when DAS is compared to the MV-BY/MV-BY-WPF values in percentage (%) of 9.34/17.65 and 16.18/31.79 for Contrast Ratio (CR) and Contrast-to-noise Ratio (CNR), were obtained. Additionally, the MV-BY-WPF better retains the speckle when compared to MV-WPF. This means that our proposed methodology can improve the imaging system, and is suggested for real applications.

Keywords: *Minimum* variance. Ultrasound imaging. Plane-wave compounding. Adaptive processing. Bayesian beamformer. Wiener post-filter.

RESUMO

Zimbico, Acácio José. BEAMFORMER BASEADO EM ABORDAGEM BAYESIANA COM O PÓS-FILTRO DE WIENER PARA PROCESSAMENTO ADAPTATIVO DE IMAGEM DE ULTRASSOM USANDO O MÉTODO DE ONDA PLANA COM COMPOSIÇÃO COERENTE. 107 f. Tese – Programa de Pós-Graduação em Engenharia Elétrica e Informática Industrial, Universidade Tecnológica Federal do Paraná. Curitiba, 2018.

Os escaneres de Ultrassom (US) convencionais ainda implementam a técnica *Delay and Sum* (DAS) devido à fácil implementação e baixo tempo de processamento, mas oferecem imagem de baixa resolução e contraste. As técnicas adaptativas permitem a obtenção de imagem de alta resolução e Contraste (CR) em troca de implementação complexa e custo de processamento elevado. Neste trabalho, sugere-se o método *Wiener Post-filter*(WPF) combinado com uma a técnica *Minimum Variance* (MV) com abordagem Bayesiana (i.e., MV-BY-WPF), que resulta em uma combinação do método proposto MV-BY com WPF para beamforming adaptativo de US usando a técnica *Coherent Plane Wave Compounding* (CPWC). A técnica CPWC é afetada por baixa SNR devido à ausência de foco na emissão de pulso. Diferentes beamformers adaptativos tais como, os baseados em *Coherence Factor* (CF) ou WPF foram sugeridos para superar tal limitação, entretanto limitações ainda persistem. Neste estudo, introduziu-se o MV-BY que mostra vantagens sutis sobre o MV através da aplicação de um pós-filtro baseado na abordagem Bayesiana que melhora o desempenho do MV. Combinou-se o método proposto, MV-BY com o WPF para formar o MV-BY-WPF, que supera MV-WPF. De acordo com os resultados, MV-BY-WPF oferece melhor CR enquanto retém o brilho de imagem na resolução comparada à oferecida por MV-WPF. Usando os métodos propostos, foram introduzidas melhorias em imagem usando CPWC com custo computacional comparável à do MV. A avaliação de desempenho das técnicas inclui a Resolução espacial, CR e as estatísticas de *speckle*. Em particular à metodologia proposta, verificou-se que com a excitação de cerca de 5 emissões, foi possível reconstruir uma imagem com qualidade comparável àquela obtida com um total de 75 emissões com o DAS. A reconstrução usando dados de simulação, *Phantom* e humanos *in-vivo* disponíveis na plataforma de US revelam a eficácia do *beamformer* proposto em termos de habilidades de supressão de ruído presente nos dados coletados. Por exemplo, usando dados humanos *in-vivo*, quando o DAS é comparado aos *beamformers* MV-BY/MV-BY-WPF, valores percentuais (%) de 9,34/17,65 e 16,18/31,79 para CR e a sua razão foram respectivamente obtidos. Além disso, as respostas produzidas por MV-BY-WPF mostram uma melhor preservação do *speckle* quando comparado com MV-WPF. Isso significa que a metodologia proposta pode melhorar o sistema de imagem sendo assim, sugerida para aplicações reais.

Palavras-chave: Variância mínima. Imagem de ultrassom. Composicão de onda plana. Processamento adaptativo. Beamformer Bayesiano. Pós-filtro de Wiener.

LIST OF FIGURES

Figure 1 – The representation of zones of compression and rarefaction created in a medium due to the propagation of a longitudinal acoustic waves, from left to right. 22
Figure 2 – Representation of the three major modes of scattering in tissue: (a) for specular reflection, (b) for diffusive scattering and, (c) for diffractive scattering. 25
Figure 3 – The cconfiguration and orientation with all the basic elements of a transducer array. 27
Figure 4 – The conventional scanning modes of two common transducer formats: (a) is the phased array transducer and (b) is the linear array transducer. The dashed arrows in both panels show the course of the scan. The vertical dashed lines indicate the plane wave transmission orientation for both cases: (c) for the phased array transducer and, (d) for the linear array transducer. 28
Figure 5 – Profile of focused ultrasound beam exhibiting the focal zones 30
Figure 6 – Example of beamforming schemas applying electronic delays: (a) for a flat planar-wave, (b) for an oriented planar-wave, (c) for a focused beam, and (d) for an oriented focused beam. 31
Figure 7 – Two examples of emitted plane-wave wavefronts. Panel (a) depicts the interference pattern of transmit pulses emitted simultaneously while Panel (b) illustrates the interference pattern of transmit pulses emitted with a linear time delay sequence to create an angled acquisition. 32
Figure 8 – Radiation pattern for fixed weighting windows (a) Using boxcar apodization and (b) using hamming apodization. 33
Figure 9 – The basic and general US image scanning process and image visualization. 34
Figure 10 – Materials and Methods: High-resolution Image (HRI) formation from a set of Low- resolution (LR) images in CPWC. 36
Figure 11 – Geometric representation of plane wave emmission and signal reception in coherent plane wave compounding. 37
Figure 12 – In subarray averaging a relatively larger array is the division into subarrays. The array is divided into (overlapping) subarrays of length L so that the spatial covariance matrices of the subarrays are averaged in order to decorrelate the array signals 40
Figure 13 – The MV beamformer diagram to medical US imaging. 41
Figure 14 – The Bayesian-based beamformer in the form of the postfilter scheme. This beamformer is used for designing the MV-BY-WPF. 49
Figure 15 – The experimental data acquiring infrastructure 52
Figure 16 – The scanning regions for multiporpose phantom 84-317 and 040GSE phantom used for experimental data acquiring 52
Figure 17 – The scanning regions covered by the linear transducer array 53
Figure 18 – Dataset from PICMUS for a total amount of 5 plane wave elements 55

Figure 19 – Ilustraction of FWHM, CR, CNR and speckle pattern evaluation. 58
Figure 20 – Ilustraction of theoretical pdf for speckle assesment. 60
Figure 21 – Images of simulated point-reflector phantom S1. 61
Figure 22 – The lateral profiles for PSF. 62
Figure 23 – Images of simulated anechoic cyst phantom S2 65
Figure 24 – Depiction of the lateral profiles using simulation data for S2. 66
Figure 25 – Beamformed images of phantom data PH1 containing hypoechoic cyst with point-reflectors. 67
Figure 26 – Beamformed images of anechoic cyst phantom data PH2. 70
Figure 27 – Beamformed images of human *in-vivo* cross sectional of a CA data H1. 73
Figure 28 – Beamformed images of human *in-vivo* longitudinal a CA data H2. 74
Figure 29 – The scanning regions (higlighted) used for speckle pattern evaluation. 79
Figure 30 – Images of simulated data and human *in-vivo* data for cross-sectional H1 and longitudinal H2 CA. 81
Figure 31 – Images of simulated anechoic cyst phantom S2. 84
Figure 32 – Images of phantom data PH1. 84
Figure 33 – Images of phantom data PH2. 84
Figure 34 – Images of human *in-vivo* longitudinal CA. 85
Figure 35 – Images of human *in-vivo* H2 data of cross sectional CA. 85
Figure 36 – The top row presents images acquired from Verasonics Imaging System for 75 plane wave emissions and beamformed with DAS, while the midle row presents images acquired from Verasonics Imaging System for only 5 plane wave emissions and beamformed with DAS with the abovementioned sequence. Analogously, the last row presents images acquired from Verasonics Imaging System for 5 plane wave emissions and beamformed with MV-BY-WPF following the the abovementioned sequence. 86

LIST OF TABLES

Table 1 – Speed of ultrasound c, acoustic impedance Z, and attenuation coefficients α for different materials (SZABO, 2004b). 23
Table 2 – The Bayesian minimum variance (MV-BY) beamformer algorithm 50
Table 3 – Dataset presentation for evaluation of the proposed methodology 54
Table 4 – Important parameters for simulated and experimental (real phantom and *in-vivo*) for acquisition and data processing. 56
Table 5 – Spatial resolution ($FWHM_{ax}$, $FWHM_{lat}$) for simulated S1. 62
Table 6 – Contrast CR and CNR for simulated S2 data. 65
Table 7 – Spatial resolution ($FWHM_{ax}$, $FWHM_{lat}$) for phantom data PH1 67
Table 8 – Spatial resolution ($FWHM_{ax}$, $FWHM_{lat}$) for phantom data PH2 70
Table 9 – Contrast (CR, CNR) for phantom data acuired using phantom 84-317 ... 72
Table 10 – Contrast (CR) and Contrast to noise ratio (CNR) for *in-vivo* data 75
Table 11 – CR and CNR for different Plane Wave Emissions (PWE) using S2 77
Table 12 – The CR and CNR for DAS beamformer 75, DAS beamformer 5 and MV-BY beamformer 5 for phantom and *in-vivo* data 77
Table 13 – The SNR for different beamformer using S2, H1 and H2 dataset 80
Table 14 – Speckle pattern produced by different adaptive beamformers taking DAS as reference 82
Table 15 – The peaks of Rayleigh pdf and Normalized intensity in dB for differente beamformers. 83

LIST OF ACRONYMS

BS	Beamspace
BR	Beam Responses
CA	Carotid artery
CC	Computational complexity
CF	Coherence factor
CM	Covariance matrix
CNR	Contrast-to-noise ratio
CPWC	Coherent plane wave compounding
CR	Contrast
CS	Coherent sum
DAS	Delay-and-sum
DL	Diagonal loading
DMAS	Delay multiply and sum
DMR	Dominant mode rejection
DR	Dynamic Range
DS	Desired signal
DSI	Desired signal of interest
EGSC	Eigenspace generalized sidelobe canceller
EMV	Eigenspace minimum variance
FWHM	Full Width at Half Maximum
$FWHM_{ax}$	FWHM in axial direction
$FWHM_{lat}$	FWHM in lateral direction
FO	Floating operations
GPU	Graphic processing unity
GSC	Generalized sidelobe canceller
H1	Human *in-vivo* data for cross-sectional CA
H2	Human *in-vivo* data for longitudinal CA
HRI	High-resolution image
IS	Incoherent sum
LRI	Low-resolution images
MAP	Maximum *a posteriori*
MMSE	Minimum mean squared error
MV	Minimum variance
MV-BY	Minimum variance combined with Bayesian based
MV-BY-WPF	Bayesian based MV combined with WPF beamformer
MV-WPF	Wiener pos-filter combined with MV
NE	Number of elements
NPICM	Noise plus interference covariance matrix
pdf	Probability density function
PH1	Phantom experimental data for resolution distortion
PH2	Phantom experimental data for contrast speckle

PICMUS	Plane Wave Challenge in Medical Ultrasound
PZT	Piezo-electric
RD	Rayleigh distribution
RF	Radio frequency
RTM	Random matrix theory
S1	Simulation phantom data for point reflector
S2	Simulation phantom data for speckle contrast
SIMU	Simulation mode
SNR	Signal-to-noise ratio
TRD	Theoretical Rayleigh distribution
US	Ultrasound
WPF	Wiener post-filter

LIST OF SYMBOLS

ρ	Density of the medium
k_c	Compressibility of the medium
z_m	Acostic impedance of the medium
c	Speed of acoustic propagation
ρ	Density of the medium
R_c	Reflection coefficient
T_c	Transmission coefficient
Z_i	Impedance measures of the tissue medium before incident to the tissue boundary
Z_t	Impedance measures of the tissue medium after refracted by the tissue boundary
θ_i	Angle at which the incident wave approaches the tissue boundary
θ_t	Angle at which the refracted wave departs from the boundary
θ_r	Angles at which the reflected wave departs from the boundary
I	Amplitude of the intensity of the propagating wave
z	Depth traveled
f_0	Emitted central frequency
I_0	Amplitude of initial intensity of the propagating wave
α	Attenuation coefficient
F_n	F-number
D_b	Focal beam
D_f	Focal distance
λ	wavelength
c	Speed of sound in the medium
M	Number of elements in the transducer
N	Number of plane wave emissions
$\vec{u}$	Receive apodization window
$\vec{w}$	Angular apodization window
λ	Wavelength of the imaging system
A	Probe aperture
D_j	Travel distance in emission
D_r	Travel distance in reception
α_j	Travel distance
$(\bullet)^T$	Transpose
$(\bullet)^H$	Hermitian
E	Expectation operator
$\vec{a}$	Array steering vector
$\vec{w}$	Weight vector
R	Covariance matrix
$(\bullet)^{-1}$	Inverse operation
D	Number of temporal samples

S	Number of subarrays used in CM estimatin
Δ	Diagonal loading factor
L	Sub-rray length
X_l	Data submatrices used in data subarray averaging
$\vec{w}_{Wiener}$	Wiener beamformer
H_{Wiener}	Wiener post-filter
R_n	Noie plus-interference covariance matrix
$H_{MV\text{-}WPF}$	WPF applied to MV beamformer
$\vec{w}_{MV\text{-}WPF}$	MV-WPF weight vector
$z_{MV\text{-}WPF}$	MV-WPF beamformer output
L_k	Points in the imaging region in the axial direction
s	Desired signal
pdf	Probability density function
$p(\theta_i)$	*a priori* probability
K	Number of temporary samples used in CM estimation
σ_s^2	Noise plus interference signal power
σ_n^2	Desired signal power
$\mathscr{L}(\bullet)$	Lagrangian
λ_o	Lagrangian multiplier
$\nabla(\bullet)$	Gradient operator

TABLE OF CONTENTS

1 INTRODUCTION 15
1.1 RELATED WORKS 15
1.2 OBJECTIVES 19
1.3 THESIS OUTLINES 20
2 THEORETICAL FRAMEWORK 22
2.1 ULTRASOUND WAVE PROPAGATION 22
2.1.1 Acoustic impedance 23
2.1.2 Ultrasound wave and medium interaction 24
2.1.3 Attenuation 25
2.2 BASICS OF ULTRASOUND IMAGE ACQUISITION 26
2.2.1 Ultrasound transducer 26
2.2.2 The beam orientation 29
2.2.3 Plane-wave Ultrasound Emission 31
2.2.4 Apodization 32
2.2.5 The basic steps of image formation and visualization 32
2.3 BEAMFORMING THEORETICAL BACKGROUND 34
2.3.1 Coherent plane wave compounding 34
2.3.2 Minimum variance Beamformer 38
2.3.3 The Coherence Factor Beamforming 41
2.3.4 The Wiener post-filter Beamforming 42
2.4 THE BAYESIAN-BASED BEAMFORMER FOR ARBITRARY ARRAY ADAPTIVE SIGNAL PROCESSING 44
3 THE PROPOSED METHOD 47
3.1 THE MV-BY-WPF IMPLEMENTATION PROCEDURE 50
3.2 EVALUATION PROCEDURES 51
3.2.1 Dataset 51
3.2.1.1 Simulation and phantom data acquired on Laboratory 51
3.2.1.2 Simulation and phantom data available on PICMUS platform 53
3.2.1.3 Human *in-vivo* data available on PICMUS platform 53
3.2.2 Comparison between different beamformers 54
3.2.3 Details for adaptive processing 56
3.2.4 Experimental evaluation setup 57
3.3 EVALUATION METRICS 57
3.3.1 Spatial resolution 57
3.3.2 Contrast 58
3.3.3 Speckle statistics 58
4 RESULTS 61
4.1 RESULTS FOR SIMULATION PHANTOM DATA FOR POINT REFLECTORS (S1) 61
4.2 RESULTS FOR SIMULATION DATA FOR ANECHOIC CYST (S2) 64
4.3 RESULTS FOR PHANTOM DATA PH1 66

4.4 RESULTS FOR PHANTOM DATA (PH2) AND 84-317 69
4.4.1 Results for phantom data (PH2) 69
4.4.2 Results for phantom data acquired on Laboratory using phantom model 84-317 71
4.5 RESULTS FOR HUMAN *IN-VIVO* DATA (H1) AND (H2) 72
4.6 SPECKLE STATISTICS 78
4.6.1 Speckle statistics for S2 78
4.6.2 Speckle statistics for H1 and H2 79
4.6.3 Qualitative evaluation using displayed images: Data from PICMUS platform 83
4.6.4 Qualitative evaluation using displayed images: Dataset collected on US Laboratory. 85
5 DISCUSSION 87
5.1 SPATIAL RESOLUTION 88
5.2 CR AND CNR 90
5.3 SPECKLE STATISTICS 91
5.4 COMPUTATIONAL COMPLEXITY EVALUATION 92
6 CONCLUSIONS AND REMARKS 94
6.1 CONCLUSIONS 94
6.2 FUTURE WORKS 95
REFERENCES 96
Appendix A – THE MV BEAMFORMER SOLUTION 103
Appendix B – THE WIENER BEAMFORMER SOLUTION 105
Appendix C – THE EXTENDED WIENER BEAMFORMER SOLUTION 106

1 INTRODUCTION

The high-resolution multi-modalities medical imaging such as ultrasound is of great importance by making the basis for the development of different imaging applications.

In recent years the impact introduced by improvements in diagnosis using ultrasound image of high quality has gained significant visibility (MEHDIZADEH et al., 2012; NGUYEN; PRAGER, 2016a).

The high-quality ultrasound image is considered as a propedeutic method for evaluation of different structures and has been increasing (HEDRICK et al., 2005). This fact is mainly due to the technological development of real-time instrumentation, equipped with high-frequency transducers with optimal spatial resolution and development of new imaging applications (HEDRICK et al., 2005).

The beamforming techniques represent one of the primary step implemented by the commercially available scanners and serves as reference for comparing the image quality for different applications (HEDRICK et al., 2005).

1.1 RELATED WORKS

Medical ultrasonic imaging is a noninvasive and low-cost technology widely used for diagnosis (SZABO, 2004b). Research in ultrasound plane-wave imaging is gaining special attention in recent years due to the fact it represents a proper method for realization of high imaging frame rate Garcia et al. (2013), Cheng and Lu (2006) which benefits several imaging applications (TANTER; FINK, 2014; SANDRIN et al., 2002).

In practice, the high imaging frame rate of single plane wave firing element is performed at the cost of a poorer imaging quality if compared with the standard sequential line-by-line scanning procedure. One reason is that in plane wave imaging there is a lack of focusing in the beam transmission process (MONTALDO et al., 2009). However, several signals are collected with different steering angles representing a set of low-resolution images are used to compose a synthesized image with equivalent

imaging quality compared to the line-by-line mode.

The process of combining different signals collected with different steering angles is named as Coherent Plane Wave Compounding (CPWC) (TANTER; FINK, 2014; MONTALDO et al., 2009).

In order to enhance the imaging quality of the single plane wave firing element, one alternative resides on the application of adaptive processing over the collected dataset.

Adaptive processing differs from the traditional Delay-and-sum (DAS) beamformer, which uses a fixed window for array signal summation, by computing a set of data-dependent weight functions which are then combined with the input data to achieve a narrower main lobe and reduced side lobe energy.

Adaptive processing has been applied to ultrasound imaging. Its validation was due to its abilities in enhancing the imaging quality in terms of spatial resolution and contrast. This motivated the attempt of implementing the adaptive beamforming involving practical platforms for real-time imaging system (ÅSEN, 2014).

Among the main categories of adaptive beamformers the Minimum Variance (MV) based beamformers Synnevag et al. (2007), Holfort et al. (2009), Synnevag et al. (2009), Asl and Mahloojifar (2010) and the Coherence Factor (CF) based beamformers Li and Li (2003), Wang and Li (2009), Nilsen and Holm (2010) have been the most popularized for medical ultrasound imaging and recently have gained a different version, resulted from a special combination that explores their advantages.

The aim of the MV beamformer which was originally introduced by Capon in 1969 Capon (1969) is to minimize the output energy while keeping the desired signal undistorted. In the MV based beamformers the Covariance Matrix (CM) plays an important role in determining the performance of the algorithm (SYNNEVAG et al., 2007; HOLFORT et al., 2009; SYNNEVAG et al., 2009; ASL; MAHLOOJIFAR, 2010; LI; LI, 2003; WANG; LI, 2009; NILSEN; HOLM, 2010).

In the field of adaptive processing using the MV principle, different approaches have been suggested such as the Random Matrix Theory (RTM) whose principle consists of improving the array noise suppression abilities. In this method, the moments the eigenvalues and eigenvectors of the data CM are subject to spectral decomposition (MESTRE; LAGUNAS, 2008, 2008; YI et al., 2015).

In Beam-space (BS) based adaptive beamformers data is converted from array

space(which is larger) to beam-space (which is reduced by a specific factor) for further processing. The most interesting outcome of beam-space processing is achieving similar or high performance compared to array-space while reducing significantly the amount of time required for data processing (NILSEN; HAFIZOVIC, 2009; ZENG et al., 2013; DEYLAMI; ASL, 2017; ZIMBICO et al., 2017).

The Rank-reduced adaptive beamformers explore the eigen-decomposition of data CM in order to determine the signal and noise subspace. The Eigenspace Minimum Variance (EMV) Mehdizadeh et al. (2012), the Dominant Mode Rejection (DMR) Tracey et al. (2014), Cox and Pitre (1997), Zimbico et al. (2019) and the Eigenspace Generalized Sidelobe Canceller (EGSC) beamformers are the most representative beamformers and therefore, have been largely applied in the field of array signal processing and medical ultrasound imaging.

The EGSC however, is formulated using the Generalized Sidelobe Canceller (GSC) beamformer which corresponds to an improved representation of MV beamformer for array signal processing (GRIFFITHS; JIM, 1982; APPLEBAUM; CHAPMAN, 1976; YU; YEH, 1995; LI et al., 2016; WANG et al., 2017; ZIMBICO et al., 2017, 2018).

The Pixel-based beamformers have gained special attention in the field of ultrasound imaging, and have improved significantly the performance of the MV beamformer (NGUYEN; PRAGER, 2016a, 2017, 2016b).

The Wiener post-filter beamformers have been suggested to overcome the limitations of the CF-based approach in terms of SNR and have improved significantly the accuracy of the estimated signals compared to CF based approach (NILSEN; HOLM, 2010; WANG; LI, 2014; ZHAO et al., 2016).

The Spatial coherence together with the Bayesian beamformers belongs to class of adaptive beamformers which make the scope of this work.

Regarding the Bayesian based beamformers, two approaches have been commonly implemented in the field of array signal processing such as the Minimum Mean Squired Error (MMSE) principle and the Maximum *a posteriori* (MAP) (MAGILL, 1965; BELL et al., 1996, 2000; LAM; SINGER, 2006).

Efforts have been made in order to improve the performance of the MV beamformer by introducing different procedures on data CM estimation such as the spatial smoothing and diagonal loading (SYNNEVAG et al., 2007).

By definition, the CF based method represents the ratio between the coherent sum and the incoherent sum which has been interpreted as an assessment of the focusing quality Li and Li (2003) and is suggested to isolate the off-axis (additive noise) signal leading to the suppression of the noise and side lobes. The CF definition has been expanded by Li and Li (2003) which proposed the Generalized Coherence Factor (GCF).

Several studies have exploited the combination of the CF weighting with the MV-based beamformers resulting in improvements introduced in spatial resolution and contrast (ASL; MAHLOOJIFAR, 2009). A theoretical framework has been proposed by Nilsen and Holm (2010) to establish the link between the CF and the Wiener post-filter. Additionally, a Wiener post-filter could be used to modify the performance of MV based beamformer (NILSEN; HOLM, 2010; ZENG et al., 2012).

Zeng et al. have connected the Wiener beamformer with a version of MV beamformer and demonstrated its improvement in imaging resolution, contrast (ZENG et al., 2012).

The CF and Wiener post-filter is known to be effective in terms of sidelobe reduction but they also attenuate the signal power, which may originate the imaging artifacts or image degradation due to the on-axis (desired signal) signal cancellation (NILSEN; HOLM, 2010; ZENG et al., 2012). Another difficulty is that the output noise power in the Wiener post-filter is hard to estimate.

Different adaptive beamformers applicable to ultrasound plane wave imaging introduce improvements in terms of spatial resolution and contrast but their performances still impose a challenge to the research community.

Among different factors affecting the plane wave imaging performance, the low SNR originated from the lack of focusing on the pulse emission is pinpointed as representing the most impacting factor for the poorer imaging performance (ZHAO et al., 2015). As result, a poor signal coherence associated with low SNR of collected echo data degrades the image quality produced by the ultrasound plane wave imaging systems (ZHAO et al., 2016).

In the area of array signal processing, however, the Bayesian-based beamformer has shown to be accurate in signal estimation in different SNR scenarios (BELL et al., 1997a, 1996, 2000).

We believe that by combining the Bayesian-based beamformer with the

WPF we can introduce benefits in designing a version of Wiener post-filter based beamformer in order to improve the imaging performance.

By using Bayesian-based beamformer we expect to improve the imaging quality in terms of artifacts reduction by signal cancellation effect at low SNR while avoiding image degradation by signal self-cancellation effect at high SNR.

With the Bayesian-based beamformer, we expect improvements in image quality in terms of spatial resolution and contrast while preserving the weak image details such as the speckle pattern produced by the adaptive processing.

The Bayesian beamformer represents a post-filter method based on the *a posteriori* probability density function (pdf) coefficients obtained from dataset. These coefficients are combined with the MV beamformer output (BELL et al., 2000). An interesting aspect is that the Bayesian-based beamformer in the present formulation has never been presented in the area of ultrasound imaging.

In this work, we suggest a combination of the proposed Bayesian-based beamformer Bell et al. (2000) with the standard Wiener post-filter for adaptive processing using the MV beamformer as the reference in order to overcome the limitation of the MV, the MV-CF and the MV-WPF beamformers in terms of spatial resolution, contrast and brightness of reconstructed images.

1.2 OBJECTIVES

The general objective of this work is to propose and evaluate the performance of adaptive beamforming techniques with application in the reconstruction of Ultrasound-based medical images. In the evaluation of the performance of beamforming techniques the following methods are used: the Full Width at Half Maximum (FWHM), Contrast (CR), Contrast to Noise Ratio (CNR) and the speckle statistics.

To accomplish the main goal outlined above, the following specific objectives have been defined:

- Propose and implement the Bayesian-based post-filter beamformer with the Wiener post-filter based beamformer.
- Evaluate the performance of the proposed method by means of FWHM, CR,

CNR, and the speckle statistics. The evaluation is performed using simulation and experimental data collected on laboratory and simulation, experimental and human *in-vivo* data available in Plane Wave Challenge in Medical Ultrasound Imaging (PICMUS) platform and;

- Human *in-vivo* data available on PICMUS platform.

1.3 THESIS OUTLINES

The thesis is organized as follows:

Chapter 2 presents the basics of ultrasound, the background where the entire data acquiring and signal model is presented as well as the beamforming techniques, and the evaluation metrics of the proposed methods.

In this Chapter 2, different beamformers are presented and the MV beamformer is highlighted by representing the core of all adaptive processing. A description of the Bayesian-based beamformer for adaptive processing using an arbitrary array is presented.

In Chapter 3, the MV-BY beamformer is proposed to US imaging. Later, the MV-BY is combined with the WPF approach to form the MV-BY-WPF beamformer. Also, Chapter 3 presents the methods applied for quantitative evaluation of the performance of the proposed beamformers. Both, the data acquiring process for simulation and phantom data as well as the assessment of the simulation, phantom, and human *in-vivo* dataset available in the research Plane Wave Challenge in Medical Ultrasound (PICMUS) Imaging platform are described.

Particular to the simulation, data was acquired using Verasonics system (Verasonics Ltd, Kirkland-WA, USA) working on simulation mode while for the rest of simulation data were generated using Field II simulation program and was made available on the PICMUS platform. Additionally, the complementary phantom data was acquired using a Verasonics's system. The performance evaluation of the proposed techniques is performed using the spatial resolution with the Full Width at Half Maximum (FWHM), Contrast (CR) or Contrast-to-noise Ratio (CNR) and the speckle statistics in ultrasound imaging.

Chapter 4 presents the simulation, where phantom experimental and human *in-vivo* results are obtained, and quantitative and qualitative assessment of the

proposed beamformers are presented.

The Bayesian Minimum Variance (MV-BY) and the Bayesian Minimum Variance with the Wiener Post-filter (MV-BY-WPF) results are presented and also compared with different beamformers with spetial attention given to the DAS beamformer. Additionally, it is shown that MV-BY and the MV-BY-WPF outperform MV and MV-WPF, and, it is demonstrated that MV-BY-WPF achieves better contrast while retaining the imaging brightness without degrading the spatial resolution compared to the MV-WPF.

Chapter 5 presents a discussion of the most relevant results obtained from the evaluation of the proposed beamformers. Besides the spatial resolution, contrast, speckle statistics results, the computational complexity for different beamformers is also discussed.

Chapter 6 describes in summary the proposed methods, the results and closes the study.

2 THEORETICAL FRAMEWORK

This chapter presents a brief overview of medical Ultrasound (US) ultrasound imaging fundamentals. The acoustic wave propagation and wave-tissue interaction are described. The basic principles such as acoustic impedance, scattering, attenuation, and ultrasound transducer configuration are presented. The basis of conventional imaging in terms of scanning modes as well as the plane wave imaging are provided. Additionally, the basic steps of image formation and visualization are also included.

2.1 ULTRASOUND WAVE PROPAGATION

In accordance with Fig. 1, a longitudinal pressure wave is emitted into the tissue medium (i.e., region of interest) by a specific acoustic source. The wave propagates from source in a predefined direction. This propagation originates an oscillating motion of the medium particles which is parallel to the wave direction as presented in Fig. 1.

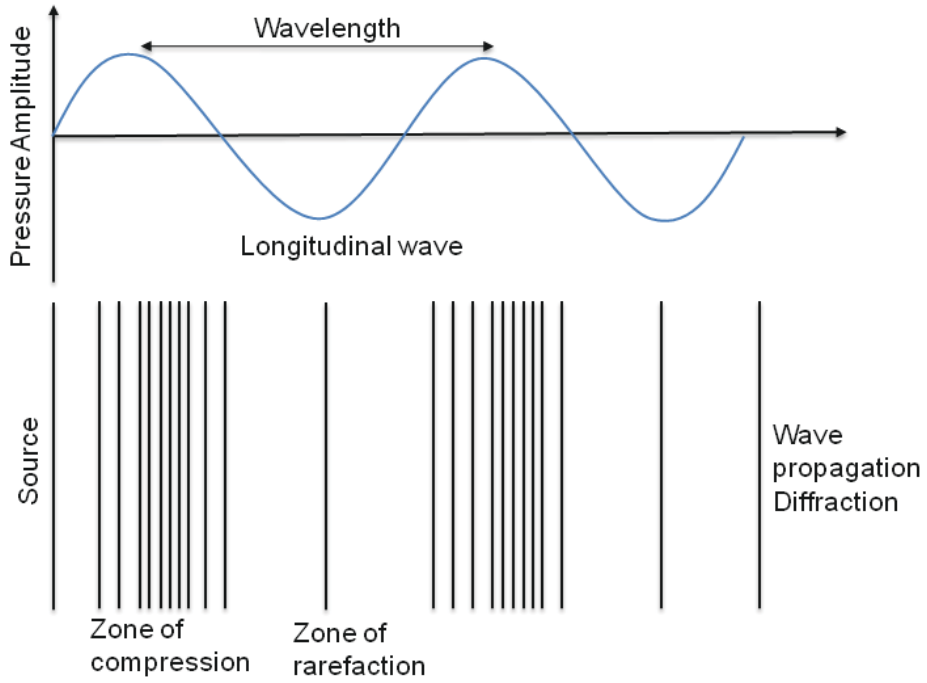

Figure 1: The representation of zones of compression and rarefaction created in a medium due to the propagation of a longitudinal acoustic waves. Adapted from (LØVSTAKKEN, 2007).

In practice, as the wave crosses the medium, zones of compression and rarefaction which are created corresponding to the peaks and troughs of the pressure wave. Such zones are separated by a wavelength.

Let the density of the medium be ρ and the compressibility of the medium k_c. The speed of acoustic propagation c of the longitudinal wave will be dependent on ρ and k_c as in Eq. (1) (SHUNG, 2006).

$$c = \sqrt{1/(\rho k_c)} \tag{1}$$

In Eq. (1) we see that less compressible mediums present higher propagation speeds. For example, the human tissue has an acoustic speed representing an adoption employed by different Ultrasound (US) devices, which is almost 1540 ms^{-1} as can be seen in Table 1 (SZABO, 2004b). Different values of the sound speed for different materials are presented in Table 1 (SZABO, 2004b).

Table 1: Speed of ultrasound c, acoustic impedance Z, and attenuation coefficients α for different materials (SZABO, 2004b).

Material	$c(m/s)$	$z(\frac{kg}{m^2 s^2})10^{-4}$	$\alpha = (dB/cm$ at 1 $MHz)$
Air	330	0.0004	12
Water	1480	1.48	0.0022
Fat	1450-1460	1.34-1.38	0.52
Brain	1560	1.55	0.85
Liver	1555-1570	1.65	0.96
Kidney	1560	1.62	1.0
Spleen	1570	1.64	1.0
Blood	1550-1560	1.61-1.65	0.17
Muscle	1550-1600	1.62-1.71	1.2
Lens of eye	1620	1.85	2.0
Skull bone	3360-4080	6.0-7.8	11.3

2.1.1 ACOUSTIC IMPEDANCE

The acoustic impedance represents the resistance of a material to the passage of an incident pressure wave, and it plays an important role in the ultrasound basis definition by determining the amount of energy involved in the imaging process.

The value of acostic impedance of the medium, z_m, is expressed by the product of the speed of acoustic propagation, c, and the density of the medium, ρ, given by Eq. (2) (SZABO, 2004a). Examples of acoustic impedance values for specific materials are presented in Table 1.

$$z_m = c\rho \tag{2}$$

The scattering at the interface between two objects of different acoustic impedance depends on the size of the scattering object when compared to the wavelength of the incident wave. Additionally, the scattering depends on the difference in acoustic impedance across the boundary (EVANS et al., 2000).

2.1.2 ULTRASOUND WAVE AND MEDIUM INTERACTION

Scattering encompasses a loss of energy from a specific wave and therefore describes the deviation of a wave from the original direction of transmission. Absorption represents the conversion of motion energy of the acoustic wave into thermal energy, mostly due to a relaxation process of tissue insonation (SHUNG, 2006).

In an ultrasound wave and medium interaction, the size of an object in the medium varies its behavior according to the incident wavelength. Depending on the context it may affect or influence the scattering which can be described in three major modes of tissue interaction: As depicted in Fig. 2 (a), Fig. 2 (b) and Fig. 2 (c), they are named, respectively, as *specular reflection*, *diffusive scattering* and *diffractive scattering*. Those tissue interaction types are discussed in the following manner: Specular reflections as shown in Fig. 2 (a) are supposed to occur when the US wavelength is smaller than the dimensions of the object in the medium. The specular reflection as shown in Fig.2 (b) results in part of the incident beam being reflected and another part being refracted at a boundary of differing acoustic impedance.

Eq. (3) and Eq. (4) present the reflection (R_c) and the transmission (T_c) coefficients (EVANS et al., 2000).

$$R_c = \frac{Z_t cos\theta_i - Z_i cos\theta_t}{Z_t cos\theta_i + Z_i cos\theta_t} \tag{3}$$

$$T_c = \frac{2Z_t cos\theta_i}{Z_t cos\theta_i + Z_i cos\theta_t} \tag{4}$$

where, Z_i and Z_t represent the impedance measures of the tissue medium before (incident) and after (refracted) the tissue boundary, θ_i represents the angle at which the incident wave approaches the tissue boundary, and θ_t and θ_r represent the angles at which the refracted and reflected waves departs from the boundary, respectively.

Additionally, the refracted energy portion of the beam deviates as it crosses the boundary (SHUNG, 2006).

However, diffusive scattering results of emitting US wavelengths longer than the dimensions of the inhomogeneity in the tissue. In such a context, the reflection spreads out in all different directions as shown in Fig. 2 (b), for which a part of the signal returns to the transducer (EVANS et al., 2000).

The diffractive scattering depicted in Fig. 2 (c) originates from the scattering object of a size roughly equal to the wavelength. This results in the continuation of the US propagating in a continuous direction (SHUNG, 2006). These fundamentals are directly involved in ultrasound data acquiring.

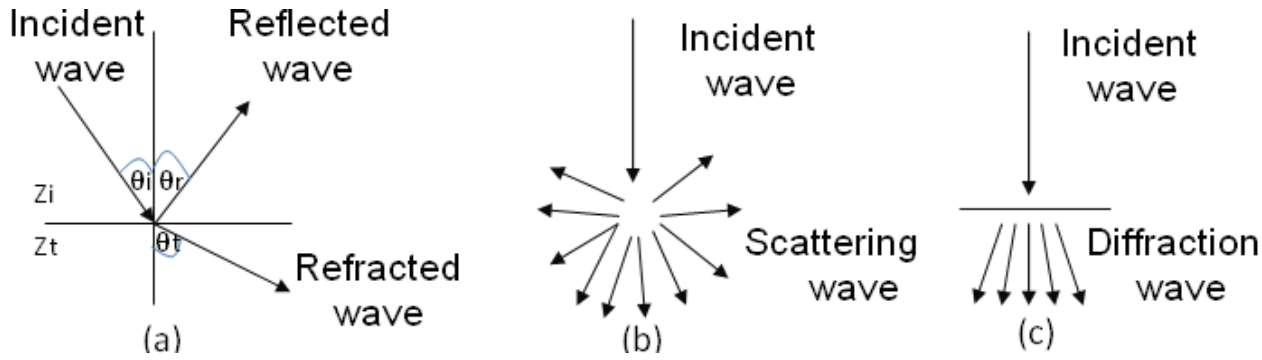

Figure 2: Representation of the three major modes of scattering in tissue: (a) for specular reflection and, (b) for diffusive scattering and, (c) for diffractive scattering. Adapted from (RITENOUR, 1990; JENSEN, 1996a)

2.1.3 ATTENUATION

The energy loss is involved in acoustic wave propagation through a heterogeneous medium. Among other factors, the scattering and absorptions are two major determinants for attenuation (SHUNG, 2006).

In practice, the acoustic energy loss in the received signal is revealed through attenuation and can be expressed as a function of distance traveled or depth in the medium as of the emitted central frequency as in Eq. (5).

$$I(z, f_0) = I_0 e^{-\alpha f_0 z} \tag{5}$$

The Eq. (5) describes the characteristics of the attenuation in tissue, where *I* represents the amplitude of intensity of the propagating wave, z is the depth and f_0 is the emitted frequency, respectively.

The amplitude of initial intensity of the propagating wave I_0 is the initial intensity of the wave at emission and α represents the attenuation coefficient. Notably, there is an exponential decrease in the initial signal amplitude as a wave propagates further into the tissue (SHUNG, 2006).

Typically, data acquisitions of deep anatomy structures use central frequencies ranging from 1 to 3 MHz and data acquiring involving more superficial structures is performed with central frequencies ranging from 5 to 10 MHz, which allows enough signal reception even with the frequency dependent effects of attenuation in such situations (RITENOUR, 1990).

2.2 BASICS OF ULTRASOUND IMAGE ACQUISITION

In US data acquisitions, a transducer emits a pressure wave into a target which can either be a mimicking phantom or tissue medium using a pulse-echo technique.

In this context, the characteristics of the transducer, the transducer structure and, the beam it creates have an effect on the resulting images mainly on visualization of the anatomical structures. These characteristics can be described with reference to their effect on image quality.

2.2.1 ULTRASOUND TRANSDUCER

In a US imaging system, the purpose of a US transducer is to emit and receive waves. Among different components, one of the main transducer components is the piezo-electric (PZT) elements which are contained within the transducer housing. This material has the ability to act as a bridge between electrical and mechanical energy by imposing a source of vibration on a PZT material. This results in the production of an electrical signal from US waves received in the transducer.

The reverse process, based on the same effect, is achieved by applying a

transient electrical signal to originate a vibration in the form of a source of ultrasonic pressure wave employed during transmission (SHUNG, 2006).

Among different transducer abilities, the element may emit a signal at a particular central frequency in the range of transmitted frequencies, termed as transducer bandwidth (BUSHBERG; BOONE, 2011). The transducer bandwidth is an important characteristic and has important implications for imaging as it determines the imaging resolution. For example, the improved image resolution can be achieved by transmitting shorter pulses, which imply on a larger pulse bandwidth, constrained by the limits of the bandwidth of the transducer (BUSHBERG; BOONE, 2011).

The transducer array is composed of multiple sensor elements. Fig. 3 presents the configuration of these elements. Each PZT element is separated from each other by a distance referred to as the **kerf** and the distance between element centers is referred to as **pitch**. These dimensions are of capital importance in this work since they provide all the lateral distances used to appropriately calculate the delays required for beamforming (SHUNG, 2006).

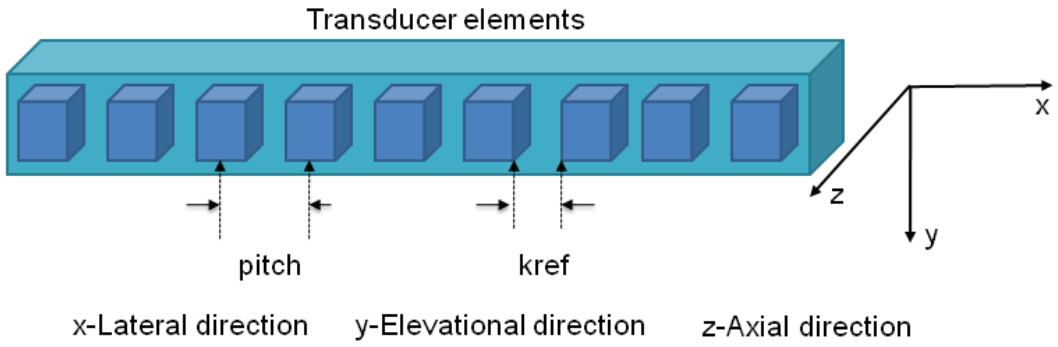

Figure 3: The configuration and orientation with all the basic elements of a transducer array. Adapted from (SWILLENS, 2010).

In order to define the orientation of the two-dimensional (2D) plane of an image with respect to the transducer, the terms axial direction z[mm] and lateral direction x[mm] are used. While the former is in-line with the beam direction and orthogonal to the surface of the transducer, the later runs along the length of the probe over all sensor elements, perpendicular to the beam direction. The elevation direction represents the width of the probe and is orthogonal to the image plane (SHUNG, 2006). Among different types of multi-element transducer arrays, the two most popular types of probes are the linear array and phased array transducers.

These types of transducers can excite the medium with multiple focused beams

corresponding to scan-lines of echo data or with oriented plane wavefronts. The main difference between the two transducer types is the active region excited to produce each beam Shung (2006), shown in Fig. 4.

The conventional scanning modes of two common transducer formats: Fig. 4 (a) is the phased array transducer and Fig. 4 (b) is the linear array transducer. The horizontally dashed arrows in both panels show the course of the scan along the lateral direction. The vertical dashed lines indicate the plane wave transmission orientation while the horizontal indicates the plane wavefronts for both cases: Fig. 4 (c) for the phased array transducer and, Fig. 4 (d) for the linear array transducer.

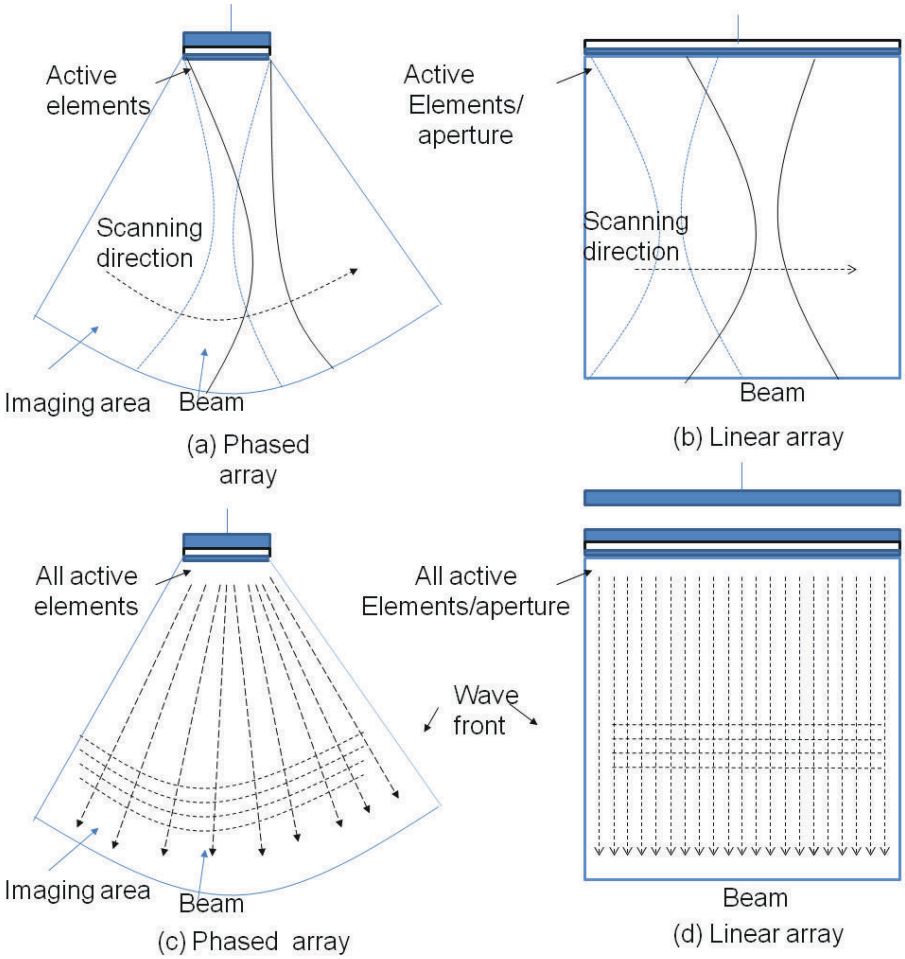

Figure 4: The conventional scanning modes of two common transducer formats: (a) is the phased array transducer and (b) is the linear array transducer. The dashed arrows in both panels show the course of the scan. The vertical dashed lines indicate the plane wave transmission orientation while the horizontal indicates the plane wavefronts for both cases: (c) for the phased array transducer and, (d) for the linear array transducer. Adapted from (DORT et al., 2012; SZASZ, 2016)

In US image formation with a phased array, all elements are activated for each

beam. Subsequently, a sequence of beams is emitted using a specific steering in order to cover the region of interest which forms a scan sector while emitting a set of waves in line-by-line scanning mode.

The linear array transducer elements are stimulated in groups called *aperture* where subsequent beams are formed by moving the aperture across the transducer (DORT et al., 2012). Only the linear array transducer operating in plane wave transmission has been applied in this work.

2.2.2 THE BEAM ORIENTATION

In acoustic wave emission, the US beam orientation is related to the transducer geometry and the system wavelength. For an unfocused or plane-wave multi-element beam which is the case of this work, the occurrence of the interaction and interference patterns among the diffracted waves of each transducer element is observed, and the wave field can be found by collectively combining the diffracted wave pattern of each of the elements (BUSHBERG; BOONE, 2011).

In practice, for focused beamforming as illustrated in Fig. 5, the acoustic field shows two regions separated by a zone for which the beam has a minimum cross-section due to inherent convergence referred to as *diffractive focusing*. The diffractive focal zone devides the imaging area in two regions which are termed as the *near field* (or Fresnel zone) and the *far field* (or Fraunhofer zone) as shown in Fig. 5 (BUSHBERG; BOONE, 2011).

In this context, an important parameter can be defined, the F_n *F-number*. The *F-number* is directly related to the image quality by means of spatial (lateral) resolution. The *F-number* represents the ratio of focal ditance to aperture length as in Eq. (6). Given a certain *F-number*, the beam width, D_b, can be obtained as in Eq. (7).

$$F_n = D_f / D_{ap} \tag{6}$$

$$D_b = \lambda F_n \tag{7}$$

where D_b and D_f represent the focal beam and focal distance. Additionally, the λ , is the wavelength.

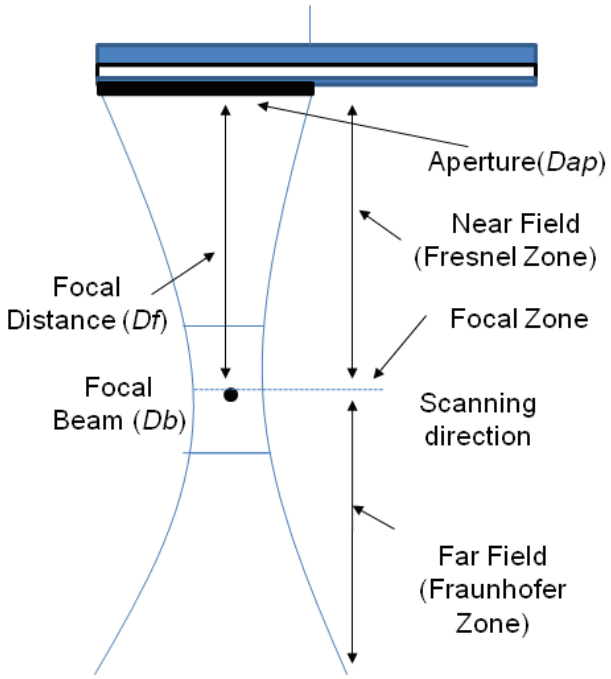

Figure 5: Profile of focused ultrasound beam exhibiting a focal zone. Adapted from (DORT et al., 2012)

In spite of diffractive focusing which in general occurs beyond the desired depth for medical imaging, electronic delays can be applied to each element which in turn act in order to focus a beam. In standard imaging systems, it involves the application of electronic delays prescribed to each element, which act to focus the beam more sharply at the desired direction or at a specific depth from the transducer. The curved apertures or lenses are also used. The concept of electronic delay focusing is depicted in Fig. 6.

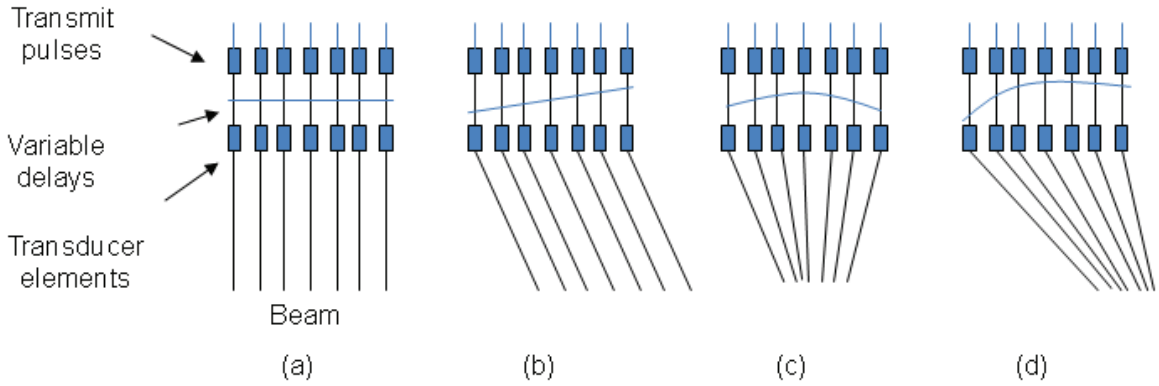

Figure 6: The beamforming applying electronic delays to produce (a) for a flat planar-wave and, (b) for an oriented planar-wave and, (c) for a focused beam, and (d) for an oriented focused beam. Adapted from (LØVSTAKKEN, 2007)

Electronic delays consist of transmitting pulses at variable time delays where each element will emit a pulse at different time (or instant) (BUSHBERG; BOONE, 2011). This concept is essential for plane wave compounding imaging by allowing transmit plane wave sequences with different steering angles.

2.2.3 PLANE-WAVE ULTRASOUND EMISSION

The Plane-wave US imaging has interested the research community mainly due to its ability to provide elevated frame-rates which exceed those of other high frame-rate techniques. It belongs to a set of the parallel beamforming scheme in which all elements are kept active and therefore can transmit pulses simultaneously. Such ability to transmit and receive waves simultaneously has a great potential for very high frame rate imaging.

In the sequel, due to technological advances, ultrasound systems have been equipped with plane-wave capabilities, as well as the processing and manipulation of large datasets which can be done more efficiently at high frame rate (DORT et al., 2012).

The ability to excite all of the transducer elements at the same time with an identically shaped pulse produces a planar wave-front which is shown in Fig. 7 (a). Applying the electronic delays principle, the transducer elements may be stimulated with a linear delay in accordance with the transducer array geometry to tilt the planar wavefront, which allows for an angled acquisition, as depicted in Fig. 7 (b) (SZASZ, 2016).

program Jensen (1996b). All the theoretical principles presented in this work are involved in this process.

The image data acquisition starts with the excitation of the transducer, through the interaction between the acoustic waves with the particles in the medium. The procedure is then followed by the raw channel data formation.

The scanning process includes an important step, which consists of determining the imaging regions either for phantom experimental data acquisition or the *in-vivo* data, after the reception of the raw channel data.

Thus, different uniformly weighted Delay-and Sum (DAS) beamforming approaches or adaptive beamformers can be applied to raw channel data to form the beamformed data.

While the former set of methods provides the best trade-off between side-lobe level and the width of the main lobe (e.g., Fig. 8), the latter combines both abilities providing improved performance in terms of spatial resolution and contrast.

Moreover, adaptive beamforming is the core of this work. The next Section

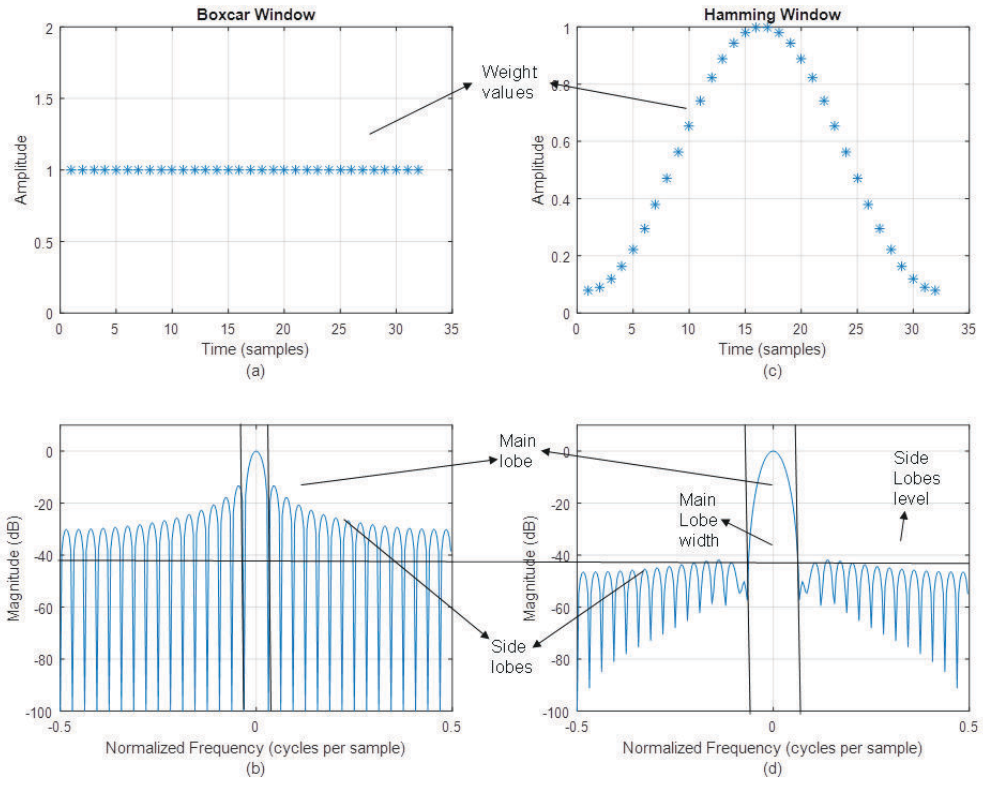

Figure 8: Radiation the pattern for fixed weighting windows: (a) apply boxcar apodization and (c) the normalized Magnitude in (dB) as well as the normalized Frequency for each sample. Similarly, (b)-(d) apply Hamming apodization.

presents different categories of adaptive beamformers.

In order to finalize the image formation process, the beamformed images are then converted into B (brightness) mode images, using conventional post-processing techniques such as envelope detection, logarithmic compression, and scan conversion (SZASZ, 2016).

Generally, B Mode images are commonly displayed in Dynamic Range (DR) of 60 dB.

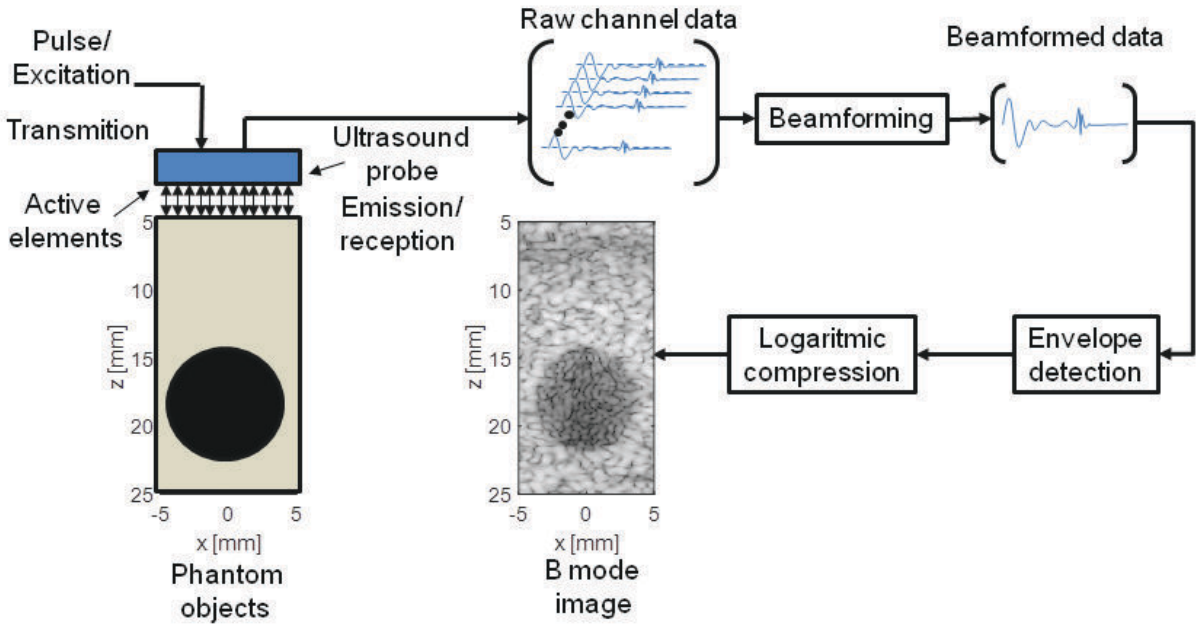

Figure 9: The basic and general US image scanning process and image visualization. The B mode image in the diagram was generated using Field II program (JENSEN, 1996b).

2.3 BEAMFORMING THEORETICAL BACKGROUND

2.3.1 COHERENT PLANE WAVE COMPOUNDING

In order to implement Coherent Plane Wave Compounding (CPWC), a single plane wave can be used to represent a typical configuration of plane wave ultrasound imaging systems.

Typically, a linear array made of 128 transducers is put directly or closely in contact with the medium of interest and the corresponding lateral direction of the imaging region (i.e., rectangular) is parallel to the array while the axial direction is perpendicular the array surface.

Since the ultrafast imaging aims to obtain an image frame simultaneously from a single transmitted acoustic pulse with parallel processing, it illuminates the medium by transmitting a large beam of a single pulsed plane wave (MONTALDO et al., 2009).

In plane wave imaging we do not have any focusing for the transmitted beam, only parallel processing during the reception contributes for image resolution (MONTALDO et al., 2009).

To overcome the effect of poor resolution, the above-mentioned transmission is performed using steering angles, shown in Fig. 10 for each transmitting event in order to cover a specific region of interest (DORT et al., 2012).

Hence, the coherent summation in the spatial compounding process of images obtained from plane wave transmissions must take into account the steered angles applied in transmission (MONTALDO et al., 2009).

By performing spatial compounding the image quality gets significantly improved. This achievement is accomplished by adding coherently the sequenced echoes coming from the same scatter. By doing so, a set of low-resolution images are combined to form a high quality synthesized image (ZHAO et al., 2015).

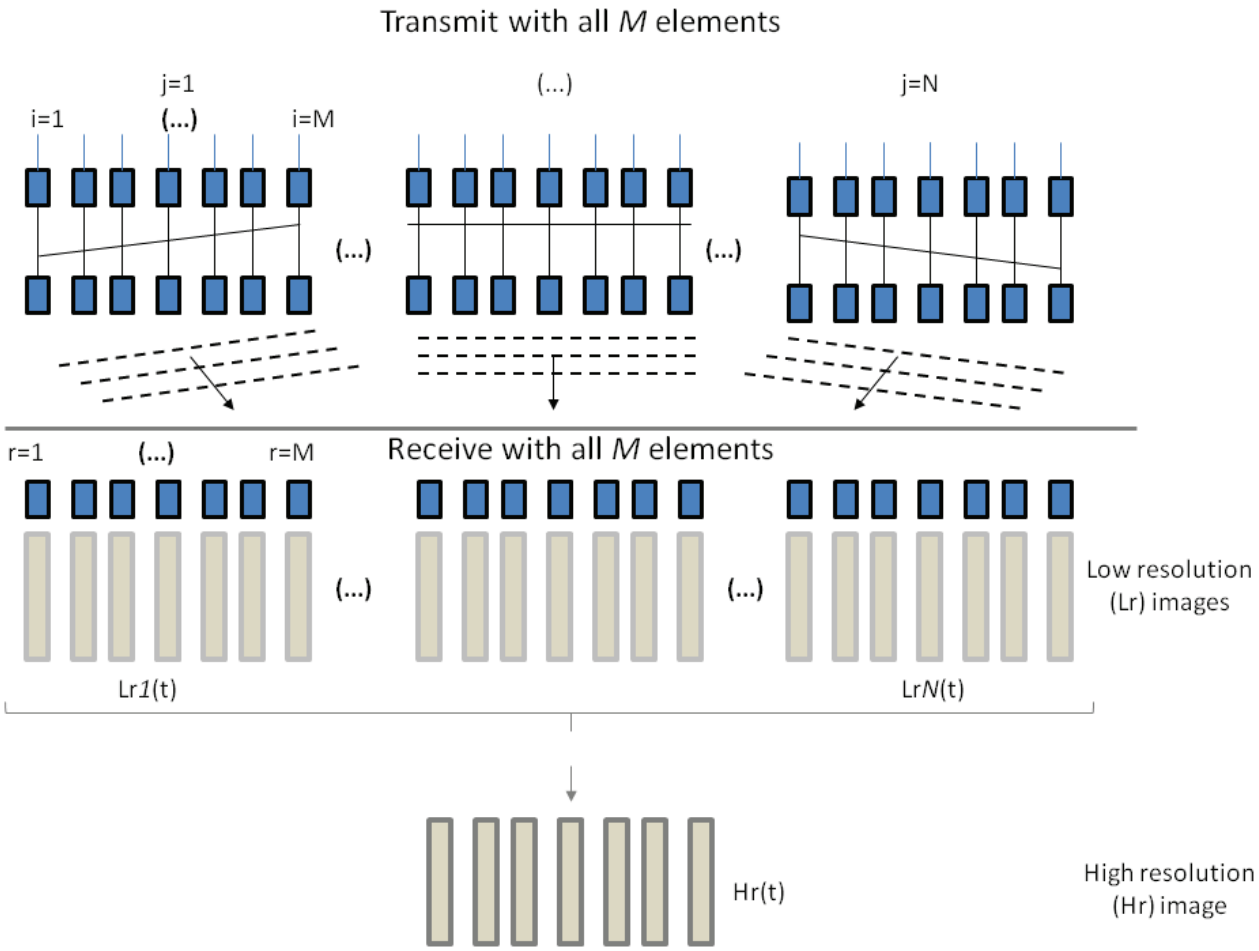

Figure 10: High-resolution Image (HRI) formation from a set of low-resolution images (LRI) in CPWC. It represents the imaging principle in parallel processing mode for emission of plane waves. For individual emission using all transducer elements, all transducer elements receive signals to yield LRIs. The LRIs are therefore combined to compound a HRI. Modified from (SZABO, 2004a, 2004b).

In CPWC, the aim is obtaining the High-resolution Image (HRI) from a set of Low-resolution Images (LRI) obtained from a set of steered plane waves. The final image is obtained by summing accordingly a set of successive frames as depicted in Fig. 10.

In Montaldo et al. (2009), an important comparison was derived between the plane-wave compounding approach and a traditional multi-focus imaging. In such comparison it was demonstrated that the plane-wave compounding approach can reach the traditional multi-focus image quality using a small number of plane wave transmissions while preserving high frame rates.

In CPWC, the signal in (x,z) is a linear combination of impulse response between the plane waves and the receiving elements. In Eq. (8), h_{jr} is the signal

received by element r when plane wave j is emitted. From Fig. 11, the signal (x,z) is obtained as in Eq. (8) (RODRIGUEZ-MOLARES et al., 2015),

$$x_{CPWC}(x,z) = \sum_{r=1}^{\mathrm{M}} u(\mathrm{x}_r) \sum_{j=1}^{\mathrm{N}} w(\alpha_j) h_{jr}\left(\frac{D_j + D_r}{c}\right) \tag{8}$$

where r is the receiving element, c the speed of sound in the medium, M the number of elements in the transducer, N is the number of Plane Wave Emissions (PWE), $\vec{u}$ a vector representing the receive apodization window and, $\vec{w}$ is a vector angular apodization. Let λ be the wavelength of the imaging system and A the probe aperture, the distances D_j in Eq. (9), D_r in Eq. (10) and the angle sequence α_j in Eq. (11), are formulated as follows (RODRIGUEZ-MOLARES et al., 2015):

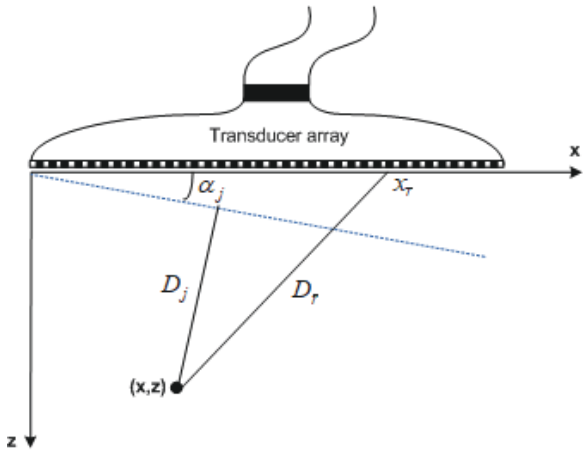

Figure 11: Geometric representation of plane wave emission and signal reception in coherent plane wave compounding.

$$D_j = z\cos\alpha_j - x\sin\alpha_j, \quad j = 1,\cdots,N \tag{9}$$

$$D_r = \sqrt{z^2 + (x - x_r)^2} \tag{10}$$

$$\alpha_j = \left(1 - \frac{N+1}{2}\right)\frac{\lambda}{A} \tag{11}$$

Signals in Eq. (8) provide a bidimentional (2D) echo data matrix representation as in Eq. (12) at time step k.

$$X(k) = \begin{bmatrix} (x_r^1(k))^T \\ (x_r^2(k))^T \\ \cdots \\ (x_r^N(k))^T \end{bmatrix} = \begin{bmatrix} x_1^1(k) & x_2^1(k) & \cdots & x_M^1(k) \\ x_1^2(k) & x_2^2(k) & \cdots & x_M^2(k) \\ \cdots & \cdots & \cdots & \cdots \\ x_1^N(k) & x_2^N(k) & \cdots & x_M^N(k) \end{bmatrix} \tag{12}$$

where $(\bullet)^T$ is the transpose and $x_r^j(k) = [x_1^j(k), x_2^j(k), \cdots, x_M^j(k)]^T$, represents the array echo data after time delay calculation of the jth wave emission.

The coherent compounding method averages the echoes to get the signal output as in Eq. (13).

$$z(k) = \frac{1}{MN} \sum_i^M \sum_j^N x_i^j(k) \tag{13}$$

2.3.2 MINIMUM VARIANCE BEAMFORMER

In Minimum variance (MV), the output of a beamformer is a combination between a set of adaptive weights and the input data as in Eq. (14),

$$z(k) = \vec{w}^H \vec{x}(k), \tag{14}$$

where k is the time index, $\vec{x}(k)$ is the input data, $\vec{x}(k) = [x_1(k), x_2(k), \cdots, x_M(k)]^T$, $w(k)$ is a vector of beamforming weights, $\vec{w} = [w_1, w_2, \cdots, w_M]^T$, $(\bullet)^T$ denotes the transpose and $(\bullet)^H$ the Hermitian, respectively. Each collum of the array of data samples in Eq. (12) can be expressed in terms of Desired Signal (DS) samples and noise components of zero mean and, Gaussian random process as in Eq. (15):

$$\vec{x}(k) = s_d \vec{a}(k) + \vec{n}(k) \tag{15}$$

where s_d is the source signal, $\vec{n}(k)$ is a vector of additive noise samples.

The weight of the MV beamformer is found by minimizing the power of the output $\left\{P = E\left\{|z(k)|^2\right\} = \vec{w}^H E\left\{x(k)x(k)^H\right\}\vec{w} = \vec{w}^H R \vec{w}\right\}$ subject to the the constraints as in Eq. (16):

$$\vec{w}_0 = \arg\min_{\vec{w}} \left\{\vec{w}^H R \vec{w}\right\} \text{ subject to } \quad \vec{w}^H \vec{a} = 1 \tag{16}$$

where E is the expectation operator, $\vec{a} = 1_{Mx1}$, $\vec{a}$ is the array steering vector, $\vec{w}_{1xM}$, $\vec{w}$ is the weight vector and, $R = E\left\{x(k)x(k)^H\right\} = |s_d|^2 \vec{a}\vec{a}^H + E\left\{n(k)n(k)^H\right\}$. R represents the Covariance Matrix (CM). The solution of the minimization problem using the Lagrangian multipliers as presented in Appendix A is given by Eq. (17):

$$\vec{w} = \frac{R_{MxM}^{-1}\vec{a}_{Mx1}}{\vec{a}_{Mx1}^{H}R_{MxM}^{-1}\vec{a}_{Mx1}} \tag{17}$$

where $\vec{w}$ is the weight vector, $(\bullet)^{-1}$ stands for inverse operation, R is the data CM. As presented in Eq. (16) the aim of MV beamformer is to minimize the output power of the estimated signal while keeping it undistorted. For such purpose, the directional constraints are set to be unitary in order to guarantee that the signals arriving in the array sensors are coming from broadside.

For full adaptive array processing (i.e., if subarray averaging is not applied), the beamformer output can be formulated as in Eq. (18).

$$z_{MV}(k) = \vec{w}^{H}\vec{x}(k), \tag{18}$$

When the CM in Eq. (17) is replaced with an identity matrix corresponding to the CM for spatially white noise, it becomes a uniformly weighted DAS beamformer which averages over M array elements as in Eq. (19).

$$\vec{w}_{DAS} = \frac{I_{MxM}^{-1}\vec{1}_{1xM}}{\vec{1}_{1xM}^{H}I_{MxM}^{-1}\vec{1}_{1xM}} = \frac{1}{M}\vec{1}_{1xM} \tag{19}$$

However, for adaptive processing, the data CM R is obtained from the data. In order to decorrelate the coherence between input echo signals and provide data CM stability, the subarray averaging and diagonal loading (DL) techniques are applied as in Eq. (20) (LI et al., 2016). While the former consists of dividing the dataset in overlapped vectors X_l whose length is limited to ($L \leq M/2$), the latter represents an addition of controlled white noise to data CM.

$$R = \frac{1}{D}\frac{1}{S}\sum_{k=-T}^{D}\sum_{l=1}^{S}X_l(k)X_l(k)^{H} + \mu_{DL} \tag{20}$$

where $D = 2K+1$ and $S = M-L+1$. D denotes the number of temporal samples and S the number of subarrays used in CM estimation, $\mu_{DL} = \frac{1}{\Delta * L}tr\{R\}I$, $\vec{X}_l = [x_l(k), x_{l+1}(k), \cdots, x_{l+L-1}(k)]^T$ and Δ, L are respectively the DL factor and subarray length, while tr stands for trace. X_l represents the data submatrices used in data subarray averaging (LI et al., 2016). In the other words, the term μ_{DL} can be considered as the regularization term of the data CM.

Taking into account the effects of subarray averaging, the length of the estimated weight vector and the length of input data have their dimension in

accordance with the subarray length. The beamformer output can be formulated as in Eq. (21).

$$z_{MV}(k) = \frac{1}{S}\sum_{l=1}^{S} \vec{w}(k)^H \vec{X}_l(k) \tag{21}$$

Figure 12 depicts a subarray structure. In Fig. 12 the subarray averaging (i.e., spatial smoothing) process is represented. The subarray averaging is performed in order to decorrelate the DS with interference and noise. The example shows an array consisting of 8 sensors (i.e., array elements) which form a total of S=5 subarrays of L=4 sensors using formula $S = M - L + 1$. Right-most, a set of highlighted blocks of the data covariance matrix corresponding to each subarray (on the right) is presented. There are 5 covariance matrices corresponding to 5 subarrays.

However, this is just an example because in practice we have M=128 sensor elements and the adaptive processing is done taking into account a subarray of L=38 sensor elements as will be presented in Section 3.2.

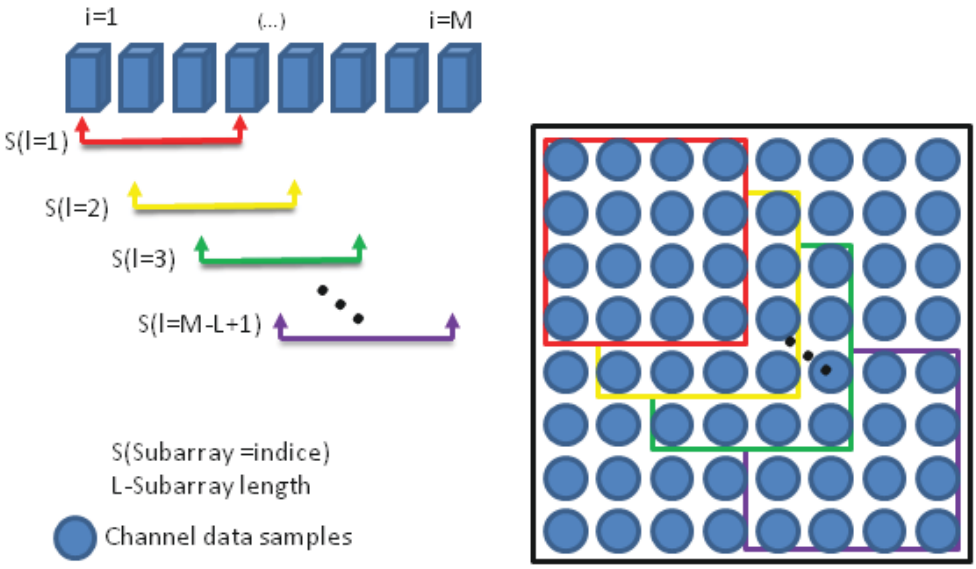

Figure 12: A relatively larger array is divided into (overlapping) subarrays of length L so that the spatial covariance matrices of the subarrays are averaged in order to decorrelate the array signals. The example shows an array consisting of 8 sensors which form a total of 5 subarrays of 4 sensors using formula $S = M - L + 1$. Right-most, a set of highlighted blocks of the data covariance matrix corresponding to each subarray (on the right) is presented. There are 5 covariance matrices corresponding to 5 subarrays. Adapted from (SZASZ, 2016; VOROBYOV, 2014).

The MV beamformer diagram in Fig. 13 can well be represented based on

space data dimensionality reduced used to represent the spatial smoothing process in Fig. 12. In Fig. 13 the array data summation procedure using the MV beamformer to US imaging is represented.

At one hand, from Fig. 13 the array data $X(k)$ consisting of k samples of N emissions of M array sensors as presented in Eq. (12) are labeled as (1) and, serve as input data to the MV estimator (2) which generates a set of adaptive weight vectors w_{MV} for each emission as in label (3). On the other hand, the array data in label (1) is divided into subarrays consisting of a set overlapped vectors $X_l(k)$ which are then averaged in label (4) so that a set of adaptively calculated weight vectors are combined with the subarray averaged data producing the desired signal $z_{MV}(k)$ for each emission as presented in label (5).

From Fig. 13, the weight vectors in the label (3) and the corresponding subarray averaged data in the label (4) are combined to form a beamformer output as in label (5) for each imaging point as presented in Eq. (21). This procedure is repeated for each emission and, in order to form the imaging point, the beamformed data for each emission are synthesized in accordance with the CPWC principle.

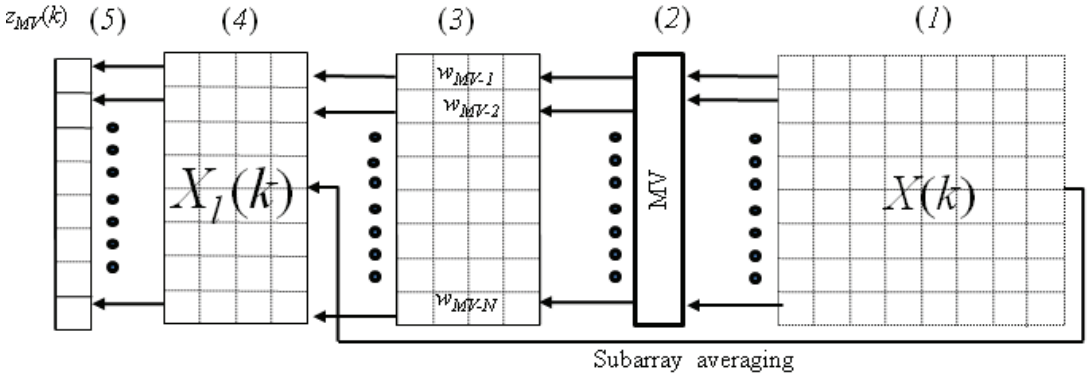

Figure 13: The MV beamformer diagram to medical US imaging. The array data summation procedure using the MV beamformer to US imaging.

2.3.3 THE COHERENCE FACTOR BEAMFORMING

The Coherence Factor (CF) is defined as the ratio between the coherent and incoherent sums across the array.

The CF has improved the spatial resolution and contrast at the cost of suppressing image details which originates imaging artifacts when SNR is low.

In accordance with Eq.(22), the $CF \in [0,1]$ is obtained taking into account the Coherent Sum (CS) and Incoherent Sum (IS) signal energy. The CF is used as a metric of focusing quality (HOLLMAN et al., 1999; MALLART; FINK, 1994; LI; LI, 2003).

$$CF = \frac{CS}{IS} = \frac{|\sum_{m=0}^{M-1} x_m(k)|^2}{M\sum_{m=0}^{M-1} |x_m(k)|^2} \tag{22}$$

The beamformer output which can be either DAS beamformer or the MV beamformer can be formulated as in Eq. (23):

$$z_{CF}(k) = CF\, z(k) = CF\, \vec{w}^{\mathsf{H}} \vec{x}(k) \tag{23}$$

2.3.4 THE WIENER POST-FILTER BEAMFORMING

The Wienner post-filter (WPF) has been introduced in order to improve the image quality. The WPF has improved the shortcomings of traditional CF based method (NILSEN; HOLM, 2010). The WPF produces an output signal which is the Minimum Mean Squared Error (MMSE) estimate of the signal of interest (for the adaptive or nonadaptive beamformer output).

In this context we believe that it could provide an image of improved quality under different SNR scenarios but it works based on estimation of DS power or the noise signal power which are hard to estimate (NILSEN; HOLM, 2010).

In order to obtain the WPF solution, the following optimization problem Eq. (24) needs to be solved in order to obtain the beamformer weights (NILSEN; HOLM, 2010).

$$\vec{w}_{Wiener} = \arg\min_w E\left\{ |s_d - \vec{w}^H \vec{x}|^2 \right\} \tag{24}$$

The solution to the optimization problem which is presented as in Eq. (25) can be found in Appendix B.

$$\vec{w}_{Wiener} = |s_d|^2 R^{-1} \vec{a} \tag{25}$$

where $\vec{w}_{Wiener}$ is avector containing the Wiener beamformer and $\vec{a} = \vec{1}$.

The data covariance matrix components can be expressed as in Eq. (26) (NILSEN; HOLM, 2010).

$$R = |s_d|^2 \vec{a}\vec{a}^H + E\left\{ nn^H \right\} = |\mathrm{s}_d|^2 \vec{a}\vec{a}^H + R_n \tag{26}$$

In order to accurately invert the CM in Eq. (26), the matrix inversion Lemma (i.e., the Woodbury matrix identity) is applied. Based on Eq. (25) which is shown in Appendix C, the solution of Eq. (27) is obtained,

$$\vec{w}_{Wiener} = \frac{|s_d|^2}{|s_d|^2 + \vec{w}^H R_n \vec{w}} \vec{w} = \frac{\sigma_s^2}{\sigma_s^2 + \sigma_n^2} \vec{w} \tag{27}$$

where $\vec{w}_{Wiener}$ (i.e., $\vec{w}_{Wiener} = H_{Wiener}\vec{w}$) is the Wiener beamformer and H_{Wiener} represents the Wiener post-filter (i.e., $H_{Wiener} \in [0,1]$). σ_s^2 and σ_n^2 are respectively the DS and noise plus interference Power components.

The WPF beamformer output can be obtained as in Eq. (28)

$$z_{Wiener}(k) = \vec{w}_{Wiener}^H \vec{x}(k) = H_{Wiener} \vec{w}^H \vec{x}(k) \tag{28}$$

In the WPF beamformer formulation, the DS, s_d represents a beamformer output which can either be adaptive or nonadaptive. In this work, we apply the WPF whose DS is obtained by the MV principle as in Eq. (27).

From Eq. (15) we can see that the Noise Plus Interference Covariance Matrix (NPICM) could be found from subtracting the DS of interest (DSI) from the collected data, however, in practical situations the DS of interest is unknown and, the best alternative for the present study should be the MV beamformer.

In accordance with Eq. (26), we can represent the data CM as $R = |s_d|^2 \vec{a}\vec{a}^H + R_n$. It means that $R_n = R - |s_d|^2 \vec{a}\vec{a}^H$ which could be inserted in standard data CM estimator used in MV beamformer (NILSEN; HOLM, 2010).

For such purpose, an estimate of the NPICM component R_n can then be obtained based on inserting the MV beamformer output z_{MV} on Eq. (29) to the common covariance matrix R estimator, given by Eq. (20) in order to obtain the estimator R_n as presented in Eq. (29).

$$R_n = \frac{1}{D}\frac{1}{S} \sum_{k=-T}^{D} \sum_{l=1}^{S} \left(\vec{X}_l(k) - z_{MV}(k)\right)\left(\vec{X}_l(k) - z_{MV}(k)\right)^H. \tag{29}$$

In accordance with Eq. (27), for MV beamformer, the WPF can be formulated as in Eq. (30).

$$H_{MV\text{-}WPF} = \frac{\vec{w}_{MV}^H R \vec{w}_{MV}}{\vec{w}_{MV}^H R \vec{w}_{MV} + \vec{w}_{MV}^H R_n \vec{w}_{MV}} \tag{30}$$

where $H_{MV\text{-}WPF}$ is the WPF applied to MV beamformer.

The weight vector and the beamformer can be formulated as in Eq. (31) and Eq. (32), respectively.

$$\vec{w}_{MV\text{-}WPF} = H_{MV\text{-}WPF}\vec{w}_{MV} \tag{31}$$

where $\vec{w}_{MV\text{-}WPF}$ is the MV-WPF weight vector.

$$z_{MV\text{-}WPF}(k) = \vec{w}^{H}_{MV\text{-}WPF}\vec{x}(k) \tag{32}$$

where $z_{MV\text{-}WPF}$ is the MV-WPF beamformer output.

2.4 THE BAYESIAN-BASED BEAMFORMER FOR ARBITRARY ARRAY ADAPTIVE SIGNAL PROCESSING

The Bayesian based beamformer formulation takes into consideration that the presented general signal model in Eq. (15) is assumed to be composed of source (i.e., the desired signal) and noise (i.e., we refer to as the noise plus interference and other incoherent noise sources) waveforms samples as functions of zero-mean Gaussian random process (BELL et al., 1997b, 2000; LAM; SINGER, 2006).

$$z_{MV\text{-}BY}(k) = \sum_{i=1}^{L_k} p(\theta_i|x)s(k) = \sum_{i=1}^{L_k} p(\theta_i|x)\vec{w}^{H}_{MV}\vec{x}(k)$$

$$i = 1, \cdots, L_k \tag{33}$$

where L_k is a set of points corresponding to the measurement grid in the imaging region in axial direction, s is the desired signal which in Eq. (33) is assumed to be the MV beamformer output.

The θ_i represents the source direction in degrees for the array steering vector which traditionally is set to be a vector of ones, (i.e., $\vec{a}(\theta_i) = \vec{a}(\theta_0) = \vec{a}_{1xM}$) (SYNNEVAG et al., 2007, 2009).

In the formulation of Bayesian-based method, the MV output is combined with the *a posteriori* Probability density function, pdf to form the z_{MV-BY}.

The beamforming output which is presented by Eq. (33) is formed by weighting the approximate *a posteriori* pdf, $p(\theta_i|x)$ with the desired signal s (BELL et al., 1997a, 2000; LAM; SINGER, 2006). The *a posteriori* pdf estimate is formulated using the

Bayes rule as in Eq. (34) (BELL et al., 2000).

$$p(\theta_i|x) = \frac{p(\theta_i)p(x|\theta_i)}{\sum_{j=1}^{L_k} p(\theta_j)p(x|\theta_j)} \tag{34}$$

where $p(\theta_i)$ is *a priori* pdf which provides the parameter statistical description and $p(x|\theta_j)$ is a likelihood function of the parameter given data (BELL et al., 2000; LAM; SINGER, 2006).

The observed data samples are supposed to be independent and identically distributed with *a priori* uniform distribution of $p(\theta_i) = 1/L_k$ (BELL et al., 2000). The *a posteriori* pdf estimate is formulated as in (BELL et al., 2000). In Eq. (35), the θ_i is the source direction in degrees for the array steering vector which traditionally is set to be a vector of ones, (i.e., $\vec{a}(\theta_i) = \vec{a}(\theta_0) = \vec{a}_{Mx1}$) (SYNNEVAG et al., 2007, 2009).

$$p(\theta_i|x) = cp(\theta_i)\mathbf{exp}\left\{\gamma K(\vec{a}(\theta_i)^H R^{-1}\vec{a}(\theta_i))^{-1}\right\} \tag{35}$$

where c (the denominator of Eq. (34) is a normalization factor ensuring that the *a posteriori* pdf sums one, K is the number of temporal samples used in CM estimation Eq. (20) whereas, γ is the ratio applied in the DS Power component in the exponent while estimating the *a posteriori* pdf. Traditionally, in simulation involving experiments for array signal processing γ factor is set to be 0.3 (BELL et al., 2000; LAM; SINGER, 2006).

Based on Eq. (33), the weight vector of the Bayesian based beamformer is expressed as in Eq. (36).

$$\vec{w}_{MV\text{-}BY}(k) = \sum_{i=1}^{L_k} p(\theta_i|x)\vec{w}_{MV}(k) \tag{36}$$

The main idea of the Bayesian-based beamformer is combining the MV weight with the *a posterior* pdf to form the beamforming output $z_{MV\text{-}BY}(k)$ as in Eq. (37).

$$z_{MV\text{-}BY}(k) = \vec{w}_{MV\text{-}BY}(k)^H\vec{x}(k) \tag{37}$$

The motivation of choosing the MV as the core of adaptive processing is that it represents a distortionless beamformer and therefore it does not affect the signal amplitude power while minimizing the corresponding noise power (NILSEN; HOLM, 2010).

In order to improve the performance of US imaging using adaptive processing, we propose the implementation of MV-BY beamformer expressed in accordance with the Eqs. (36) and (37), respectively, as presented in Chapter 3.

The MV-BY beamformer is then combined with the Eq. (27) in order to design an effective WPF Eq. (42) for adaptive processing of ultrasound imaging using CPWC.

The effectiveness of the proposed method for spatial resolution and image contrast is demonstrated using simulation, phantom experiment, and *invivo* experiment dataset.

3 THE PROPOSED METHOD

The Bayesian-based beamformer for adaptive array processing of medical ultrasound imaging is suggested in accordance with Section 2.4.

This method is formulated by weighting the *a posteriori* pdf with the MV beamformer output (BELL et al., 2000; LAM; SINGER, 2006).

Additionaly, this beamformer was implemented by Bell et al. (2000) and Lam and Singer (2006) as formulated in Eq. (41).

Plane wave imaging is low SNR due to the lack of focusing in the pulse emission Wang and Li (2014), Zhao et al. (2015) and the Bayesian beamformer has improved the signal estimation accuracy over different scenarios of SNR Bell et al. (2000), Lam and Singer (2006) and therefore, we believe that it should introduce improvements in image quality.

An interesting aspect is that the Bayesian-based beamformer results to US imaging have never been presented in the area of ultrasound imaging and, therefore we suggest the first implementation.

This beamformer represents a post-filter to MV beamformer and is suggested to improve the array noise suppression abilities. We believe that it can improve the ultrasound image quality in CPWC imaging.

In practice, the Bayesian-based beamformer introduces improvements in the estimation of desired signal s_d. This beamformer is obtained by combining (i.e., weighting) the MV beamformer output with a post-filter (i.e., the *a posteriori* pdf $p(\theta_i|x)$ estimated from data in accordance with the Eq. (38) (BELL et al., 2000; LAM; SINGER, 2006).

Therefore, for implementation in the field of US umaging, the array data processing is performed taking into account a subarray structure adopted for adaptive processing of US image so that a subarray steering vector of $\vec{a}(\theta_i) = \vec{a}_{Lx1}$ is adopted.

In accordance with Eq. (34), data samples are uniformly distributed with *a priori* $p(\theta_i)$ distribution of $p(\theta_i) = 1/L_k$ (i.e., L_k represents the amount of temporary samples in the imaging measurement grid). The *a posteriori* pdf estimate is formulated

as in Eq. (38).

$$p(\theta_i|x) = cp(\theta_i)\mathbf{exp}\Big\{\gamma_{SNR}D(\vec{a}(\theta_i)^H R^{-1}\vec{a}(\theta_i)^{-1})\Big\} \tag{38}$$

where c is a normalization factor ensuring that the *a posteriori* pdf sums one.

Recall that D denotes the number of temporal samples used in CM estimation Eq. (20) whereas, $\gamma_{SNR} \in (0,1)$ is the function of signal to noise ratio (SNR) which in this work is data-dependent obtained from the components σ_s^2 and σ_n^2 of Eq. (27) and is formulated as in Eq. (39).

$$\gamma_{SNR} = \frac{\sigma_n^2}{\sigma_s^2} = \frac{\vec{w}_{MV}^H R_n \vec{w}_{MV}}{\vec{w}_{MV}^H R \vec{w}_{MV}} \tag{39}$$

From Eq. (36) and Eq. (40) we can represent the weight vector of MV-BY beamformer $\vec{w}_{MV\text{-}BY}$ as in Eq. (40) as well as the beamformer output Eq. (41).

$$\vec{w}_{MV\text{-}BY}(k) = \sum_{i=1}^{L_k} p(\theta_i|x)\vec{w}_{MV}(k) \tag{40}$$

$$z_{MV\text{-}BY}(k) = \vec{w}_{MV\text{-}BY}(k)^H \vec{x}(k) \tag{41}$$

The *a posteriori* pdf is combined with the MV beamformer resulting in MV-BY beamformer. Additionaly, the MV-BY beamformer method is combined with the WPF approach to formulate the MV-BY-WPF beamformer which is presented in Eq. (42).

In complement to Table 2, Fig. 14 presents the diagram of the proposed methodology.

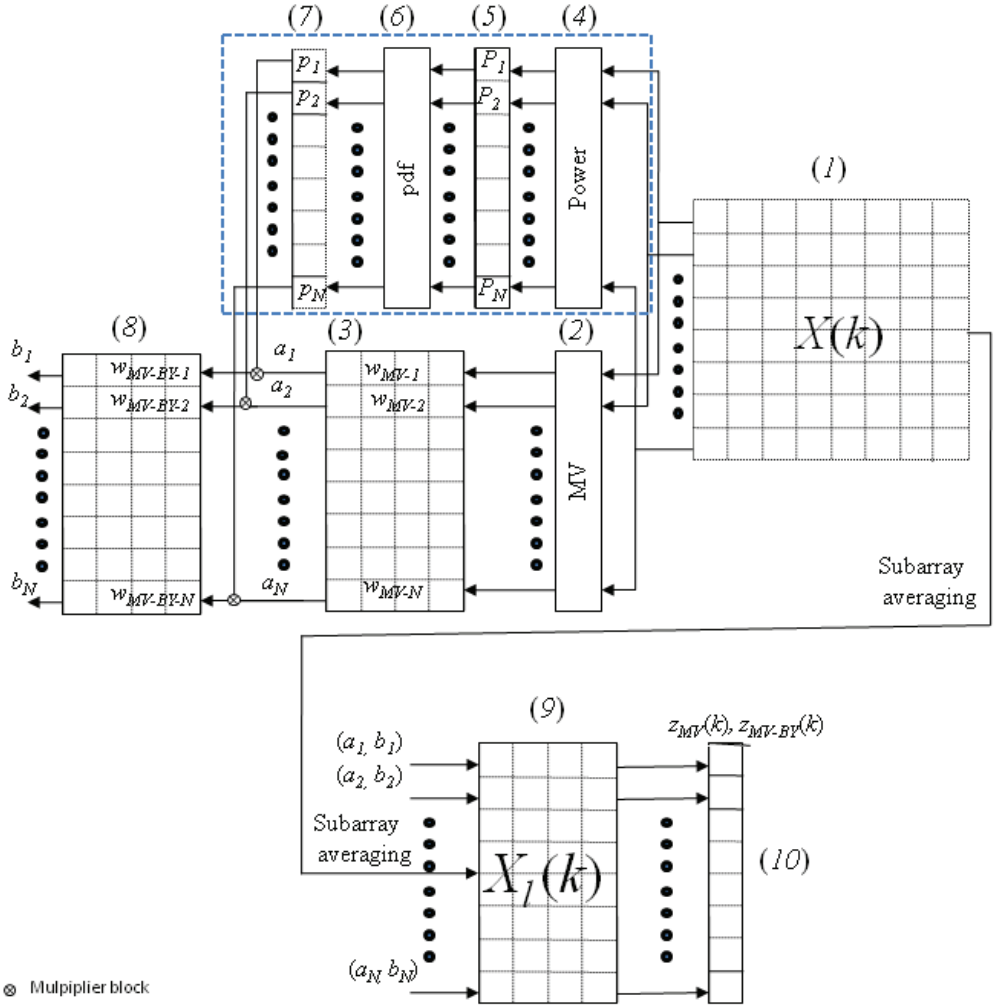

Figure 14: The Bayesian based post-filter scheme which is used for designing the MV-BY-WPF beamformer. The upper branch dashed in blue represents the a posteriori pdf coefficients calculation.

In Fig. 14, the highlighted steps can be described as follows: **Label (1)** presents samples of collected data X for N emmissions and M array sensors as in Eq (12), **Label (2)** presents the MV estimator, **Label (3)** presents a set of MV weight vectors w_{MV} for each emission, **Label (4)** presents the Power output (estimator), **Label (5)** presents the DS Power output values of DS, P for each emission which are combined with the steering vector to derive the **Label (6)** (the pdf estimator).

Additionally, **Label (7)** presents the *a posteriori* pdf coefficients, p for each emission which are combined with the MV weight vector, to form the MV-BY beamformer, **Label (8)** presents a set of MV-BY weight vectors, w_{MV-BY} and **Label (9)** presents the subarray averaged dataset X_l which is combined either with a set of MV weight vectors w_{MV}, **Label (3)** or a set of MV-BY weight vectors w_{MV-BY}, **Label (8)** to form the beamformer output **Label (10)**, as indicated by symbols **a** and **b**, respectively.

In labels (3) and (8), the symbols **a** and **b** are used to represent the combination between the adaptive weights using the MV and the MV-BY beamformers, respectively.

The difference between Fig. 14 and the diagram shown in Fig. 13, is that this diagram presents additional elements (i.e., the upper branch dashed in blue) which represents the *a posteriori* pdf coefficients calculation.

3.1 THE MV-BY-WPF IMPLEMENTATION PROCEDURE

The key steps for implementation procedures of the proposed beamformers are summarized in Table 2. For the sake of clarity, the performance of the proposed methods (BY, MV-BY and MV-BY-WPF) is ranked together with the following methods: DAS, MV, CF, MV-CF, and MV-WPF, respectively.

Table 2: The Bayesian minimum variance (MV-BY) beamformer algorithm

A:	For each emission, the raw data x_{CPWC} Eq. (8) are collected based on the superposition principle. For each imaging point, the time delay is calculated and then combined with the corresponding signal. A collection of signals in Eq. (8) are grouped in order to form a 2-D data matrix as in Eq. (12).
B:	Obtain the estimate the data covariance matrix (CM) R Eq. (20) and, apply the diagonal loading (DL) method Eq. (20).
C:	Calculate the minimum variance (MV) beamformer weight Eq. (17) using the CM estimate and the steering vector.
D:	Estimate the *a posteriori* pdf $p(\theta_i\|x)$ Eq. (35) using the power of desired signal and the *a priori* pdf $p(\theta_i)$.
E:	Calculate the Bayesian minimum variance (MV-BY) beamformer output $z_{MV-BY}(k)$ as in Eq. (37).
F:	Calculate the R_n using Eq. (29) taking into consideration the signal $z_{MV-BY}(k)$ as the coherent energy component.
G:	Calculate the (MV-BY-WPF) beamformer using Eq. (42).

The MV-BY-WPF can be formulated in analogy to Eq. (27) and Eq. (30) and is presented in Eq. (42).

$$z_{MV\text{-}BY\text{-}WPF} = \frac{\vec{w}^H_{MV\text{-}BY} R \vec{w}_{MV\text{-}BY}}{\vec{w}^H_{MV\text{-}BY} R \vec{w}_{MV\text{-}BY} + \vec{w}^H_{MV\text{-}BY} R_n \vec{w}_{MV\text{-}BY}} =$$

$$= \frac{|z_{MV\text{-}BY\text{-}WPF}|^2}{|z_{MV\text{-}BY\text{-}WPF}|^2 + \vec{w}^H_{MV\text{-}BY} R_n \vec{w}_{MV\text{-}BY}} \tag{42}$$

The weight vector and the beamformer output can be formulated as in Eq. (43) and Eq. (44), respectively.

$$\vec{w}_{MV\text{-}BY\text{-}WPF} = H_{MV\text{-}BY\text{-}WPF} \vec{w}_{MV\text{-}BY} \tag{43}$$

$$z_{MV\text{-}BY\text{-}WPF}(k) = \vec{w}^H_{MV\text{-}BY\text{-}WPF} \vec{x}(k) \tag{44}$$

The estimate of R_n in Eq. (42) is obtained based on inserting the MV-BY beamformer output Eq. (44) to the covariance matrix estimator R in Eq. (29).

After following all the procedures described in Table 2, we form the image pixel using MV-BY. Additional, we place the obtained weigh vector in Eq. (27) into Eq. (30) to form the MV-BY-WPF. The process is repeated for each imaging point to get the final beamformed image which is displayed in the Dynamic Range (DR) of 60 dB.

3.2 EVALUATION PROCEDURES

3.2.1 DATASET

Evaluation procedures will be performed in accordance with the available dataset in the following order:

3.2.1.1 SIMULATION AND PHANTOM DATA ACQUIRED ON LABORATORY

Figures 15 represent the experimental data acquiring infrastructure camposed by (a) the Verasonics US system, (b) the phantom model 84-317, (c) The linear array transducer model L11-4v and (d), the phantom model 040GSE.

Figure 16 represents the scanning regions for both phantoms used for experimental data acquiring. In (a) for multipurpose phantom model-84-317 and, (b), the phantom 040GSE.

Figure 17 represents the scanning regions covered by the linear transducer array. (a) scanning region for data simulation using the Verasonics US system (SIMU), (b) the hypoechoic target, (c) the anechoic cyst, (d) a set of hypoechoic targets and,

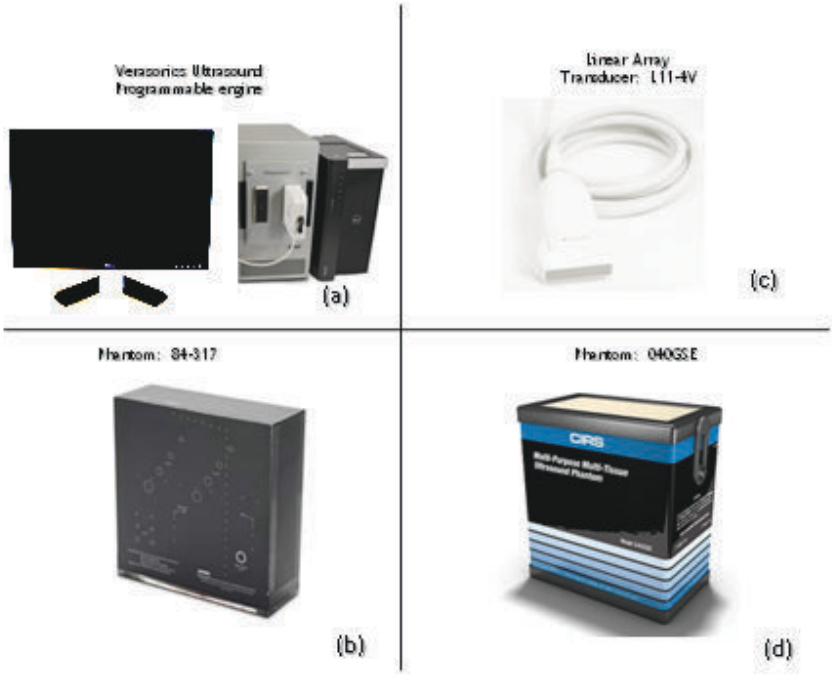

Figure 15: The experimental data acquiring infrastructure campused by (a) the Verasonics US system, (b) the phantom model 84-317, (c) the linear array transducer model L11-4v and (d), the phantom model 040GSE.

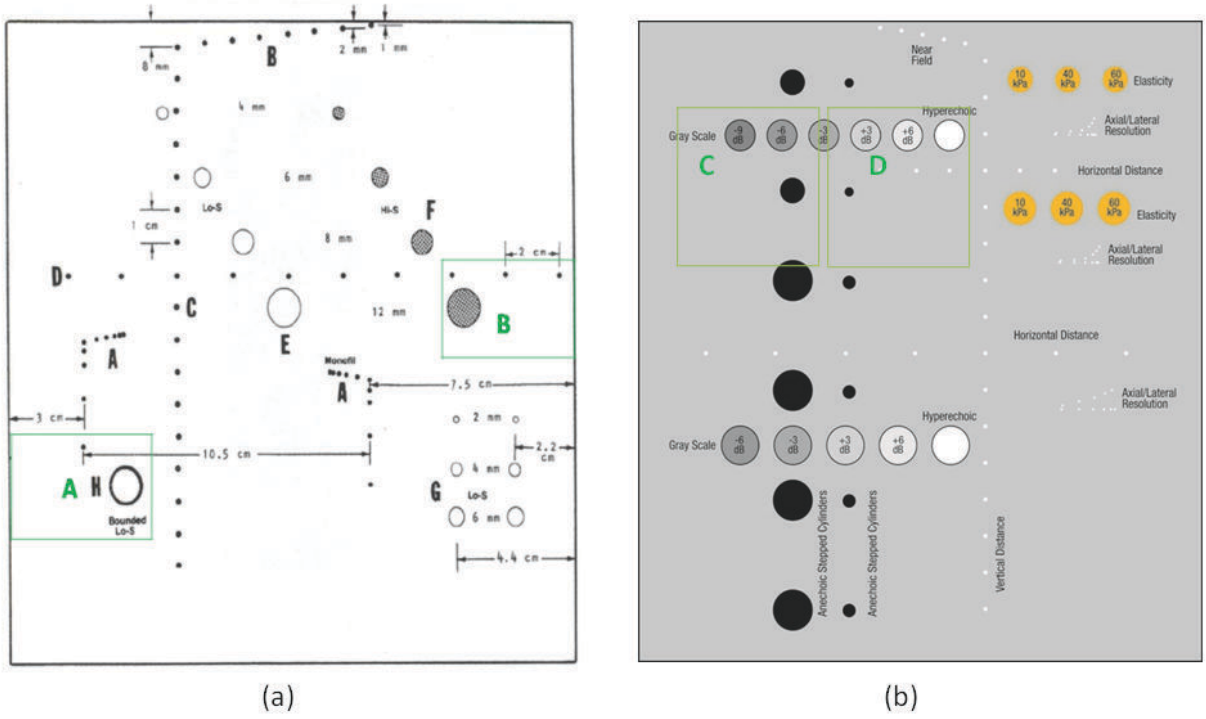

Figure 16: The scanning regions for (a) multipurpose phantom 84-317 and (b) 040GSE phantom used for experimental data acquiring.

(e) a set of anechoic cysts.

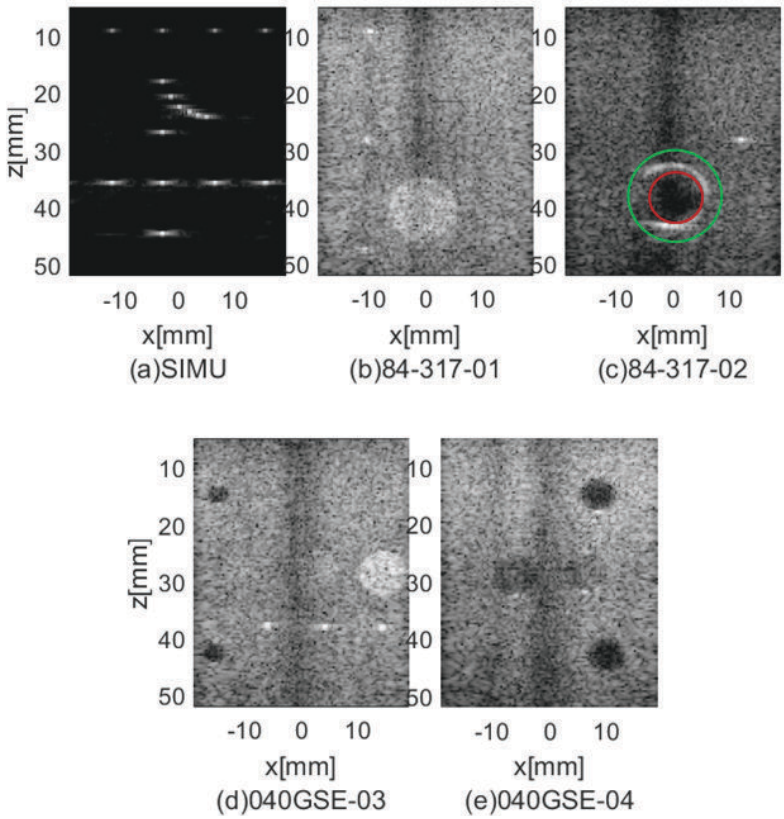

Figure 17: The scanning regions covered by the linear transducer array. (a) Scanning region for data simulation using the Verasonics US system, (b) the hypoechoic target, (c) the anechoic cyst, (d) a set of hypoechoic targets and, (e) a set of anechoic cysts.

3.2.1.2 SIMULATION AND PHANTOM DATA AVAILABLE ON PICMUS PLATFORM

To evaluate the performance of the proposed method we use the simulation and phantom datasets.

3.2.1.3 HUMAN *IN-VIVO* DATA AVAILABLE ON PICMUS PLATFORM

To evaluate the performance of the proposed method we use the human *in-vivo* datasets available. A complete description is given in Table 3. In total, an amount of 75 plane wave sequences were acquired for each case.

The highlighted regions in Fig. 18 were used for evaluation of the performance of the proposed methods while the regions in red in S1 show the points reflectors used for spatial resolution (axial or lateral) evaluation.

Table 3: Dataset presentation for evaluation of the proposed methodology

I:	**The simulated dataset available in PICMUS**: Dataset from simulated phantom reflector for spatial resolution evaluation and anechoic cyst phantom with several anechoic cysts for contrast speckle analysis were made available in PICMUS (LIEBGOTT et al., 2016). Such data were acquired using Field II (JENSEN, 1996b). The corresponding images are presented in Fig. 18 (a) and Fig. 18 (b).
II:	**The phantom dataset available in PICMUS**: Such dataset include both resolution and contrast was recorded using CIRS Multi-Purpose Ultrasound Phantom (Model 040GSE). The data acquiring was performed with a scan region with anechoic cyst, hypo-echoic target and a point reflector. The corresponding images are presented in Fig. 18 (c) and Fig. 18 (d).
III:	**The phantom dataset acquired in UTFPR-Brasil Lab**: Both the contrast speckle dataset and the resolution distortion dataset were experimentally acquired using a Fluke Multi-Purpose ultrasound phantom model 84-317 Fig. **??** (b) and Fig. **??** (c) and the CIRS Multi-purpose ultrasound phantom (Model 040GSE) Fig. **??** (d) and Fig. **??** (e) available in Ultrasound Laboratory of UTFPR-Brazil. The corresponding scan regions, among anechoic cysts, hypo-echoic targets contains several point reflectors instead of that collected from Verasonics working at simulation mode (SIMU) as depicted in Fig. **??** (a). The corresponding images are presented in Fig. **??**.
IV:	**The human *in-vivo* dataset available in PICMUS**: The proposed methods are examined on two *in-vivo* datasets of a carotid artery (CA) i.e., cross sectional CA and longitudinal CA, respectively. This allows for more practical and realist analysis either in terms of qualitative or quantitative assessment of the proposed methodology. The corresponding images are presented in Fig. 18 (e) and Fig. 18 (f).

The highlighted anechoic regions in S2 were used for contrast evaluation while the regions in blue were used for speckle evaluation.

In PH1, only the spatial resolution was evaluated while in PH2, the contrast, In H1 and H2 both contrast (green box leftmost and red box) and speckle have been evaluated in order to test the abilities of our proposed methodology.

3.2.2 COMPARISON BETWEEN DIFFERENT BEAMFORMERS

In order to examine the performance of the proposed beamformers, we used PICMUS dataset for qualitative and quantitative analysis. The PICMUS dataset includes simulation, phantom and human *in-vivo* dataset. Additionally, we have acquired phantom data using Verasonics ultrasound imaging system in UTFPR-Brazil Laboratory for qualitative analysis. The performance of MV-BY and MV-BY-WPF is

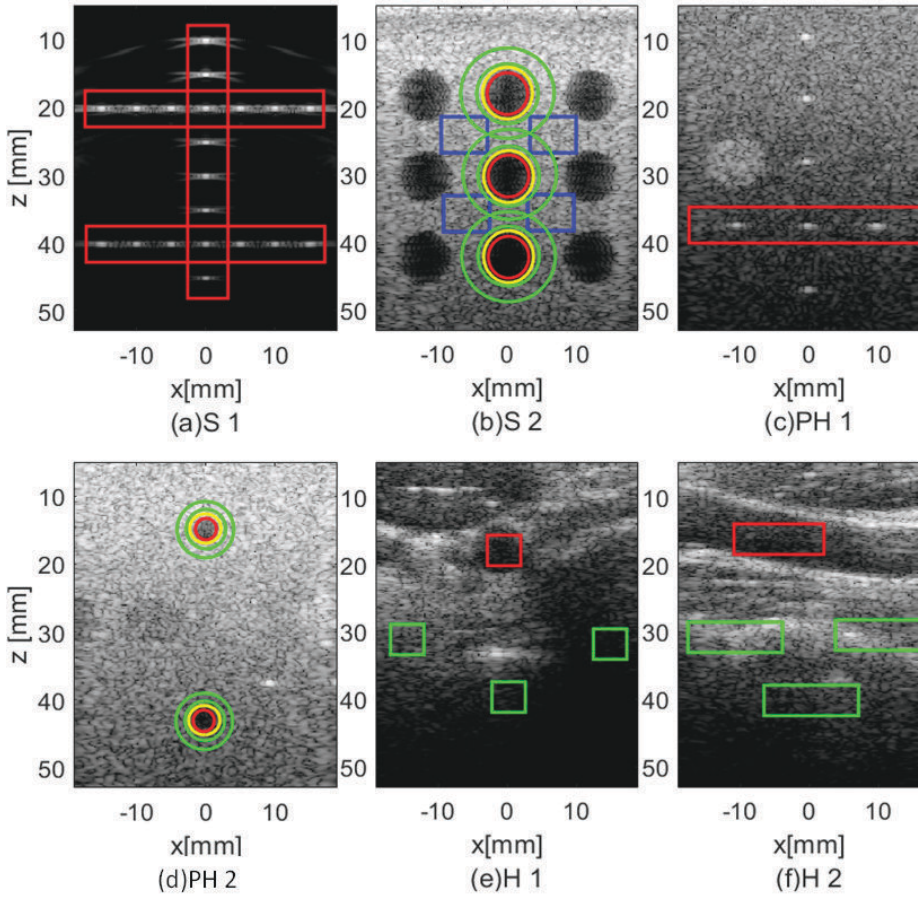

Figure 18: Dataset from PICMUS for a total amount of 5 plane wave elements: (a) Simulation phantom data for point reflector (S1) (b) Simulation data phantom data for speckle contrast (S2),(c) Phantom experimental data (PH1), (d) Phantom experimental data for contrast speckle (PH2), (e) Human *in-vivo* data for cross-sectional CA (H1) , (f) Human *in-vivo* data for longitudinal CA (H2), respectively.

compared to the following methods:

1. The DAS beamformer as in Eq. (19);
2. The MV beamformer Eq. (18) which represents the core of adaptive beamforming in this study;
3. The CF-based method is a post-filter beamformer Eq. (22) and is suggested in order to provide support in terms of the theoretical framework of the proposed methods. In this context, the CF weights are combined with the DAS beamformer output;
4. The BY beamformer Eq. (34) and Eq. (35) was implemented in order to test the weighting abilities of the *a posteriori* pdf coefficients (i.e., the post-filter) when directly applied to the time-delayed version of received data. The *a posteriori* pdf

post-filter has been combined with Eq. (19) to form BY beamformer;

5. The MV-CF beamformer was suggested in order to compare the MV beamformer when combined with the CF-based post-filter designed for adaptive processing. In this context, the CF for adaptive processing weights the MV beamformer output and,

6. The MV-WPF beamformer Eq. (30) which was suggested in order to provide a fair comparison with the proposed (i.e., MV-BY-WPF) in Eq. (42).

The MV-BY-WPF beamformer is compared with the MV and MV-BY with particular importance.

The main difference between the MV and the MV-BY is that the MV-BY beamformer has been combined with the *a posteriori* pdf coefficients which represent a post-filter applied to MV beamformer. Likewise, the difference between the MV-BY-WPF beamformer with the MV-WPF beamformer is that the former has been designed using an input signal of interest the MV-BY beamformer output while the latter has applied the standard MV output.

3.2.3 DETAILS FOR ADAPTIVE PROCESSING

Table 4 presents the most important parameters used for adaptive processing in this work.

Table 4: Important parameters for simulated and experimental (real phantom and *in-vivo*) for acquisition and data processing.

Imaging parameters	Simulation	Experimental/human *in-vivo*
Central, Sampling frequencies	5.2 MHz, 20.8 MHz	5.2 MHz, 20.8 MHz
Transducer model	L11-4v	L11-4v
Number of Elements (NE)	128	128
NE for emission, reception	128, 128	128, 128
Subarray length (L)	$30\%128 \approx 38$	$30\%128 \approx 38$
Sound speed	1540 m/s	1540 m/s
Fractional bandwidth	60 %	60 %
pich	0.3 mm	0.3 mm
F-Number	1.75	1.75
Range, angles	-16° to 16°, 75	-16° to 16°, 75
Data acquiring	from Field II	040GSE/84-317
Diagonal loading	$\Delta = 20$	$\Delta = 10$

All the beamformers applied in this work were implemented and evaluated using Matlab R2016b (Mathworks Inc. Natick, MA, USA) on a desktop PC (Windows 10, 64-bit system, Intel T6600 with 2.2 GHz, and 6 GB Memory).

3.2.4 EXPERIMENTAL EVALUATION SETUP

All the simulation, phantom, and human *in-vivo* dataset are acquired with a 128 element probe and central transducer frequency of 5.2 MHz. Additional information can be found in Table 4 or accessed on the PICMUS website.

All the image data acquisition (simulated, phantom and human *in-vivo*) includes transmission of 75 plane wave firing elements with steering angles spaced uniformly between -16° to 16° with a gap of 0.5°. All the acquisition has been performed with am *F-Number* of 1.75.

In accordance with Table 4, for adaptive processing, a subarray of 30% of 128 elements is approximately 38 array elements used for each update step while computing the adaptive weights.

Either in transmit or the receive no apodization was applied.

3.3 EVALUATION METRICS

Figures 19 and 20 were generated using Field II together with the DAS method.

In Fig. 19 its presented an example of imaging regions where the spatial resolution, contrast and speckle pattern measures are performed: In Fig. 19 (a), the central circular anechoic cyst shows the region inside cyst, region outside cyst for CR and CNR evaluation using Eq. (45) and Eq. (46).

The blue box shows the highlighted region for background speckle pattern evaluation. In Fig. 19 (b) the point scatterers and the highlighted region in red box shows an example of point reflector examined in order present the lateral profile whose plots were presented in Fig. 19 (c).

3.3.1 SPATIAL RESOLUTION

The spatial resolution evaluation is done by computing full width at half maximum (FWHM) of point spread function in the axial and lateral directions. The

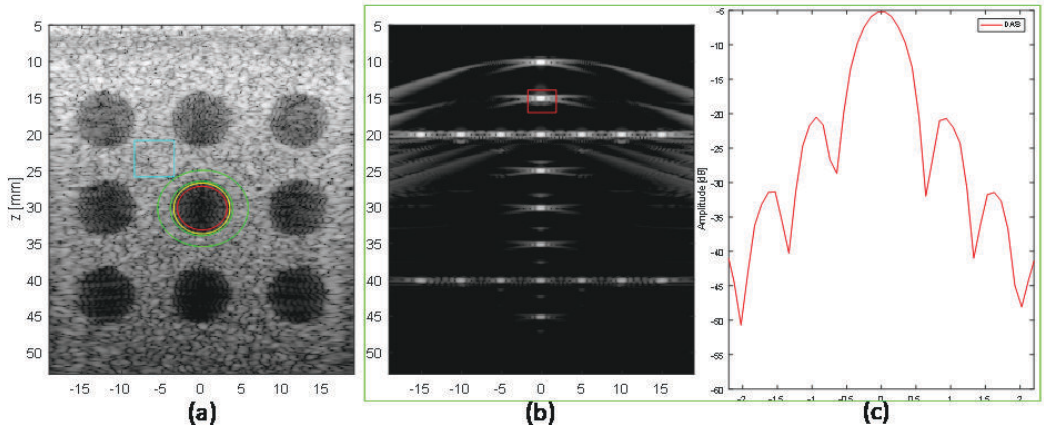

Figure 19: Example of imaging regions where the spatial resolution, contrast and speckle pattern measures are performed: (a) The central circular anechoic cyst shows the region inside cyst, region outside cyst for CR and CNR evaluation using Eq. (45) and Eq. (46). The blue box shows the highlighted region for background speckle pattern evaluation; (b) shows the point scarters and the highlighted region in red box shows an example of point reflector examined in order present the lateral profile whose plots were presented in (c).

FWHM defines the beam width of the main lobe at -6 dB. Figure 19 (b) and (c) respectively, shows the point reflector (i.e., in red) and the equivalent lateral profile.

3.3.2 CONTRAST

For contrast evaluation and speckle statistics assessment, the CR and CNR are formulated as in Eq. (45) and Eq. (46), respectively (ZHAO et al., 2016).

$$CR = \left|\varphi_{cyct} - \varphi_{bck}\right| \tag{45}$$

$$CNR = \frac{\left|\varphi_{cyct} - \varphi_{bck}\right|}{\sqrt{\sigma^2_{cyst} + \sigma^2_{bck}}} \tag{46}$$

where φ_{cyst}, is the mean intensity (before log-compression) in the cyst and φ_{bck}, is the mean intensity in the speckle, σ^2_{cyst} is the variance of intensitie inside cyst and, σ^2_{bck} is the variance of intensitie in the background, respectively (HVERVEN et al., 2017). For illustration, the corresponding regions are shown as an example in Fig. 19 (a).

3.3.3 SPECKLE STATISTICS

In order to compare the effect of MV-BY and MV-BY-WPF and other interference suppression methods on speckle, we evaluated the speckle in a specific area within the images obtained by different methods. The corresponding areas are

highlighted in Fig. 18.

All the regions subject to speckle pattern evaluation are highlighted in rectangular boxes and have been independently evaluated to ensure that the follow the Rayleigh Distribution (RD).

In such context, it is examined if the speckle pattern of the beamformed data follows the RD by performing the hypothesis test (ks-test 5% significance) and, the test is decided when the computed p-value is compared with the indicated value in the pre-defined significance interval 2016.

The corresponding results are presented in Fig. 30. In order to quantify the similarity, the speckle region of the DAS image has been adopted as a reference and calculates the percentage of the rest of the speckle pattern produced by different adaptive beamformers.

The SNR which represents the measure of image speckle can be expressed as in Eq. (47) (HVERVEN et al., 2017).

$$SNR = \frac{\varphi_{bck}}{\sigma_{bck}} \tag{47}$$

Additionally, the Rayleigh probability density function (pdf) of envelope detected data of a beamformer can be used as complement of speckle evaluation of a specific image region is formulated as in Eq. (48).

Generally, the envelope detected data for DAS beamformer show SNR of 1.91 and the corresponding pdf is expressed as in Eq. (48) and, follows closely the Theoretical Rayleigh Distribution (TRD) (SZABO, 2004b; ZHAO et al., 2016).

$$p(\varphi_{bck}) = \left(\frac{2\varphi_{bck}}{\overline{\varphi_{bck}}^2}\right)\mathbf{exp}\left(\frac{-\varphi_{bck}}{\overline{\varphi_{bck}}^2}\right) \tag{48}$$

where $\overline{\varphi_{bck}}^2$ is the mean of the squared amplitude. Since the adaptive processing introduce significant changes in the speckle statistics of beamformed data, in this work we have examined the beamformed data to ensure that it follows the Rayleigh Distribution (RD) using the hypothesis test (**ks**-test 5% significance) which allows decide if the computed p-value are in accordance with the significance interval (ZHAO et al., 2016).

Figure 20 was obtained from envelope detected data in blue box of Fig. 19 (a).

It presents and compares the TRD with the RD obtained using DAS beamformer for simulated data acquired from Field II simulation program in a DR of 60 dB.

The RD can show the normalized intensity distribution as well as their probabilities for beamformed data.

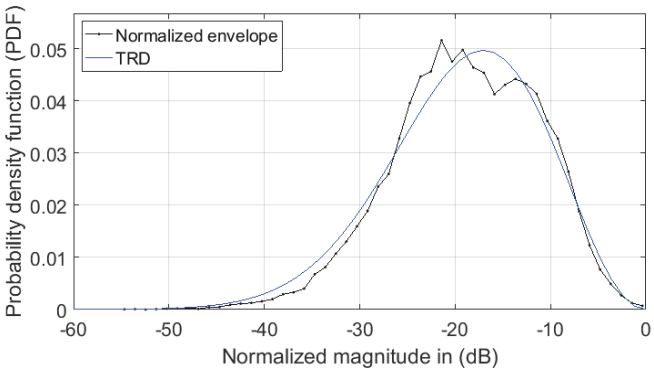

Figure 20: Illustration of theoretical pdf for speckle assessment.

For data processing, we used only 5 plane wave sequences centered at zero degree. We only used a total amount of sequences for comparison in order to demonstrate the benefits of our proposed methodology.

In Fig. 18 the highlighted regions were used for evaluation of the performance of the proposed methods. In S1 the highlighted regions in red illustrate that all the points reflectors were used for spatial resolution (axial or lateral) evaluation.

In S2 the highlighted anechoic regions were used for contrast evaluation while the highlighted in blue were used for speckle evaluation.

4 RESULTS

Different point targets and circular anechoic cysts were generated in a simulated media to test the capabilities of our proposed beamformers. Additionaly, data captured using the available in US system on Laboratory and phantom together with the *in-vivo* data are applied.

4.1 RESULTS FOR SIMULATION PHANTOM DATA FOR POINT REFLECTORS (S1)

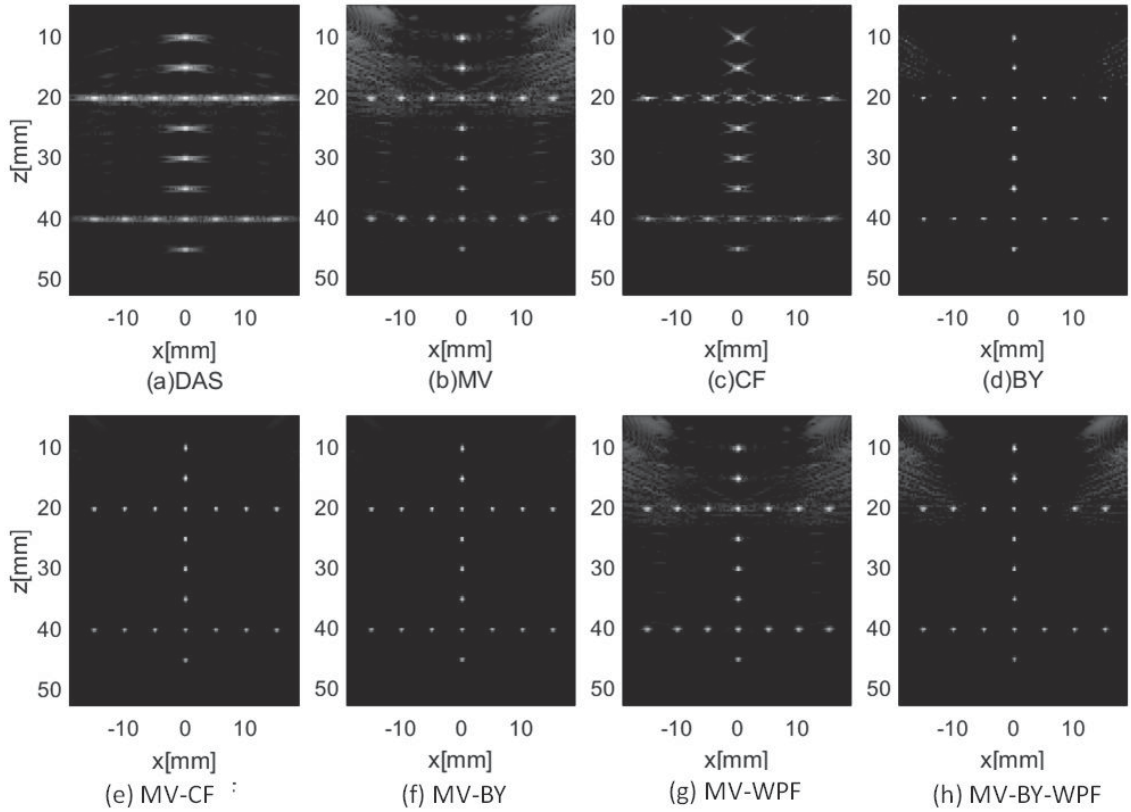

Figure 21: Images of simulated point-reflector phantom S1 obtained by: (a)DAS, (b)MV, (c)CF, (d) BY, (e)MV-CF, (f)MV-WPF and, (g)MV-BY-WPF. All the images are displayed with a DR of 60 dB. The lateral profiles are presented Fig. 22.

Table 5: Spatial resolution ($FWHM_{ax}$, $FWHM_{lat}$) for simulated S1.

Beamformer	$FWHM_{ax}$ [mm]	$FWHM_{lat}$ [mm]
DAS	0.43	0.55
MV	0.42	0.53
CF	0.41	0.52
BY	**0.40**	**0.51**
MV-CF	0.41	0.51
MV-BY	0.42	0.53
MV-WPF	0.41	0.51
MV-BY-WPF	0.41	0.51

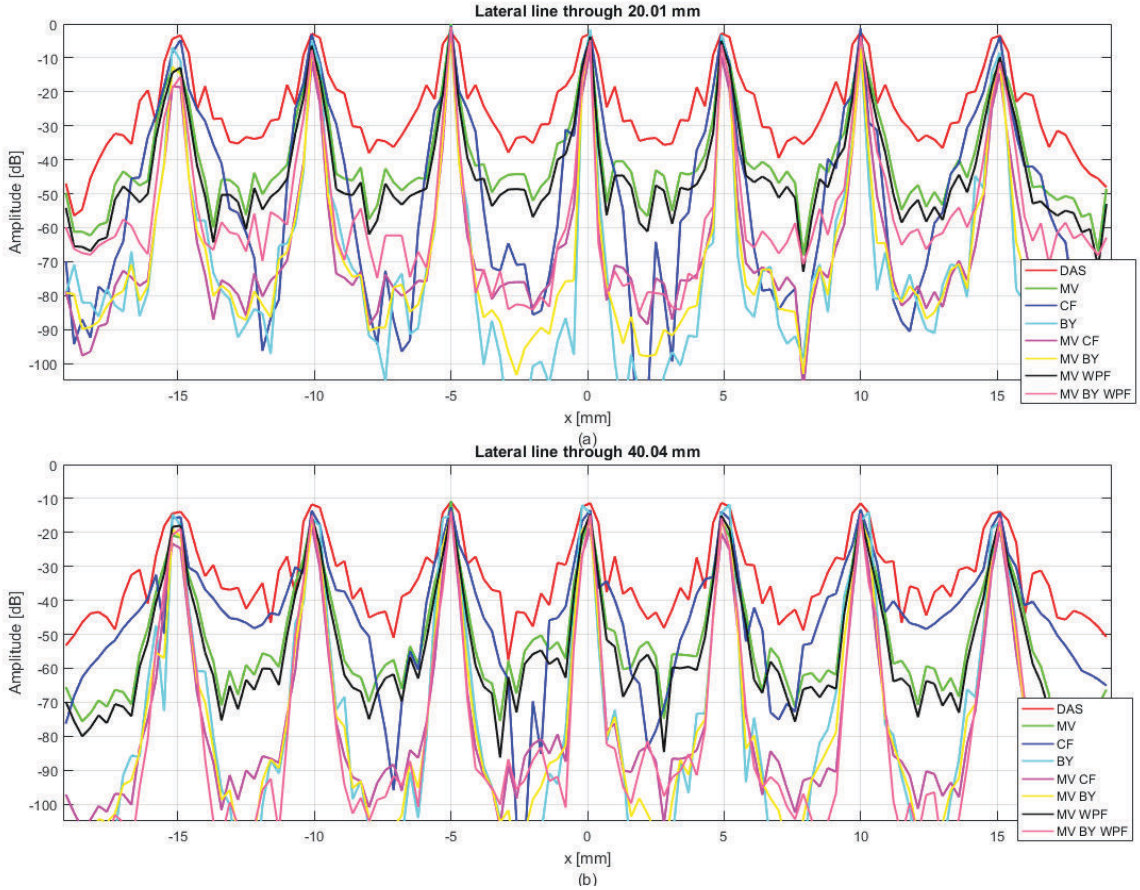

Figure 22: The lateral profiles of the displayed images in Fig. 21 at different imaging depths: (a) The lateral profile through 20 mm depth and (b) The lateral profile through 40 mm depth, respectively.

Table 5 presents the average of $FWHM_{ax}$ in axial direction and $FWHM_{lat}$ in lateral direction for simulated point targets. The results of the average of

$FWHM_{ax}$/$FWHM_{lat}$ in the highlighted region in S1 provided the following values in [mm] (0.43, 0.42, 0.41, 0.40, 0.41, 0.42, 0.41, 0.41)/(0.55, 0.53, 0.52, 0.51, 0.51, 0.53, 0.51, 0.51).

Taking DAS as reference, the FWHM reduction in percentage using Eq. (49) in both directions (i.e., $FWHM_{ax}$/$FWHM_{lat}$) for MV, CF,BY,MV-CF, MV-BY, MV-WPF and MV-BY-WPF showed respectively the following values (0.94, 3.76, 6.10, 3.76, 1.88, 3.52, 4.93)/(3.67, 5.50, 6.97, 5.69, 3.67, 6.61, 5.87).

$$\Delta_{FWHM(\%)} = \frac{FWHM - FWHM_{ref}}{FWHM_{ref}} x100 \tag{49}$$

where ref stands for $reference$, and $\Delta_{FWHM(\%)}$ represents either $FWHM_{ax}$ or $FWHM_{lat}$ in percentage taking DAS as reference. In the other words, we can say that the average of width of the main lobe at -6 dB have reduced for different beamformers compared to the DAS beamformer.

Following the above mentioned results, we notice that, all the point reflector showed an improved difinition for different beamformers compared to DAS beamformer. Additionaly, among different adaptive beamformers, the CF, MV-CF and MV-WPF presented the well defined point reflectors.

We can notice that the spatial resolution has subtle improvement represented by a slight reduction of the average of the main lobe in both directions. Among the adaptive BF, the $FWHM_{ax}$ and $FWHM_{lat}$ improvements are present despite being apparently subtle.

However, the array noise suppression abilities are clearly visible so that in lateral profile presented in Fig. 22, the CF-based adaptive methods appear to suppress more noise than their counterparties.

This behavior allows suppressing noise in both directions while preserving the main lobe. However, it is expected that the array noise suppression abilities occur while keeping the most relevant data preserved. The CF-based beamformer for point reflector show enhanced spatial resolution compared to MV and MV-BY at the cost of significant side lobe energy reduction. In this context, the weak image details can also be suppressed which can degrade the image brightness.

However, the WPF beamforming methods show more enhanced resolution mainly when imaging the isolated point reflectors, but the sidelobe reduction was not as much as in CF based beamformers. Furthermore, the most improved lateral side lobe

energy reduction was achieved by MV-BY in comparison with the different beamforming techniques. Fig. 22 show the Beam Responses (BR) using different beamforming techniques for point targets.

4.2 RESULTS FOR SIMULATION DATA FOR ANECHOIC CYST (S2)

The displayed images in Fig. 23 show the responses of beamformed images using different beamformers.

Table 6 presents the average of CR/CNR of the highligted circular anechoic cysts in Fig. 18.

All the adaptive beamformers (MV-CF, BY, MV-CF, MV-BY MV-WPF and MV-BY-WPF) outperformed DAS in terms of CR/CNR.

In accordance with the results obtained from tests, the CR/CNR values were computed in percentage using Eq. (50) and taking DAS as reference values of: (10.49, 64.89, 94.91, 80.57, 14.89, 77.62 and 89.41) / (19.23, 15.71, 19.23, 41.99, 22.44, 42.31 and 51.60) were observed.

$$\Delta_{CR/CNR(\%)} = \frac{CR/CNR - CR/CNR_{ref}}{CR/CNR_{ref}} x100 \tag{50}$$

where ref stands for $reference$ and $\Delta_{CR/CNR(\%)}$ represents either CR or CNR in percentage taking DAS as reference.

Improvements introduced by MV-BY over MV in terms of CR/CNR in percentage were of 3.97/2.68 whereas, MV-BY-WPF over MV-WPF in terms of CR/CNR in percentage were of 6.63/6.53.

Additioanally, in complement to the displayed images and the results presented in Table 6, Fig. 24 presents the lateral profiles of the beamformed images.

For CR and CNR evaluation Eq. (45) and Eq. (46) were used for phantom data while for speckle background evaluation, SNR is complemented by the Rayleigh pdf as presented in Fig. 30 (a), Fig. 30 (b) and Fig. 30 (c).

The corresponding imaging regions for simulated and *in-vivo* data are presented in Fig. 29.

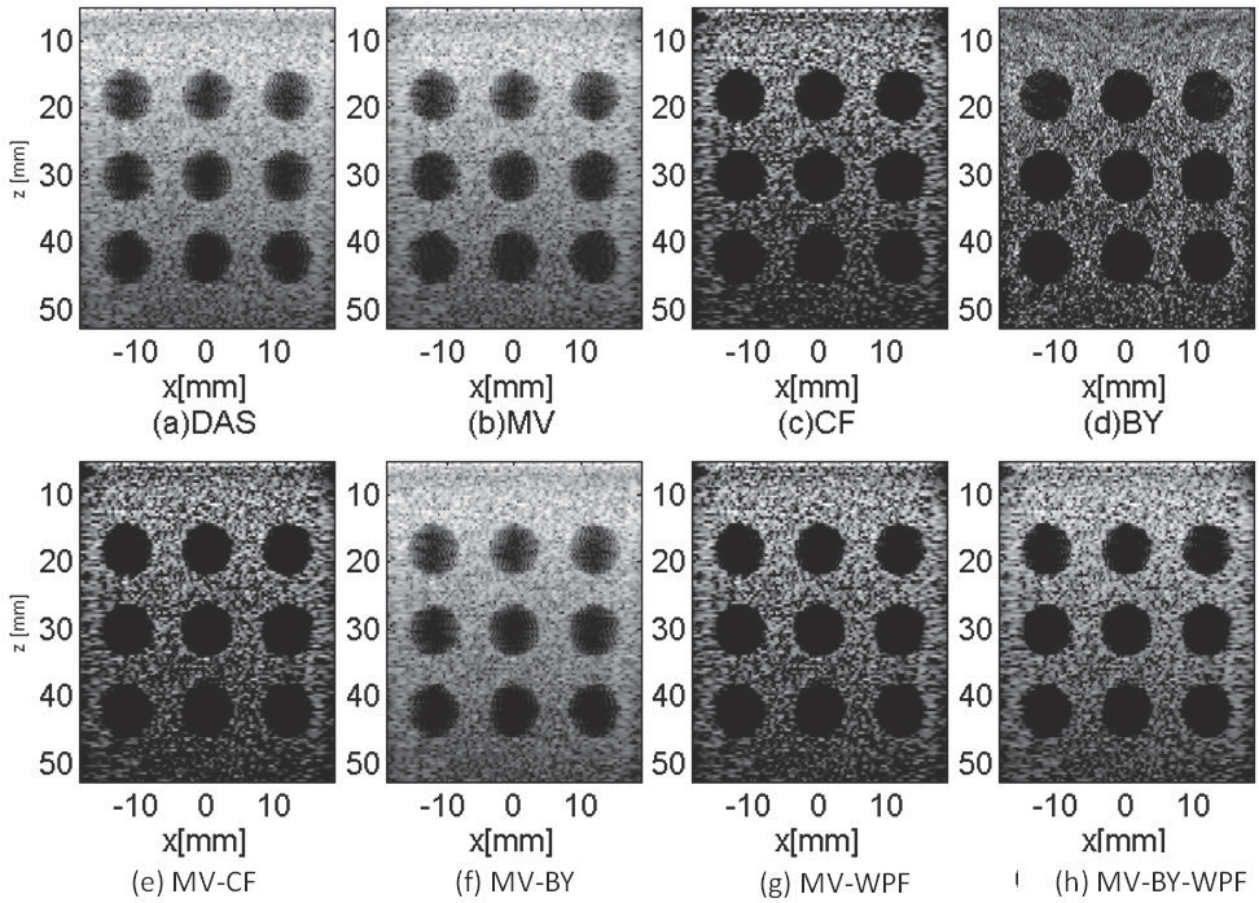

Figure 23: Images of simulated anechoic cyst phantom S2 obtained by: (a) DAS, (b)MV, (c)CF, (d)BY, (e)MV-CF, (f)MV-WPF and, (g)MV-BY-WPF. All the images are displayed with a DR of 60 dB. The corresponding lateral profiles are presented in Fig. 24

Table 6: Contrast CR and CNR for simulated S2 data.

Beamformer	CR [dB]	CNR [dB]
DAS	20.02	3.12
MV	22.12	3.72
CF	33.01	3.61
BY	39.02	3.72
MV-CF	36.15	4.43
MV-BY	24.02	3.82
MV-WPF	35.36	4.44
MV-BY-WPF	38.92	4.61

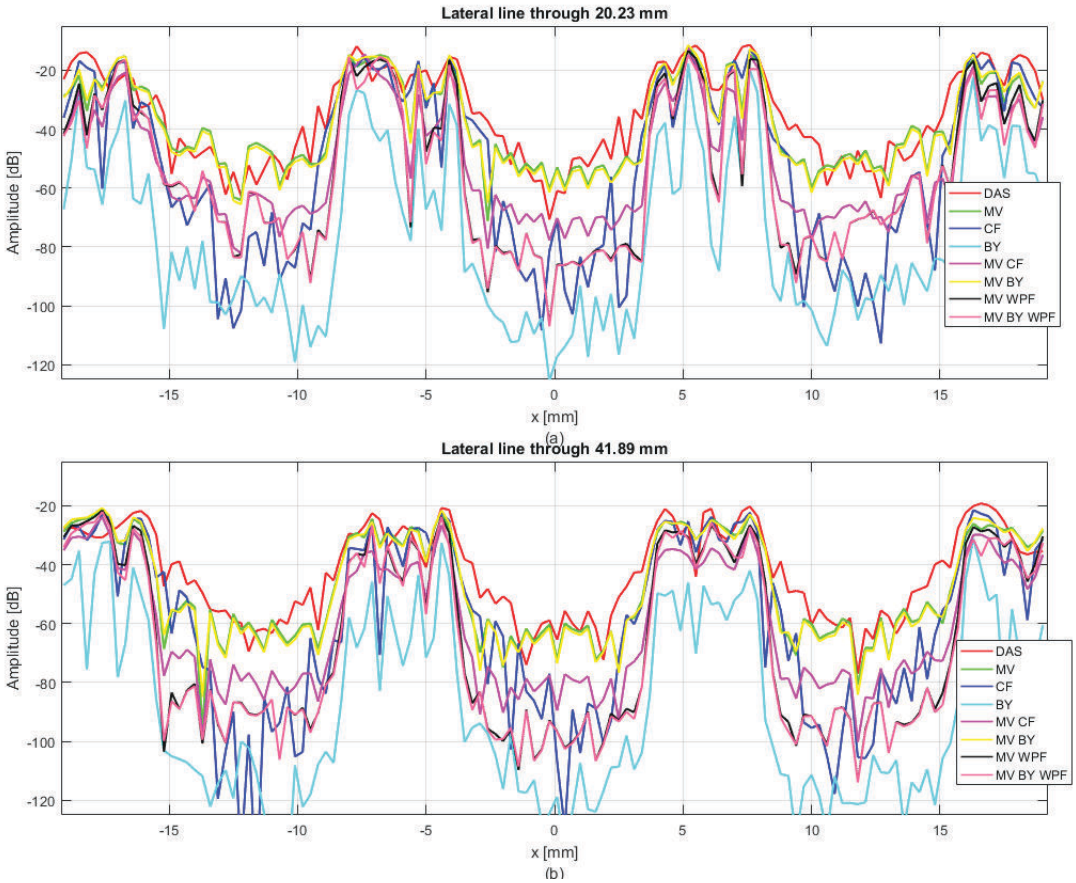

Figure 24: The lateral profiles using simulation data for S2 correspond to the displayed images in Fig. 23 for different beamformers at different imaging depths: (a) the lateral profile through 20 mm and (b) the lateral profile through 41 mm, respectively.

4.3 RESULTS FOR PHANTOM DATA PH1

The displayed images in Fig. 25 show the beamformed responses of different beamformers using phantom data.

Table 7 presents the spatial resolution ($FWHM_{ax}$, $FWHM_{lat}$). In order to evaluate the performance of the proposed beamformers, Table 7 presents results for spatial resolution evaluation.

Fig. 25 show the BR using different beamforming techniques for point targets.

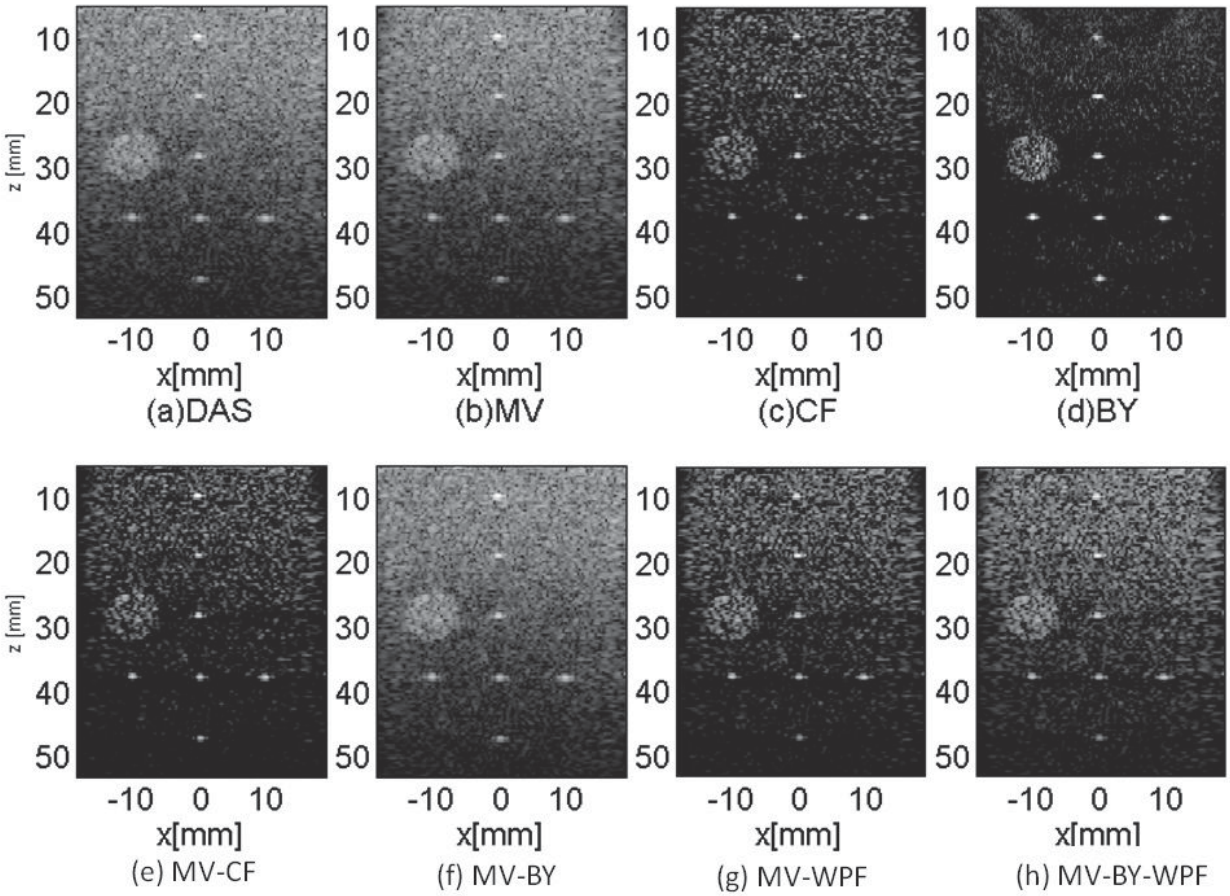

Figure 25: Beamformed images of phantom data PH1 containing hypoechoic cyst with point-reflectors obtained by: (a)DAS, (b)MV, (c)CF, (d)BY, (e)MV-CF, (f)MV-WPF and, (g)MV-BY-WPF. All the images are displayed with a DR of 60 dB.

Table 7: Spatial resolution ($FWHM_{ax}$, $FWHM_{lat}$) for phantom data PH1

Beamformer	$FWHM_{ax}$ [mm]	$FWHM_{lat}$ [mm]
DAS	0.57	0.66
MV	0.54	0.62
CF	**0.52**	**0.61**
BY	0.53	0.62
MV-CF	**0.51**	**0.62**
MV-BY	0.51	0.61
MV-WPF	0.52	0.62
MV-BY-WPF	**0.52**	**0.61**

In accordance with the simulation data, the improvements introduced by adaptive beamformers are visible in terms of the spatial resolution presented in Table

7.

Results of the average of $FWHM_{ax}/FWHM_{lat}$ in the highlighted region in PH1 were computed using Eq. (49) provided the following values in [mm] (0.57, 0.54, 0.52, 0.53, 0.51, 0.51, 0.52, 0.52)/(0.66, 0.62, 0.61, 0.62, 0.62, .61, 0.62, 0.61).

Taking DAS as reference, the FWHM reduction in percentage in both directions (i.e., $FWHM_{ax}/FWHM_{lat}$) for MV, CF, BY, MV-CF, MV-BY, MV-WPF and MV-BY-WPF showed respectively the following values (5.26, 8.77, 7.01, 10.52, 10.52, 8.77, 8.77)/(6.06, 7.57, 6.06, 6.06, 7.57, 6.06, 7.57).

The spatial resolution has subtle improvement represented by a slight reduction of the average of the main lobe in both directions. Additionally, we can see that among the adaptive BF, the $FWHM_{ax}$ and $FWHM_{lat}$ improvements are present but they are subtle.

The array noise suppression abilities provided by adaptive beamformer over DAS beamformer are clearly visible so that in displayed images, the CF-based adaptive methods appear to suppress more noise than their counterparts.

This behavior allows suppressing noise in both directions while preserving the main lobe. This behavior can be seen in displayed images in different methods for point targets. The CF, BY, MV-BY and the MV-WPF methods have the produced the point reflectors with an improved definition.

However, it is expected that the array noise suppression abilities occur while keeping the most relevant data preserved.

The CF-based beamformer show for point reflector show enhanced spatial resolution compared to MV and MV-BY by at the cost of the side lobe energy reduction. However, the WPF beamformer methods show more enhanced resolution mainly when imaging the isolated point reflectors, but the sidelobe reduction was not as much as in CF based beamformers.

Furthermore, the most improved lateral side lobe energy reduction was achieved by MV-BY in comparison with the different BF techniques.

4.4 RESULTS FOR PHANTOM DATA (PH2) AND 84-317

In order to examine the performance of the proposed BFs, the phantom data with circular anechoic cyst PH2 and the multiporpose phantom model and 84-317 were used.

4.4.1 RESULTS FOR PHANTOM DATA (PH2)

As illustrated in Fig 18 (b), a simulated phantom containing a total of 9 circular anechoic cysts was tested and the displayed images are shown in Fig. 26 show the beamformed images.

Values of CR, CNR were computed in accordance with the red boxes in Fig. 18 (e) and Fig. 18 (f) chosen to be the reference for respectively the intensity in the background and the cyst for intensity inside the cyst using the formulas Eq. (45) and Eq. (46). The beamformed images are displayed in Fig. 26 with a dynamic range of 60dB.

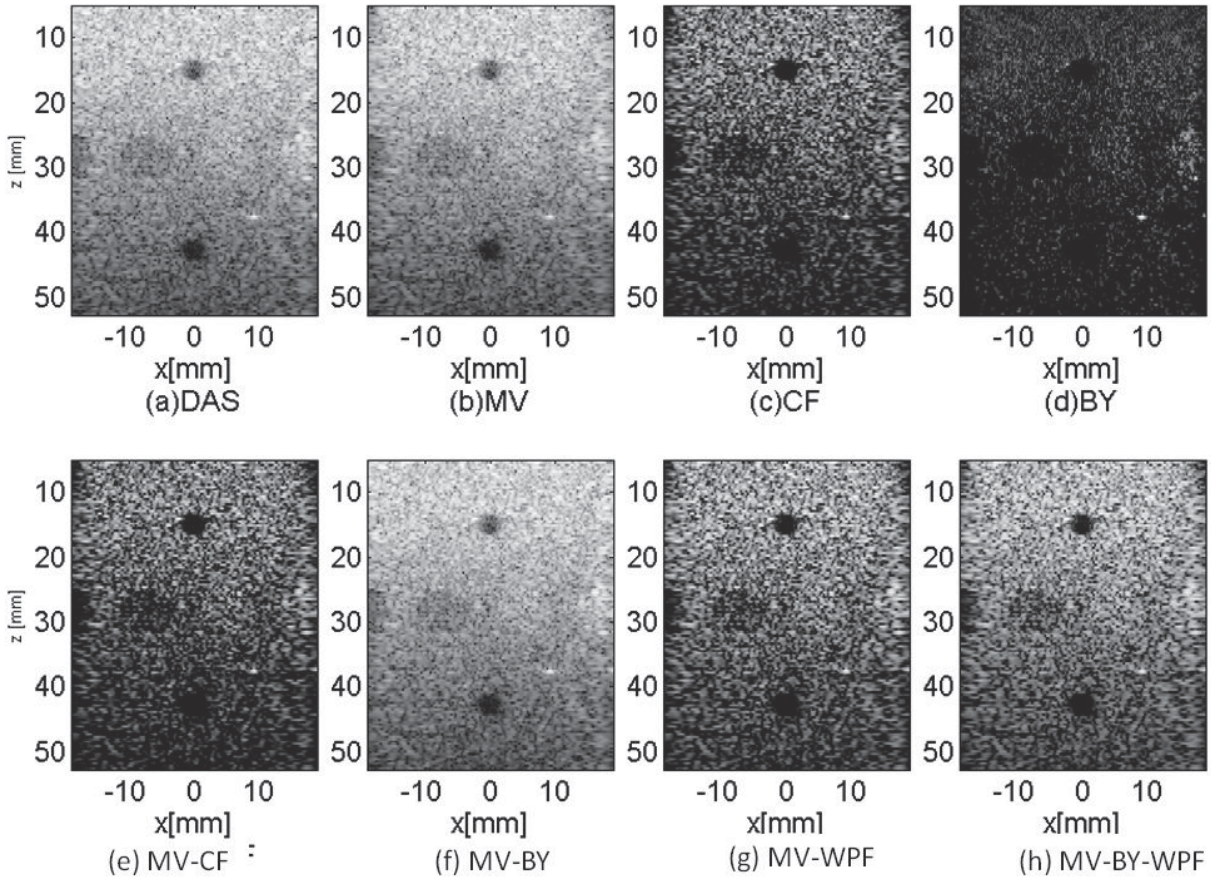

Figure 26: Beamformed images of anechoic cyst phantom data PH2 obtained by: (a)DAS, (b)MV, (c)CF, (d)BY, (e)MV-CF, (f)MV-WPF and, (g) MV-BY-WPF. All the images are displayed with a DR of 60 dB.

Table 8: Spatial resolution ($FWHM_{ax}$, $FWHM_{lat}$) for phantom data PH2

Beamformer	**CR** [dB]	**CNR** [dB]
DAS	20.03	2.21
MV	21.02	2.27
CF	23.13	2.35
BY	24.05	2.36
MV-CF	24.03	3.91
MV-BY	22.03	2.32
MV-WPF	24.14	2.79
MV-BY-WPF	25.48	2.88

On observing the displayed images, we can notice that the DAS exhibited a poor contrast among all the adaptive beamformers. The CF beamformer and the BY

exhibited more improved contrast compared to the MV and the MV-BY but the more improved contrast was showed by the MV-WPF which appeared to outperform slightly the BY beamformer.

However, MV-BY-WPF outperformed slightly the MV-BY which can be observed in the displayed images in Fig. 26. In order to quantify contrast performance, we used the CR and CNR as formulated in Eq. (45) and Eq. (46), respectively.

In accordance with Table 8, all the adaptive beamformers (with the sequence presented in Fig. 26 legend) outperformed the DAS beamformer in terms of CRCNR.

The results for PH2 in terms of CR/CNR were provided in terms of percentage using Eq. (50) provided the following results: (4.94, 15.47, 20.06, 19.97, 9.98, 20.51 and 27.20)/ (2.71, 6.33, 6.78, 27.14, 4.97, 26.24 and 30.31) respectively. We have noticed improvements introduced by MV-BY over MV in terms of CR/CNR in percentage were of 4.8/2.2 while for MV-BY-WPF over MV-WPF were of 5.6/3.2, respectively.

4.4.2 RESULTS FOR PHANTOM DATA ACQUIRED ON LABORATORY USING PHANTOM MODEL 84-317

We have examined phantom data (i.e., the anechoic cyst Fig. **??** (c)) collected on Verasonics Ultrasound Imaging System of UTFPR ultrasound laboratory with the following phantom models 84-317 and 040GSE, respectively. We only decided to display the images produced by DAS and the MV-BY-WPF to show improvements in terms of the quality of the displayed images using the proposed method for both phantoms.

Analogously to the phantom PH02, Table 9 presents results obtained using phantom 84-317 collected in US Lab. Using Eq. (50) to compute the CR/CNR in percentage. The collected data provided the following CR/CNR results (2.35, 3.48, 8.80, 10.26, 3.53, 13.33 and 17.66)/(5.57, 12.74, 16.33, 13.54, 4.78, 20.31 and 25.89), respectively. Improvements introduced by MV-BY over MV in terms of CR/CNR in percentage were of 1.15/3.77 while for MV-BY-WPF over MV-WPF were of 3.8/4.6, respectively.

Table 9: Contrast (CR, CNR) for phantom data acuired using phantom 84-317

Beamformer	**CR** [dB]	**CNR** [dB]
DAS	21.23	2.51
MV	21.33	2.55
CF	21.42	2.83
BY	23.1	2.92
MV-CF	23.41	2.85
MV-BY	21.58	2.63
MV-WPF	24.06	3.02
MV-BY-WPF	24.98	3.16

4.5 RESULTS FOR HUMAN *IN-VIVO* DATA (H1) AND (H2)

The human *in-vivo* data has been tested in order to evaluate the performance of our proposed beamformers. The displayed images in Fig. 28 and Fig. 27 show the beam responses produced by the proposed beamformers using human *in-vivo* data for both cases.

In accordance with Table 10 values of CR/CNR results for different beamformers are presented. The achived results in terms of CR/CNR for *in-vivo* showed values in percentage computed in accordance with Eq. (50).

For human *in-vivo* data H1, values of (2.29, 3.12, 5.20, 15.72, 4.58, 19.78 and 24.36)/(3.86, 6.76, 7.72, 13.04, 6.76, 10.62 and 14.97) were found while for H2 values of (2.47, 2.91, 9.34, 10.97, 5.24, 13.79 and 17.65)/(13.29, 13.87, 16.18, 16.18, 19.07, 23.69 and 31.79) were computed.

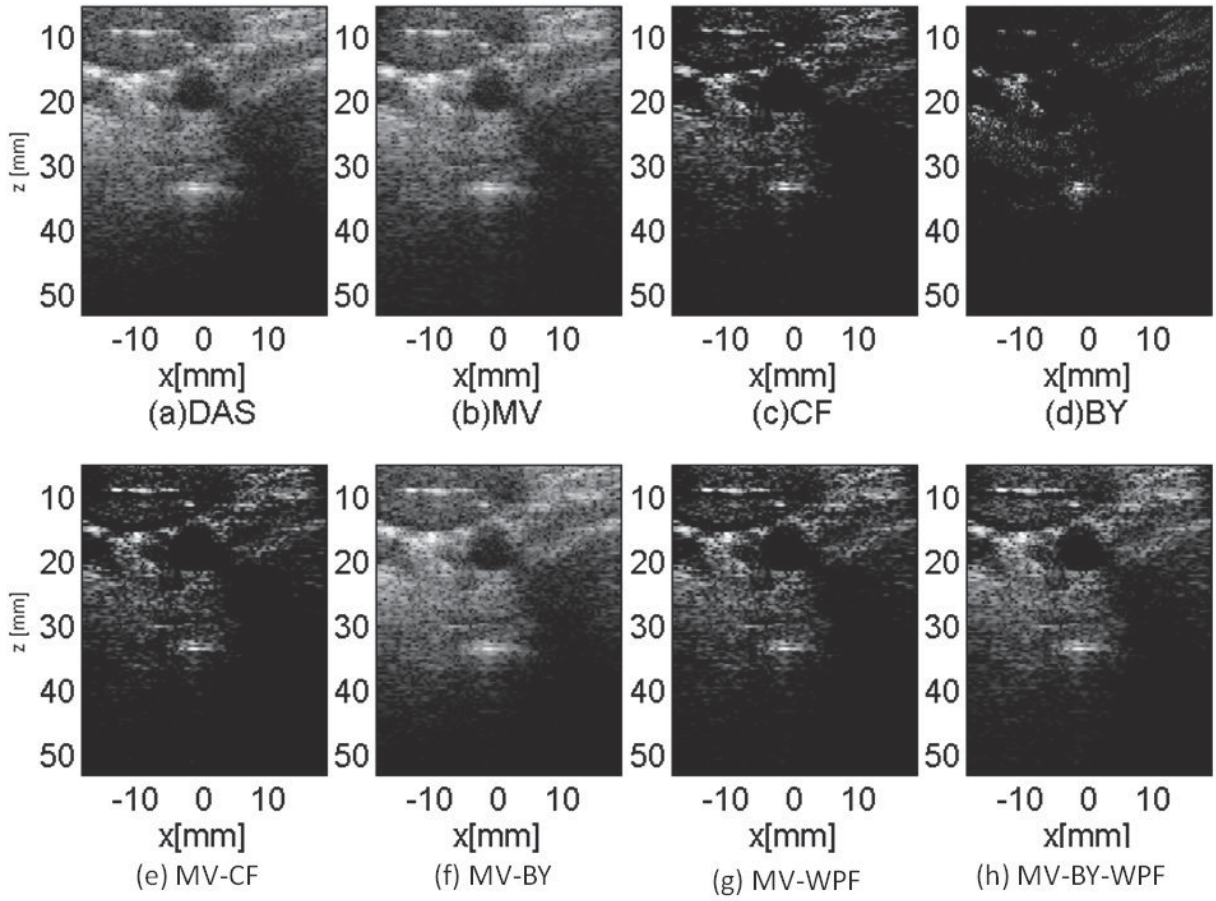

Figure 27: Beamformed images of human *in-vivo* cross sectional of a CA data H1 obtained by: (a)DAS, (b)MV, (c)CF, (d)BY, (e)MV-CF, (f)MV-WPF and, (g)MV-BY-WPF. All the images are displayed with a DR of 60 dB.

Improvements introduced by MV-BY over MV in terms of CR/CNR in percentage were of 2.23/2.79 for H1 and 2.70/5.10 for H2 whereas, improvements introduced by MV-BY-WPF over MV-WPF were respectively of 3.82/3.93 for H1, 3.38/6.54 for H2, respectively.

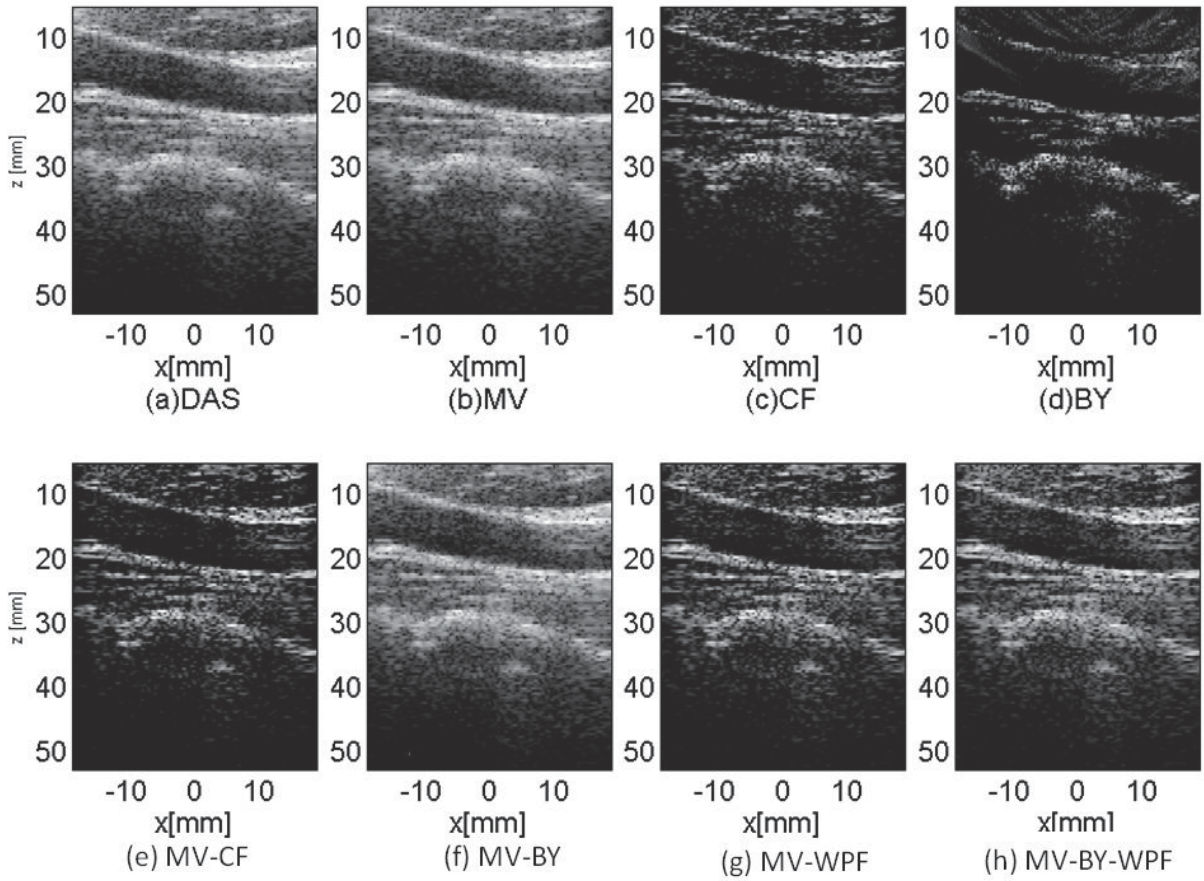

Figure 28: Beamformed images of human *in-vivo* longitudinal a CA data H2 obtained by: (a)DAS, (b)MV, (c)CF, (d) BY, (e)MV-CF, (f)MV-WPF and, (g)MV-BY-WPF. All the images are displayed with a DR of 60 dB.

Adaptive processing, mainly based on CF procedures and another post-filter method traditionally degrade the speckle background at the cost of increasing the imaging contrast. For a rigorous evaluation procedure, the speckle pattern produced by different beamformer methods should be taken into account.

In both cases (i.e., Fig. 27 and Fig. 28) we can observe that in the displayed images for different adaptive beamformers present improvements in terms of contrast however, some of them did not perform well in terms of image brightness preservation compared with the DAS beamformer.

In order to evaluate the speckle pattern of the proposed beamformers, all the beamformed data undergo the **ks** test/evaluation in order to evaluate if they follow the Rayleigh distribution.

In this study, we decided to select three cases in accordance with the plots of speckle pattern which is presented in Fig. 18 (a) for simulated contrast speckle

phantom data and Fig. 18 (e) and Fig. 18 (f) for experimental human *in-vivo* data for longitudinal CA and cross-sectional CA, respectively.

For CR and CNR evaluation Eq. (45) and Eq. (46) were used for phantom data while for speckle background evaluation, SNR is complemented by the Rayleigh pdf as presented in Fig. 30 (a), Fig. 30 (b) and Fig. 30 (c). The corresponding imaging regions for simulated and *in-vivo* data are respectively presented in Fig 18 and Fig. 29.

Table 10: Contrast (CR) and Contrast to noise ratio (CNR) for *in-vivo* data

Human *in-vivo* data	***in-vivo* data**			
	Cross CA		**Longitudinal CA**	
Beamformer	**CR [dB]**	**CNR [dB]**	**CR [dB]**	**CNR [dB]**
DAS	19.21	2.07	20.32	1.73
MV	19.55	2.15	20.42	1.96
CF	19.61	2.21	20.51	1.97
BY	20.21	2.23	22.11	2.01
MV-CF	22.23	2.34	22.44	2.01
MV-BY	19.79	2.21	21.01	2.11
MV-WPF	23.01	2.29	23.01	2.14
MV-BY-WPF	23,89	2,38	23,79	2,32

In order to demonstrate the benefits of our proposed method, all the images displayed in Fig 31, Fig.32, Fig.33, Fig.34 and, Fig.35 were compared at the following form: (a) represent the beamformed data for DAS beamforming for 75 acquisitions, (b) represent the beamformed data using DAS for 5 acquisitions while in (c) the MV-BY-WPF beamformer was performed with 5 acquisitions.

For speckle pattern evaluation, the imaging region has been selected in a different manner for all the beamformed images with 256x256 pixels. For simulated data we have considered all the selected backgrounds for each anechoic cyst while for human *in-vivo* data, the blue boxes the region outside the human *in-vivo* CA.

In Fig. 18 (a) all the imaging points were considered for spatial resolution evaluation (i.e., $FWHM_{ax}$ and $FWHM_{lat}$).

In Fig. 18 (b) the highlighted regions in circles have been used as the reference

for imaging contrast evaluation (i.e., CR and CNR) however, for speckle evaluation, the four highlighted regions with blue boxes have been considered for speckle pattern evaluation.

Each evaluation region has been subject to ks test (5% significance interval) to ensure that the envelope detected from beamformed data follows Rayleigh distribution. In Fig. 18 (c), the highlighted regions undergo the spatial resolution evaluation in order to test the performance of the proposed adaptive beamformers using $FWHM_{ax}$ and $FWHM_{lat}$.

The corresponding results are presented in Table 7. In Fig. 18 (d), the highlighted regions undergo contrast evaluation in order to test the performance of the proposed adaptive beamformers using CR and CNR.

The corresponding results are presented in Table **??**. Results of CR/CNR for phantom data (i.e., the phantom PH2) can be obtained at the top of Table 8 while for human *in-vivo* data (i.e., the Longitudinal CA and the Cross-sectional CA) the CR/CNR results can be seen further down Table 10.

Either in Fig. 18 (e) and Fig. 18 (f) or in Fig. 29 (b) and Fig. 29 (c), the human *in-vivo* data are presented and, the highlighted regions are used to compute the imaging contrast. Additionally, the regions highlighted out the borders of the Carotid artery only one is used for imaging contrast evaluation but all of them are used as the references for speckle pattern evaluation.

Each evaluation region has been subject to **ks** test (5% significance interval) to ensure that the envelope detected from beamformed data follows the Rayleigh distribution. The corresponding results for contrast can be found in Table 10. Results of speckle-pattern evaluation are well presented in Fig. 30 and their corresponding SNR values to each beamformer are also included in Fig. 30 legend.

From Table 12 we can see values of CR/CNR using different PWE for different adaptive beamformers. We have noticed that the MV-BY-WPF produced CR/CNR of 36.62/4.57 which was almost of that provided by DAS with 75 PWE, i.e., 37.45/4.76. In such a context, the selected contrast values were compared to that produced by DAS with 75 PWE as presented in Table 12.

Table 11: CR and CNR for different Plane Wave Emissions (PWE) using S2

PWE	1	3	5	7	11	17	21
Beamformer				CR[dB]			
DAS	17.02	19.21	20.02	21.24	22.43	23.21	23.86
MV	20.38	20.05	24.12	22.27	23.13	23.41	24.05
CF	23.98	21.32	33.01	23.91	23.95	24.01	25.80
BY	23.98	25.72	40.024	24.11	24.22	25.01	25.95
MV-CF	21.59	23.42	36.15	23.90	25.53	25.91	26.12
MV-BY	21.55	24.75	26.02	27.01	29.03	29.96	31.56
MV-WPF	23.68	26.42	35.86	35.91	36.03	37.12	38.02
MV-BY-WPF	24.98	28.67	36.62	37.21	36.27	37.76	38.46
				CNR[dB]			
DAS	1.64	2.45	3.12	3.44	4.23	4.31	5.02
MV	2 1.84	2.48	3.92	3.47	4.36	4.86	5.12
CF	2.01	2.55	3.61	3.93	4.45	4.93	5.56
BY	2.31	2.71	3.94	3.24	4.23	5.02	5.62
MV-CF	2.02	2.68	3.94	3.73	4.33	5.16	5.75
MV-BY	2.03	2.73	3.75	3.80	4.33	5.24	5.82
MV-WPF	2.11	3.32	4.53	3.38	4.75	5.03	6.24
MV-BY-WPF	2.31	3.57	4.57	4.61	4.83	5.27	6.48

Table 12: The CR and CNR for DAS beamformer 75, DAS beamformer 5 and MV-BY beamformer 5 for phantom and *in-vivo* data

Phantom/*in-vivo*	**Phantom dataset**				***in-vivo* dataset**			
	040GSE		**84-317**		**Cross CA**		**Longitudinal CA**	
Beamformer	**CR [dB]**	**CNR [dB]**	**CR [dB]**	**CNR [dB]**	**CR [dB]**	**CNR [dB]**	**CR [dB]**	**CNR [dB]**
DAS, 75	26.3	2.19	23.3	2.57	24.2	2.43	24.1	2.37
DAS, 5	20	2.21	21.2	2.51	19.21	2.07	20.32	1.73
MV-BY-WPF, 5	25.5	2.88	25.0	3.16	23.89	2.38	23.79	2.32

4.6 SPECKLE STATISTICS

We evaluated the speckle pattern produced by different beamformers. All the proposed beamformers undergo the **ks** test with 5% significance to ensure if they follow the Raleigh distribution. In this study, we decided to select three cases for evaluation which include the simulated data S2 and human *in-vivo* data H1 and H2, respectively.

4.6.1 SPECKLE STATISTICS FOR S2

Traditional CF based beam-formers and Wiener post-filter based beamformers traditionally provide increased spatial resolution at the cost of reduced speckle-pattern while increasing the imaging contrast.

On observing the beamformed images using adaptive processing in Fig. 8, CF, BY, MV-CF and the MV-WPF show an improved image contrast. The CF, MV-CF and MV-WPF, in spite of apparently degraded speckle background, the imaging contrast has increased significantly. Figure 30 (a) present plots of speckle pattern of simulated phantom data.

For speckle pattern evaluation, the TRD has fit to DAS beamformer as the reference, due to the fact that it follows strictly the Rayleigh distribution. In terms of RD, the MV beamformer showed values closer to that presented by DAS beamformer, which agrees with a closer SNR as can be seen in Fig. 30 (a) or Table 13. In BY method, the displayed image darkened as can be seen in Fig. 23 (d) and, is in agreement with the low SNR value exhibited in Table 13. The MV, MV-CF and MV-BY better preserved speckle which is complemented by an increased SNR value as presented Table 13. The RD curves are also closer one another and are in agreement with the corresponding SNR values.

Figure 29 represents the scanning regions (highlighted) used for speckle pattern evaluation using different beamformers. In Fig. 29 (a), the upper left-most scanning regions was adopted to generate the Rayleigh pdf curves as presented in Fig. 30 (a).

Additionally, results of speckle statistics were computed taking as reference Fig. 18 (b) blue box their results are presented in Fig. 30 (a) and also complemented by the SNR in Table 13. While performing the hypothesis tests we have noticed different results for each beamformer.

The test results are highlighted as **PASS** (i.e., one (1)) or **FAIL** (i.e., (0)). The hypothesis test results show which of the selected scanning regions of a beamformed image their speckle pattern followed the Rayleigh distribution.

4.6.2 SPECKLE STATISTICS FOR H1 AND H2

In order to evaluate the quality of the speckle pattern produced by different adaptive beamformers the **ks** text has been performed in all the selected imaging regions in accordance with, Fig. 23 (b), Fig. 18 (e) and, Fig. 18 (f) respectively. For simplicity, the H1 and H2 scanning regions for *in-vivo* data are shown in Fig. 29 (b) and Fig. 29 (c), respectively.

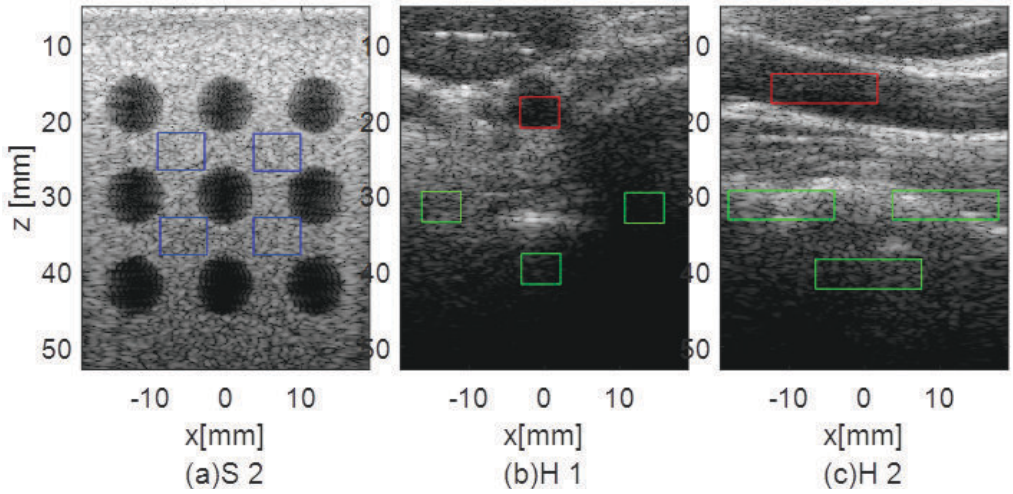

Figure 29: The scanning regions (highlighted) used for speckle pattern evaluation. (a), (b) and (c), respectively.

Similarly to the simulated data, for both cases (i.e., H1 and H2) the results of beamformed images using *in-vivo* data show that CF based beamformers showed reduced amplitude in their backgrounds including in that regions selected for speckle pattern evaluation. In this context, the reduction in amplitude background imply on speckle pattern degradation but the imaging contrast has increased significantly as presented in Table 10. Notice that the imaging contrast increases at the cost of suppressing some imaging details which lead to a poor image quality despite enhancing the visibility of image borders.

Figure 30 (b) and 30 (c) present plots of speckle pattern of experimental *in-vivo* data. Similarly to the simulated data using Fig. 30 (a), the speckle pattern has been evaluated taking as reference the TRD which is fit to DAS beamformer due to the fact

that the corresponding histogram intensities of envelope-detected data follow closely the Rayleigh distribution.

Table 13 show the speckle assessment of different beamformers. The plots of the RD in Fig. 30 is also complemented by the SNR results shown within the legend of Fig. 30 for S2, H1 and H2 data.

The RD for MV and MV-BY beamformer showed values closer to that presented by DAS beamformer and agrees with the SNR values presented in Table 13 as well as in Figs. 30 (b) and (c) legends. In BY method for both cases (i.e., H1 and H2), the image darkened as can be seen in Fig. 8 (d), Fig. 27 (d) and, Fig. 28 (d) respectively, implying in an agreement with the low SNR value exhibited within the legend as well as in Table 13.

Table 13: The SNR for different beamformer using S2, H1 and H2 dataset

Beamformer	S2	H1	H2
DAS	1.75	1.66	1.64
MV	1.69	1.57	1.57
CF	1.61	1.59	1.56
BY	**0.94**	**0.86**	**0.86**
MV-CF	1.57	1.49	1.42
MV-BY	1.69	1.57	1.57
MV-WPF	1.33	1.21	1.14
MV-BY-WPF	1.44	1.31	1.25

In Figs. 28 (b),(f) and 28 (b),(f) for respectively MV, and MV-BY beamformers better preserved the speckle which is complemented by an increased SNR value presented in Figs. 30 (a), (b) and (c), respectively.

Figure 29 represents the scanning regions (highlighted) used for speckle pattern evaluation using different beamformers. In Fig. 29 (b)-(c), all the upper left-most scanning regions were used to generate the Rayleigh pdf curves as presented in Fig. 30 (b)-(c).

The results of speckle statistics were computed taking as reference Fig. 29 (b) and Fig. 29 (c) red boxes for both cases and their results are presented in Fig. 30 (b) and Fig. 30 (c) and also complemented by the SNR values. Similarly to the simulated

data, while performing the hypothesis tests we have noticed different results for each beamformer.

Similarly to the simulated data we highlighted the **ks** test results as **PASS** (i.e., one (1)) or **FAIL** (i.e., (0)) in order to evaluate which of selected scanning regions of a beamformed images their speckle pattern followed the Rayleigh distribution.

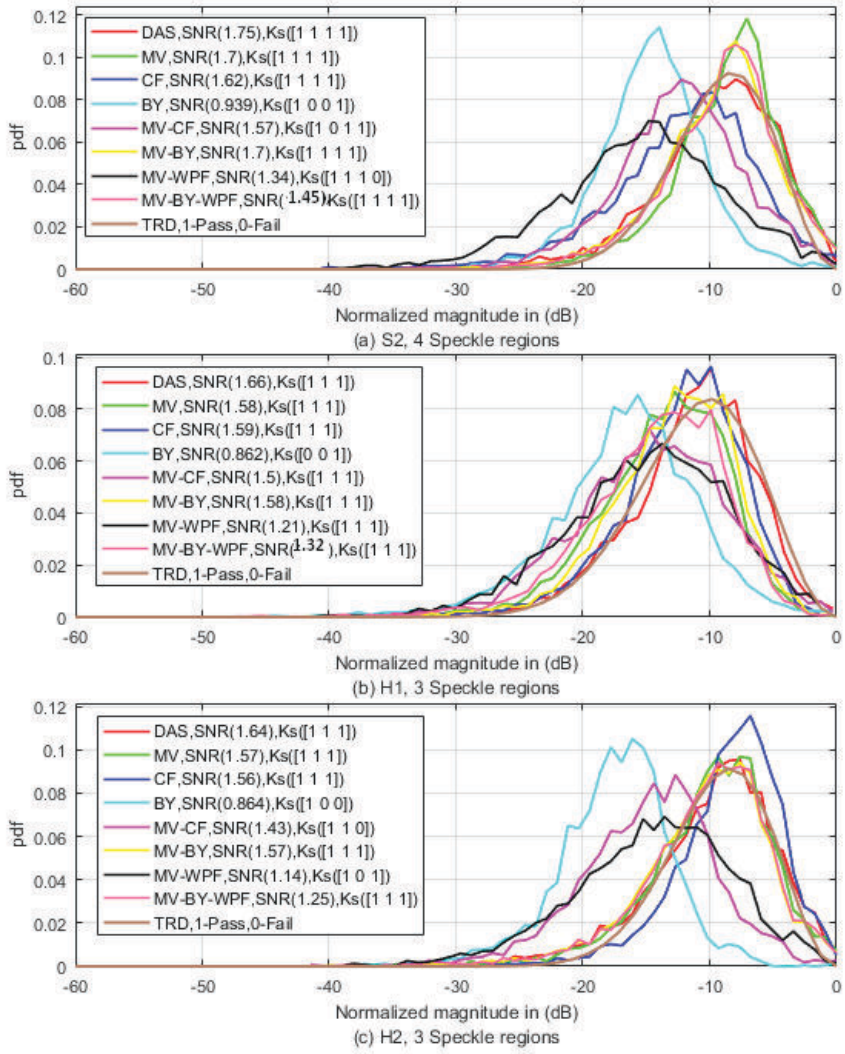

Figure 30: Images of simulated data and human *in-vivo* data for cross-sectional H1 and longitudinal H2 CA: (a) Represents the evaluation results of the first speckle region (i.e., the leftmost) of S2, (b) represents the evaluation results of the first speckle region (i.e., the leftmost) of H1 and (c) represents the evaluation results of the first speckle region (i.e., the leftmost) of H2, respectively.

The SNR produced by different adaptive beamformers is presented in Fig. 30 and also complemented by Table 14 which presents the results of speckle produced by different adaptive beamformers in percentage (%) taking DAS as the reference. The

results were computed using Eq. (51).

$$\Delta_{SNR(\%)} = \frac{SNR}{SNR_{ref}} 100 \tag{51}$$

where ref stands for $reference$, and $\Delta_{SNR(\%)}$ represents SNR in percentage taking DAS as reference.

Table 14: Speckle pattern produced by different adaptive beamformers taking DAS as reference

Beamformer	S2	H1	H2
MV	97.14	95.18	95.73
CF	92.57	95.78	95.12
BY	**53.71**	**51.80**	**52.43**
MV-CF	89.71	90.36	87.19
MV-BY	97.14	95.18	95.73
MV-WPF	76.57	72.89	69.51
MV-BY-WPF	76.57	72.89	76.21

Table 15 was obtained from Fig. 30 in terms of representation of the peaks of Rayleigh distribution and Normalized intensity in dB. This Table is complementary in terms of the peaks of Normalized intensity in dB produced by different beamformers.

At one hand, we notice that the BY method degraded significantly the image brightness by presenting the Normalized intensity in dB with lower values at the other hand, the MV-BY-WPF exhibited values closer compared with that obtained by DAS which is in agrees either in terms of the displayed images, RD curves and the SNR values presented in Table 13.

Table 15: The peaks of Rayleigh pdf and Normalized intensity in dB for differente beamformers.

Beamformer	S2, [dB]	H1, [dB]	H2, [dB]
DAS	-8.0	-10.0	-7.2
MV	-7.8	-12.5	-7.0
CF	-11.0	-10.0	-7.1
BY	**-14.0**	**-16.0**	**-16.4**
MV-CF	-7.9	-12.5	-12.1
MV-BY	-8.1	-13.1	-8.0
MV-WPF	-15.0	-13.0	-13.2
MV-BY-WPF	-8.2	-10.0	-7.0

4.6.3 QUALITATIVE EVALUATION USING DISPLAYED IMAGES: DATA FROM PICMUS PLATFORM

In order to highlight the improvements introduced by MV-BY-WPF among the basic results obtained from PICMUS dataset we have displayed the beamformed images using the standard DAS, 75 followed by DAS, 5 and the MV-BY-WPF, 5.

The last comparison was suggested in such a manner to show qualitatively the abilities of our proposed methodology in terms of array noise suppression which results in a high image quality.

Regarding the amount (i.e., at about the average) of the plane wave firing elements involved in comparison was performed to show how much number of transmission we could reduce while attaining the image quality comparable to that obtained with a larger number of plane wave transmission.

The corresponding images were displayed in Fig. 31 for simulated anechoic cyst phantom: (a) DAS, 75 plane waves, (b) DAS, 5 plane waves and (c) MV-BY-WPF, 5.

Likewise, Fig. 32, Fig. 33, Fig. 34 and Fig. 35 present the displayed images of the phantom data PH1, the phantom data PH2, the *in-vivo* human data H1 of longitudinal CA and, the *in-vivo* human data H2 of cross-sectional CA, respectively.

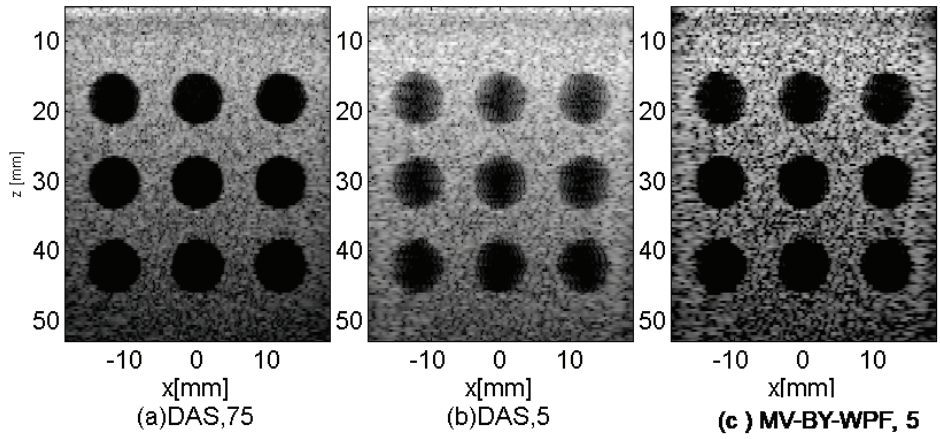

Figure 31: Images of simulated anechoic cyst phantom: (a) DAS, 75, (b) DAS, 5 and (c) MV-BY-WPF, 5, respectively.

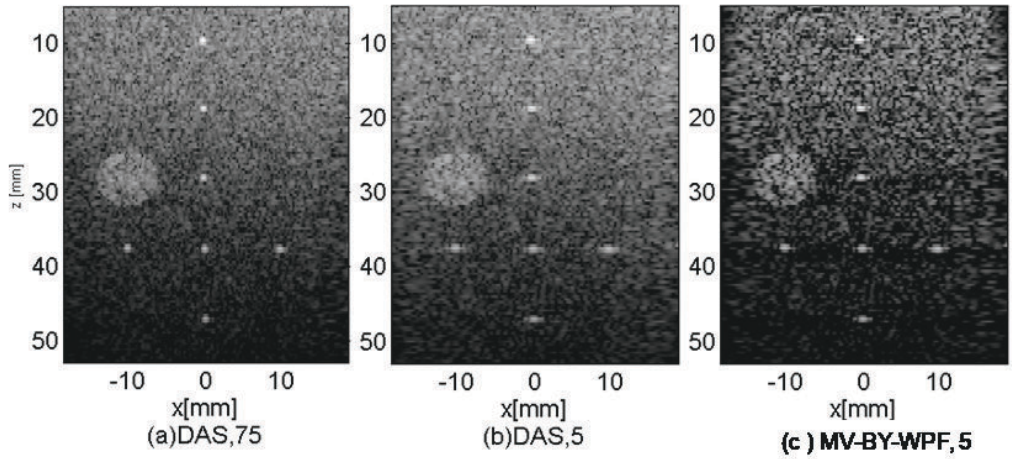

Figure 32: Displayed images of phantom data PH1: (a) DAS, 75, (b) DAS, 5 and (c) MV-BY-WPF, 5, respectively.

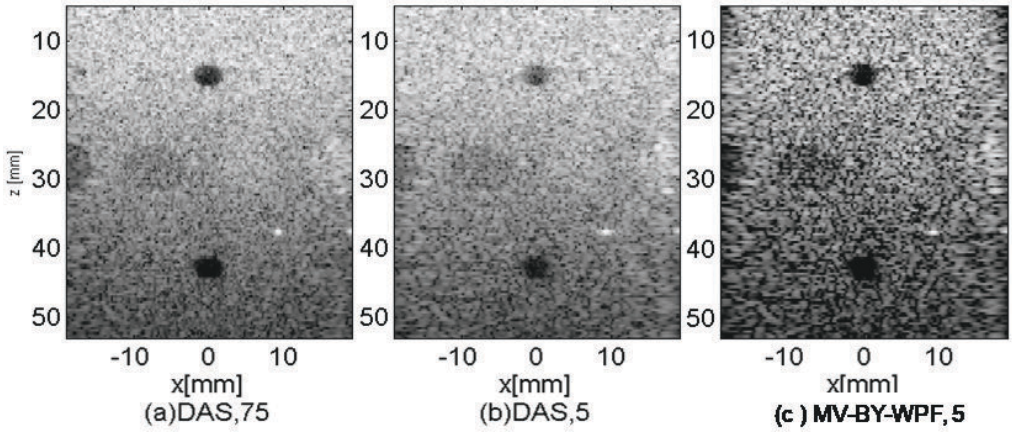

Figure 33: Images of phantom data PH2: (a) DAS, 75, (b) DAS, 5 and (c) MV-BY-WPF, 5, respectively.

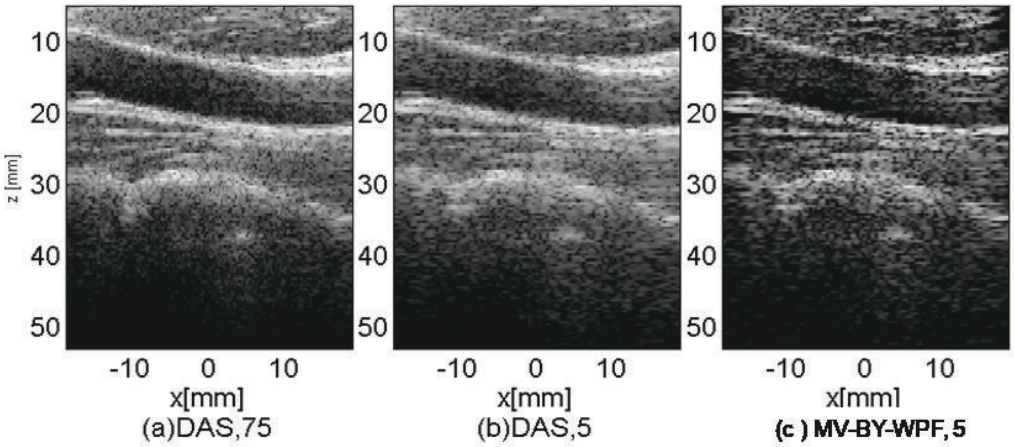

Figure 34: Images of human *in-vivo* human data H1 of longitudinal CA: (a) DAS, 75, (b) DAS, 5 and (c) MV-BY-WPF, 5, respectively.

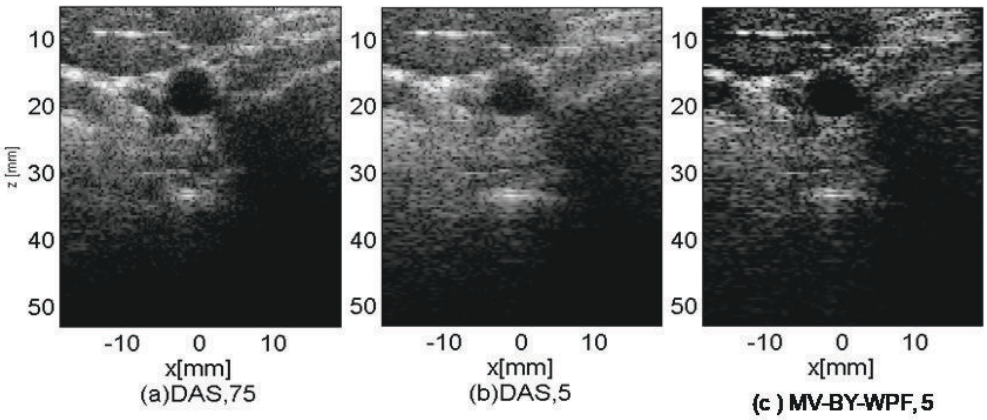

Figure 35: Images of human *in-vivo* data H2 of cross-sectional CA: (a) DAS, 75, (b) DAS, 5 and (c) MV-BY-WPF, 5, respectively.

4.6.4 QUALITATIVE EVALUATION USING DISPLAYED IMAGES: DATASET COLLECTED ON US LABORATORY.

In Fig. 36, the top row presents images acquired from Verasonics Imaging System for 75 plane wave emissions and beamformed with DAS: (a) simulation data from SIMU, (b) Hypo-echoic target from 84-314, (c) Anechoic cyst from 84-314, (d) and (e) phantom data from 040GSE, respectively, while the midle row presents images acquired from Verasonics Imaging System for only 5 plane wave emissions and beamformed with DAS with the abovementioned sequence. Analogously, the last row presents images acquired from Verasonics Imaging System for 5 plane wave emissions and beamformed with MV-BY-WPF following the the abovementioned sequence.

We can notice that the image quality produced by our proposed method with 5 plane wave emissions is comparable to the quality of DAS with 75 plane wave emissions. Rather than synthesizing an amount of 75 plane wave emissions we need only 5 plane wave emissions to produce an equivalent image quality.

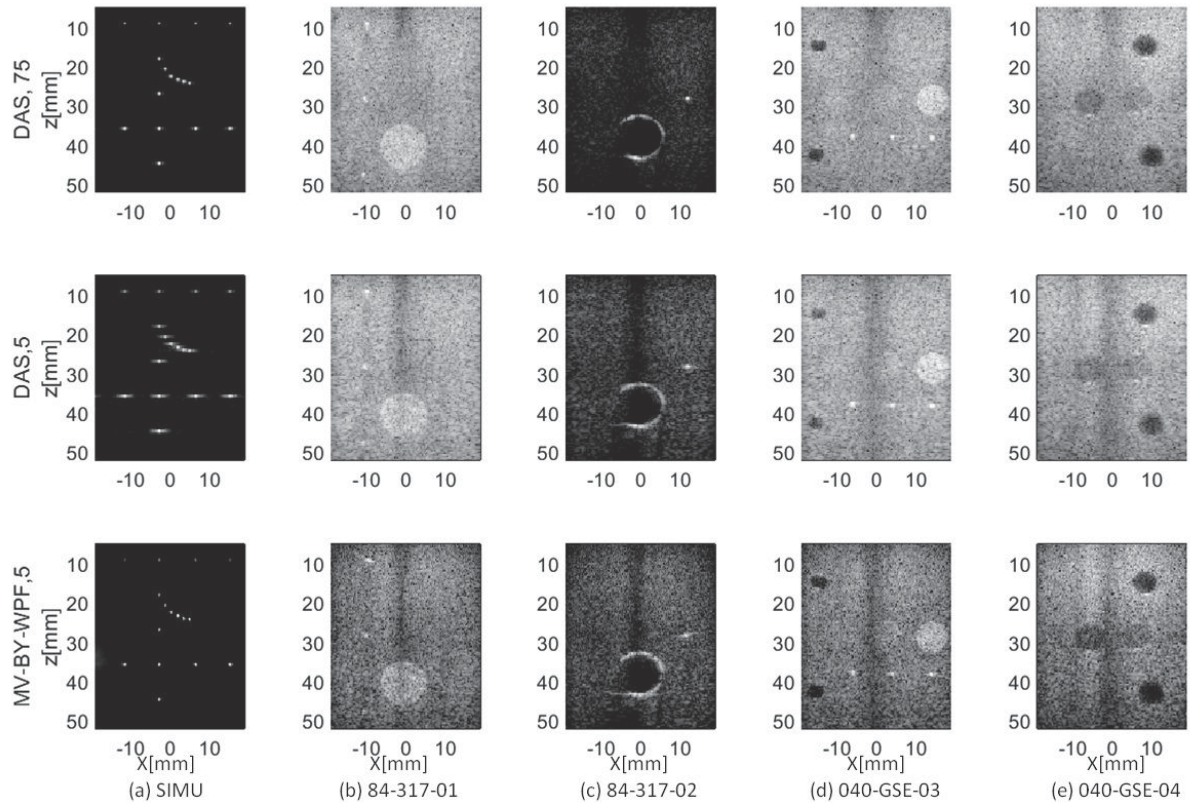

Figure 36: The top row presents images acquired from Verasonics Imaging System for 75 plane wave emissions and beamformed with DAS: (a) simulation data from SIMU, (b) Hypo-echoic target from 84-314, (c) Anechoic cyst from 84-314, (d) and (e) phantom data from 040GSE, respectively, while the midle row presents images acquired from Verasonics Imaging System for only 5 plane wave emissions and beamformed with DAS with the abovementioned sequence. Analogously, the last row presents images acquired from Verasonics Imaging System for 5 plane wave emissions and beamformed with MV-BY-WPF following the the abovementioned sequence.

5 DISCUSSION

We have implemented the MV-BY beamformer to US imaging. The MV-BY beamformer represents a combination between the MV beamformer with the*a posteriori* pdf coefficients. The MV-BY outperforms the MV in terms of spatial resolution and contrast.

We have combined the MV-BY with the WPF beamformer in order to obtain a more robust WPF. As result, we have noticed improvements introduced in image quality mainly in terms of contrast while retaining the speckle pattern. In terms of imaging resolution, improvements were subtle.

The Bayesian-based post-filter (i.e., the pdf coefficients) which was combined with the MV beamformer resulted in MV-BY which was used as input or desired signal in the WPF. As result, the MV-BY-WPF was formulated based on MV-BY. Regarding the MV-BY beamformer is formulated combining the *a posteriori* pdf coefficients with the MV beamformer.

We have noticed that the *a posteriori* pdf coefficients have the ability to improve the signal coherence which is one of the problems of traditional adaptive beamformers.

In accordance with the obtained results, we see that the statistics of image intensity distribution along the imaging region appeared to be altered which we believe is due to the signal coherence added by applying this factor (i.e., the pdf coefficients).

Different works published in the literature present and discuss improvements introduced by the MV based beamformers and other adaptive methods.

In Qi et al. (2018) a joint transmit-receive beamformer was designed for the plane wave in the US and outperforms different MV approaches. However, this was accomplished at high computational complexity despite benefits in terms of resolution and contrast were limited.

In Polichetti et al. (2018) a nonlinear beamformer is proposed in order to improve the performance of traditional Delay Multiply and Sum (DMAS) method for the plane wave the US, however, to attain the performance provided by the DAS 75, an amount of 11 emissions was required in spite of less preservation of the image

brightness.

In Ozkan et al. (2018) a beamformer using MAP approach was implemented whose background was supported on the basis of the inverse problem involving a signal mode accounting for the white noise assumption. The obtained results for contrast and resolution were satisfactory but, the beamformer need be highly iterated in order to achieve an optimal to obtain a high-quality image.

An interesting publication by Chernyakova et al. (2018) has been suggested for US imaging in CPWC. In this work, a comparison with different CF based methods is performed with special emphasis to the amount of plane wave emissions which should be reduced in order to reconstruct an image with the quality equivalent of that obtained with a total amount (i.e., of 75) of plane wave sequences provided in the PICMUS website.

In their work, could successfully represent an image quality of 75 plane wave emission with only 13 plane wave emissions using their proposed method termed as (Iterative) Maximum a posteriori (iMAP) beamformer (CHERNYAKOVA et al., 2018).

In our proposed method, using the PICMUS data, with an amount of 5 plane wave emissions with MV-BY-WPF we have reconstructed an image with quality in terms of contrast and speckle pattern comparable to that obtained when using a total amount of 75 plane wave emissions at computational complexity similar to that provided by the MV beamformer without degrading the spatial resolution.

We have summarized the outcomes of this our in terms of spatial resolution, contrast, Speckle statistics and, the Computational complexity evaluation.

5.1 SPATIAL RESOLUTION

In terms of resolution, all the adaptive beamformers presented improvements compared to DAS. The results in terms of beamformed images are presented in Fig. 21 complemented by lateral profiles of the PSF of different point reflectors at different imaging depths.

In Fig. 21 we can notice that the MV beamformer has a narrower main lobe and lower side lobe levels meaning that it was superior to DAS in resolving the simulated point reflectors.

We notice that the $FWHM_{ax}$ and $FWHM_{lat}$ from Table 5 show that BY, MV-CF

and MV-BY were superior to MV beamformer by providing a narrower $FWHM_{ax}$ and $FWHM_{lat}$.

We believe that the improvements of BY over MV are due to signal coherence introduced by the *a posterior* pdf (i.e., the pdf coefficients). However in terms of MV-CF improvements were introduced due to the effects of CF which acts as weighting factor to improve the local intensity, while the improvements of the MV-BY are due to the signal coherence introduced by the *a posterior* pdf over the MV beamformer.

Improvements of WPF over MV are explained in terms of the MV-WPF implementation using the MV principle which represents an MMSE of the desired signal.

This ability allows WPF preserving the abilities of MV which is a distortionless beamformer by keeping the main lobe unchanged at broadside while suppressing noise and interferences at other directions. However, the improvements of MV-BY-WPF over MV-WPF can be seen as a different behavior of WPF when the desired signal is of different statistics.

In such a context, we associate such improvements to the robustness of the MV-BY over different SNR scenarios. The MV-BY is used as the desired signal in WPF design. In general, improvements in terms of the spatial resolution were subtle.

However, CF, MV-CF, and MV-WPF appear to present the most resolved scatterers compared to the MV beamformers. Such improvements in spatial resolution are complemented by the lateral profiles depicted in Fig. 22.

In Fig. 22 we can notice that the improvements are complemented by enhancing the ability to suppress sidelobe energy in the imaging background.

In terms of sidelobe energy, we can see that the lateral profiles presented by the MV-WPF and MV-BY-WPF were somewhat similar but the former appears to be more effective in terms of sidelobe suppression abilities than the letter.

It can be seen in the displayed images, the lateral profiles and the Tables 5 and 7 that the MV-WPF and MV-BY-WPF beamformer were almost similar, but the lateral profiles of the former together with the displayed images show that the brightness in the image background appearers to be highly reduced.

Similarly to the simulated data, Fig. 7 presents the displayed images of phantom experiments data PH1 for spatial resolution evaluation. No lateral profiles

were provided, but the array noise abilities presented by the proposed beamformers in the simulation scenario were maintained in accordance with the displayed images.

In general, the performance of the proposed beamformer was in agreement with that obtained in simulation data. Regarding adaptive beamformers, we believe that improvements of MV-BY over MV in terms of the spatial resolution were due to the enhanced signal coherence introduce by the *a posterior* pdf which is comparable with a post-filter combined with the MV beamformer.

5.2 CR AND CNR

In terms of CR and CNR, all the adaptive beamformers presented improvements in imaging performance compared to DAS. The displayed images Fig. 23, Fig. 26, Fig. 28 and Fig. 27 show improvement introduced by adaptive beamformer over the DAS beamformer.

Particular to Fig. 23, the lateral profiles Fig. 24 of different beamformers were depicted in order to complement the results provided by the displayed images in Fig. 23. We believe that these results apply to different scenarios of CR and CNR in this study. We have computed CR and CNR using formulas Eq. (45) and Eq. (46), respectively.

The computed values od CR and CNR are presented in Table 6 for simulated data and Table 8 for human *in-vivo* data.

In Table 10 for different scenarios. Improvements of MV-BY over MV were due to the signal coherence introduced by the posterior pdf coefficients. In this context, the *a posterior* pdf coefficients are applied to the MV beamformer and improve the signal coherence.

The MV-WPF has improved the CR and CNR of MV as expected from simulated results where the MV-WPF is seen as providing solution approaching the MMSE (NILSEN; HOLM, 2010). The WPF for adaptive processing using the MV beamformer (i.e., MV principle) does not affect the signal amplitude power while minimizing the noise power (NILSEN; HOLM, 2010).

However, the MV-BY-WPF provides more improved contrast by taking into consideration the desired signal obtained from a most robust beamformer (i.e., the MV-BY beamformer).

While the simulated data for point reflectors provided improvements in terms of spatial resolution using BY method, the contrast by BY beamformer also improved significantly but, predominantly the signal intensity in the imaging background was reduced meaning that an apparent suppression of image details has occurred. It can be interpreted to as resulted in speckle pattern severely degraded which will be analyzed next subsection.

5.3 SPECKLE STATISTICS

The speckle pattern produced by different beamformers was assessed in terms of signal to noise ratio (SNR) and the Raleigh probability density function analysis (HVERVEN et al., 2017) of the beamformed data.

The SNR values and the Rayleigh probability function of envelope-detected data were respectively computed using the formulas Eq. (47) and Eq. (48), respectively. All the adaptive beamformers which presented more improvements in imaging resolution and contrast presented the much more speckle reduction by taking DAS beamformer as the reference.

This behavior can be observed from the displayed images or in the computed SNR values. We can see that the MV beamformer compared to DAS produced a slightly reduced SNR which leads to the speckle reduction and also can be complemented by the displayed images.

In order to deepen the speckle assessment in the highlighted regions (i.e., the blue and red boxes) of Fig. 18 (b), Fig. 18 (e) and Fig. 18 (f) we have displayed the speckle assessment Fig. 30 (a), Fig. 30 (b) and Fig. 30 (c) produced by different beamformers in terms of their intensity histogram in accordance with the Rayleigh probability density function.

In Fig. 30 we decided to show the SNR values particular to specific beamformer and the corresponding result of **ks** test. The k-test with 5% significance was performed to ensure if a specific imaging region of a beamformer output follows the Rayleigh distribution.

For simplicity, we have labeled each test corresponding to specific imaging Region as PASS (i.e., (1)) or FAIL (i.e., (0)), respectively. From Fig. 30 (a), 30 (b), and 30 (c) we notice that the MV, MV-BY and sometimes MV-CF better preserved

the speckle and were closer each other. The MV-BY-WPF preserved better speckle compared to MV-WPF. These results can be explained following the computed values of SNR for each beamformer.

Regarding to **ks** test, different adaptive beamformers showed their selected regions for **ks** test following the RD with **PASS** however, as can be seen in Fig. 30 (a), 30 (b) , and 30 (c) some imaging regions had severe speckle degradation from adaptive processing and did not retain the speckle pattern at acceptable limits in terms of allowed statistics despite they exhibited more improved spatial resolution they **FAILED** the **ks** text evaluation.

5.4 COMPUTATIONAL COMPLEXITY EVALUATION

On evaluating the computational complexity in CPWC imaging the number of plane wave firing elements (i.e., $N = 5$) must be taken into account. The main goal of CPWC is reducing the Computational Complexity (CC) aiming to increase the frame rate of the imaging system that is the reason why the analysis of the CC plays an important role.

The require CC by uniformly weighted DAS beamformer is of an order of $O(M)$ where M is the array length set to be 128 hence, it will take $O(NM)$ floating operations. However, in adaptive beamforming, the CC occurs in the inversion operation of the CM.

In MV beamformer, the CM inversion require $2/3L^3$ Floating Operations (FO) when applying Gauss-Jordan eliminations (ZHAO et al., 2015; ZENG et al., 2013).

In addition, for adaptive processing, we used a subarray of 30% of the full array size (i.e., $L = 0.3x128 = 38$) elements and therefore, the MV will need $O(N(2/3L^3))$ FO.

The WPF formulation is similar to CF by applying the coherent sum and incoherent sum components in order to compute the focusing indices.

In terms of WPF, the coherent sum and incoherent sum components are expressed in terms of output power of desired signal and noise plus interference power as presented in Eq. (24) or Eq. (25). While computing the WPF it's expected to consume a similar amount of time. For computing the WPF the time consuming required is as similar as that required to compute the CF.

For CF computation in Eq. (22) an additional computational load lead to the computation of the coherent and incoherent energy of L^2 which is neglected (ZHAO et

al., 2016).

In this work, the computation of CM in Eq. (20) and the NPICM CM in Eq. (29) undergo the spatial smoothing and temporal averaging effects that have subtle impact in the CC (BUSKENES et al., 2017, 2015; ZHAO et al., 2016).

According to Bell et al., (BELL et al., 2000) the MV-BY will need an amount of FO almost that is required for MV weight computation for weight vector update. That is because it uses the already computed inverted covariance matrix used for MV weight (BELL et al., 2000).

As mentioned by Bell et al., the additional time needed to compute the *a posteriori* pdf will be neglected. In such context, the MV-BY and MV should present similar computational complexity of $O(N(2/3L^3))$ FO.

In total the time consumption by WPF is about $O(N(2/3L^3) + L^2))$ which is almost $O(N(2/3L^3))$(ZHAO et al., 2016). It means that similarly to the MV beamformer the most computationally demanding step for MV-WPF and MV-BY-WPF is still the CM inversion among different steps in adaptive processing.

In general, all the adaptive beamformers are computationally intense compared to DAS and prohibitive for real-time implementation. However, for real-time application the complexity can be decreased by applying the recursive updating Mehdizadeh et al. (2012) combined with the Graphics Unit Processing (GPU) (ZHAO et al., 2015).

In general, we can conclude that the improvements in terms of image quality were obtained at an extra CC compared to DAS, but at CC similar to that of MV beamformer.

6 CONCLUSIONS AND REMARKS

6.1 CONCLUSIONS

We have successfully proposed and implemented the Bayesian-based beamformer (MV-BY) with the Wiener post-filter (WPF) based (i.e., MV-BY-WPF) for adaptive beamforming of ultrasound image using coherent plane wave compounding (CPWC).

The CPWC imaging is low SNR due to the lack of focusing on pulse emission. Different adaptive methods such CF based beamformer or Wiener post-filter beamformer have been suggested to overcome such limitation however they still present limitations.

In this study, we have introduced the MV-BY beamformer which takes subtle advantages over the MV beamformer by applying a Bayesian-based post-filter (i.e., the pdf coefficients) which add robustness to MV beamformer. We combined the proposed MV-BY with the WPF to formulate the MV-BY-WPF which takes advantages compared to MV-WPF.

Our proposed beamformer appears to provide the best trade-off between robustness and performance which lead to an improved contrast. Additionaly, the image brightness was retained without degrading the spatial resolution compared to the traditional MV-WPF and other CF based methods.

The WPF for adaptive processing using distortion-less beamformer (e.g., MV principle) does not affect the signal amplitude power while minimizing the noise power (NILSEN; HOLM, 2010).

Using our proposed method, improvements have been introduced in CPWC imaging system at comparable computational complexity to MV beamformer.

Particular to our proposed methodology we have found that an amount of approximately 5 emissions (i.e., the first 5 central datasets in a total of 75) using the PICMUS data available of the platform, we have reconstructed an image with quality comparable to that obtained when using a total amount of 75 emissions with DAS beamformer.

The reconstruction using simulation, phantom and human *in-vivo* dataset available on PICMUS reveal the effectiveness of our proposed beamformer in terms of array noise suppression abilities.

For simulation data S2, when DAS is compared to the MV-BY/MV-BY-WPF values in percentage (%) of 20.06/27.20 and 6.78/30.31 for CR and CNR, were respectively obtained. For phantom data PH02, 8.80/17.66 and 16.33/25.89 while for human *in-vivo* data H1, the obtained values were of 5.20/24.36 and 7.72/14.97.

An interesting outcome was observed when evaluating the human *in-vivo* data H2, where values of 9.34/17.65 and 16.18/31.79 were respectively obtained.

Additionally, the beamformed responses produced by MV-BY-WPF retains the speckle when compared to MV-WPF. It means that our proposed methodology can improve the imaging system is suggested for real applications.

6.2 FUTURE WORKS

A possible continuity with the research of the proposed methods would still be feasible. There is a wide range of works that can be investigated using adaptive beamforming methods in different US imaging modalities such as synthetic aperture imaging (SAI), photostatic imaging (PAI) and Diverging Wave Imaging (DWI) (HASEGAWA; KANAI, 2011; PAPADACCI et al., 2014, 2014).

In addition to beamforming using Plane Wave Imaging (PWI), there is the possibility of evaluating the effectiveness of the proposed method for other beamforming modality such as DWI.

The DWI has attracted the research community by allowing the real-time assessment of cardiac ultrasound data and also make possible their acquisition at a very high frame rate at the cost of highly reduced image quality (PAPADACCI et al., 2014).

REFERENCES

APPLEBAUM, S.; CHAPMAN, D. Adaptive arrays with main beam constraints. **IEEE Transactions on Antennas and Propagation**, IEEE, vol. 24, n. 5, p. 650–662, 1976.

ÅSEN, J. P. H. **Accelerating adaptive ultrasound imaging algorithms by means of general-purpose computing on graphics processing units**. Tese (Doutorado) — Norwegian University of Science and Technology, 2014.

ASL, B. M.; MAHLOOJIFAR, A. Minimum variance beamforming combined with adaptive coherence weighting applied to medical ultrasound imaging. **IEEE transactions on ultrasonics, ferroelectrics, and frequency control**, IEEE, vol. 56, n. 9, 2009.

ASL, B. M.; MAHLOOJIFAR, A. Eigenspace-based minimum variance beamforming applied to medical ultrasound imaging. **IEEE transactions on ultrasonics, ferroelectrics, and frequency control**, IEEE, vol. 57, n. 11, 2010.

BELL, K. L.; EPHRAIM, Y.; TREES, H. L. V. Robust adaptive beamforming under uncertainty in source direction-of-arrival. In: IEEE. **Statistical Signal and Array Processing, 1996. Proceedings., 8th IEEE Signal Processing Workshop on (Cat. No. 96TB10004**. [S.l.], 1996. p. 546–549.

BELL, K. L.; EPHRAIM, Y.; TREES, H. L. V. Robust adaptive beamforming using data dependent constraints. In: IEEE. **Acoustics, Speech, and Signal Processing, 1997. ICASSP-97., 1997 IEEE International Conference on**. [S.l.], 1997. vol. 5, p. 3513–3516.

BELL, K. L.; EPHRAIM, Y.; TREES, H. L. V. Robust adaptive beamforming using data dependent constraints. In: IEEE. **Acoustics, Speech, and Signal Processing, 1997. ICASSP-97., 1997 IEEE International Conference on**. [S.l.], 1997. vol. 5, p. 3513–3516.

BELL, K. L.; EPHRAIM, Y.; TREES, H. L. V. A bayesian approach to robust adaptive beamforming. **IEEE Transactions on Signal Processing**, IEEE, vol. 48, n. 2, p. 386–398, 2000.

BUSHBERG, J. T.; BOONE, J. M. **The essential physics of medical imaging**. [S.l.]: Lippincott Williams & Wilkins, 2011.

BUSKENES, J. I.; ÅSEN, J. P.; NILSEN, C.-I. C.; AUSTENG, A. An optimized gpu implementation of the mvdr beamformer for active sonar imaging. **IEEE Journal of Oceanic Engineering**, IEEE, vol. 40, n. 2, p. 441–451, 2015.

BUSKENES, J. I.; HANSEN, R. E.; AUSTENG, A. Low-complexity adaptive sonar imaging. **IEEE Journal of Oceanic Engineering**, IEEE, vol. 42, n. 1, p. 87–96, 2017.

CAPON, J. High-resolution frequency-wavenumber spectrum analysis. **Proceedings of the IEEE**, IEEE, vol. 57, n. 8, p. 1408–1418, 1969.

CHENG, J.; LU, J.-y. Extended high-frame rate imaging method with limited-diffraction beams. **ieee transactions on ultrasonics, ferroelectrics, and frequency control**, IEEE, vol. 53, n. 5, p. 880–899, 2006.

CHERNYAKOVA, T.; COHEN, D.; SHOHAM, M.; ELDAR, Y. C. imap beamforming for high quality high frame rate imaging. **arXiv preprint arXiv:1806.03526**, 2018.

COX, H.; PITRE, R. Robust dmr and multi-rate adaptive beamforming. In: IEEE. **Signals, Systems & Computers, 1997. Conference Record of the Thirty-First Asilomar Conference on**. [S.l.], 1997. vol. 1, p. 920–924.

DEYLAMI, A. M.; ASL, B. M. A fast and robust beamspace adaptive beamformer for medical ultrasound imaging. **IEEE transactions on ultrasonics, ferroelectrics, and frequency control**, IEEE, vol. 64, n. 6, p. 947–958, 2017.

DORT, S.; MUTH, S.; SWILLENS, A.; SEGERS, P.; CLOUTIER, G.; GARCIA, D. Vector flow mapping using plane wave ultrasound imaging. In: IEEE. **Ultrasonics Symposium (IUS), 2012 IEEE International**. [S.l.], 2012. p. 330–333.

EVANS, D. H.; MCDICKEN, W. N.; EVANS, D. H.; MCDICKEN, W. N. **Doppler ultrasound: physics, instrumentation and signal processing**. [S.l.]: Wiley New York:, 2000.

GARCIA, D.; TARNEC, L. L.; MUTH, S.; MONTAGNON, E.; PORÉE, J.; CLOUTIER, G. Stolt's fk migration for plane wave ultrasound imaging. **IEEE transactions on ultrasonics, ferroelectrics, and frequency control**, IEEE, vol. 60, n. 9, p. 1853–1867, 2013.

GRIFFITHS, L.; JIM, C. An alternative approach to linearly constrained adaptive beamforming. **IEEE Transactions on antennas and propagation**, IEEE, vol. 30, n. 1, p. 27–34, 1982.

HASEGAWA, H.; KANAI, H. High-frame-rate echocardiography using diverging transmit beams and parallel receive beamforming. **Journal of medical ultrasonics**, Springer, vol. 38, n. 3, p. 129–140, 2011.

HEDRICK, W. R.; HYKES, D. L.; STARCHMAN, D. E. Ultrasound physics and instrumentation. Elsevier Mosby, 2005.

HOLFORT, I. K.; AUSTENG, A.; SYNNEVÅG, J.-F.; HOLM, S.; GRAN, F.; JENSEN, J. A. Adaptive receive and transmit apodization for synthetic aperture ultrasound

imaging. In: IEEE. **Ultrasonics Symposium (IUS), 2009 IEEE International**. [S.l.], 2009. p. 1–4.

HOLLMAN, K.; RIGBY, K.; O'DONNELL, M. Coherence factor of speckle from a multi-row probe. In: IEEE. **Ultrasonics Symposium, 1999. Proceedings. 1999 IEEE**. [S.l.], 1999. vol. 2, p. 1257–1260.

HVERVEN, S. M.; RINDAL, O. M. H.; RODRIGUEZ-MOLARES, A.; AUSTENG, A. The influence of speckle statistics on contrast metrics in ultrasound imaging. In: IEEE. **Ultrasonics Symposium (IUS), 2017 IEEE International**. [S.l.], 2017. p. 1–1.

JENSEN, J. A. **Estimation of blood velocities using ultrasound: a signal processing approach**. [S.l.]: Cambridge University Press, 1996.

JENSEN, J. A. Field: A program for simulating ultrasound systems. In: CITESEER. **10TH NORDICBALTIC CONFERENCE ON BIOMEDICAL IMAGING, VOL. 4, SUPPLEMENT 1, PART 1: 351–353**. [S.l.], 1996.

LAM, C. J.; SINGER, A. C. Bayesian beamforming for doa uncertainty: theory and implementation. **IEEE Transactions on Signal Processing**, IEEE, vol. 54, n. 11, p. 4435–4445, 2006.

LI, J.; CHEN, X.; WANG, Y.; LI, W.; YU, D. Eigenspace-based generalized sidelobe canceler beamforming applied to medical ultrasound imaging. **Sensors**, Multidisciplinary Digital Publishing Institute, vol. 16, n. 8, p. 1192, 2016.

LI, P.-C.; LI, M.-L. Adaptive imaging using the generalized coherence factor. **IEEE transactions on ultrasonics, ferroelectrics, and frequency control**, IEEE, vol. 50, n. 2, p. 128–141, 2003.

LIEBGOTT, H.; RODRIGUEZ-MOLARES, A.; CERVENANSKY, F.; JENSEN, J. A.; BERNARD, O. Plane-wave imaging challenge in medical ultrasound. In: IEEE. **Ultrasonics Symposium (IUS), 2016 IEEE International**. [S.l.], 2016. p. 1–4.

LØVSTAKKEN, L. Signal processing in diagnostic ultrasound: Algorithms for real-time estimation and visualization of blood flow velocity. **Norwegian University of Science and Technology: Trondheim, Norway**, 2007.

MAGILL, D. Optimal adaptive estimation of sampled stochastic processes. **IEEE Transactions on Automatic Control**, IEEE, vol. 10, n. 4, p. 434–439, 1965.

MALLART, R.; FINK, M. Adaptive focusing in scattering media through sound-speed inhomogeneities: The van cittert zernike approach and focusing criterion. **The Journal of the Acoustical Society of America**, ASA, vol. 96, n. 6, p. 3721–3732, 1994.

MEHDIZADEH, S.; AUSTENG, A.; JOHANSEN, T. F.; HOLM, S. Eigenspace based minimum variance beamforming applied to ultrasound imaging of acoustically hard

tissues. **IEEE transactions on medical imaging**, IEEE, vol. 31, n. 10, p. 1912–1921, 2012.

MESTRE, X.; LAGUNAS, M. Á. Modified subspace algorithms for doa estimation with large arrays. **IEEE Transactions on Signal Processing**, IEEE, vol. 56, n. 2, p. 598–614, 2008.

MONTALDO, G.; TANTER, M.; BERCOFF, J.; BENECH, N.; FINK, M. Coherent plane-wave compounding for very high frame rate ultrasonography and transient elastography. **IEEE transactions on ultrasonics, ferroelectrics, and frequency control**, IEEE, vol. 56, n. 3, p. 489–506, 2009.

NGUYEN, N.; PRAGER, R. Minimum variance approaches to ultrasound pixel-based beamforming. **IEEE Transactions on Medical Imaging**, IEEE, 2016.

NGUYEN, N. Q.; PRAGER, R. W. High-resolution ultrasound imaging with unified pixel-based beamforming. **IEEE transactions on medical imaging**, IEEE, vol. 35, n. 1, p. 98–108, 2016.

NGUYEN, N. Q.; PRAGER, R. W. Minimum variance approaches to ultrasound pixel-based beamforming. **IEEE transactions on medical imaging**, IEEE, vol. 36, n. 2, p. 374–384, 2017.

NILSEN, C.-I.; HAFIZOVIC, I. Beamspace adaptive beamforming for ultrasound imaging. **IEEE Transactions on Ultrasonics, ferroelectrics, and frequency control**, IEEE, vol. 56, n. 10, 2009.

NILSEN, C.-I. C.; HOLM, S. Wiener beamforming and the coherence factor in ultrasound imaging. **IEEE transactions on ultrasonics, ferroelectrics, and frequency control**, IEEE, vol. 57, n. 6, 2010.

OZKAN, E.; VISHNEVSKY, V.; GOKSEL, O. Inverse problem of ultrasound beamforming with sparsity constraints and regularization. **IEEE transactions on ultrasonics, ferroelectrics, and frequency control**, IEEE, vol. 65, n. 3, p. 356–365, 2018.

PAPADACCI, C.; PERNOT, M.; COUADE, M.; FINK, M.; TANTER, M. High-contrast ultrafast imaging of the heart. **IEEE transactions on ultrasonics, ferroelectrics, and frequency control**, IEEE, vol. 61, n. 2, p. 288–301, 2014.

POLICHETTI, M.; VARRAY, F.; BÉRA, J.-C.; CACHARD, C.; NICOLAS, B. A nonlinear beamformer based on p-th root compression—application to plane wave ultrasound imaging. **Applied Sciences**, Multidisciplinary Digital Publishing Institute, vol. 8, n. 4, p. 599, 2018.

QI, Y.; WANG, Y.; GUO, W. Joint subarray coherence and minimum variance beamformer for multitransmission ultrasound imaging modalities. **IEEE transactions**

on ultrasonics, ferroelectrics, and frequency control, IEEE, vol. 65, n. 9, p. 1600–1617, 2018.

RITENOUR, E. R. Doppler ultrasound: Physics, instrumentation and clinical applications. **Radiology**, Radiological Society of North America, vol. 177, n. 2, p. 346–346, 1990.

RODRIGUEZ-MOLARES, A.; TORP, H.; DENARIE, B.; LØVSTAKKEN, L. The angular apodization in coherent plane-wave compounding [correspondence]. **IEEE transactions on ultrasonics, ferroelectrics, and frequency control**, IEEE, vol. 62, n. 11, p. 2018–2023, 2015.

SANDRIN, L.; TANTER, M.; CATHELINE, S.; FINK, M. Shear modulus imaging with 2-d transient elastography. **IEEE transactions on ultrasonics, ferroelectrics, and frequency control**, IEEE, vol. 49, n. 4, p. 426–435, 2002.

SHUNG, K. K. Diagnostic ultrasound. 2006.

SWILLENS, A. **A multiphysics model for improving the ultrasonic assessment of large arteries**. Tese (Doutorado) — Ghent University, 2010.

SYNNEVAG, J.; AUSTENG, A.; HOLM, S. Adaptive beamforming applied to medical ultrasound imaging. **IEEE Transactions on Ultrasonics Ferroelectrics and Frequency Control**, IEEE INSTITUTE OF ELECTRICAL AND ELECTRONICS, vol. 54, n. 8, p. 1606, 2007.

SYNNEVAG, J.-F.; AUSTENG, A.; HOLM, S. Benefits of minimum-variance beamforming in medical ultrasound imaging. **IEEE transactions on ultrasonics, ferroelectrics, and frequency control**, IEEE, vol. 56, n. 9, 2009.

SZABO, T. Diagnostic ultrasound imaging: inside out. **Access Online via Elsevier**, 2004.

SZABO, T. L. **Diagnostic ultrasound imaging: inside out**. [S.l.]: Academic Press, 2004.

SZASZ, T. **Advanced beamforming techniques in ultrasound imaging and the associated inverse problems**. Tese (Doutorado), 2016.

TANTER, M.; FINK, M. Ultrafast imaging in biomedical ultrasound. **IEEE transactions on ultrasonics, ferroelectrics, and frequency control**, IEEE, vol. 61, n. 1, p. 102–119, 2014.

TRACEY, B.; PENNINCK, D.; LEMMERHIRT, D.; POLAK, J. Robust adaptive beamforming for artifact suppression in gastrointestinal ultrasonography. In: IEEE. **Ultrasonics Symposium (IUS), 2014 IEEE International**. [S.l.], 2014. p. 1690–1693.

VOROBYOV, S. A. Adaptive and robust beamforming. In: **Academic Press Library in Signal Processing**. [S.l.]: Elsevier, 2014. vol. 3, p. 503–552.

WANG, P.; LI, N.; LUO, H.-w.; ZHU, Y.-k.; CUI, S.-g. Generalized sidelobe canceller beamforming method for ultrasound imaging. **The Journal of the Acoustical Society of America**, ASA, vol. 141, n. 3, p. 1900–1908, 2017.

WANG, S.-L.; LI, P.-C. Mvdr-based coherence weighting for high-frame-rate adaptive imaging. **IEEE transactions on ultrasonics, ferroelectrics, and frequency control**, IEEE, vol. 56, n. 10, 2009.

WANG, Y.-H.; LI, P.-C. Snr-dependent coherence-based adaptive imaging for high-frame-rate ultrasonic and photoacoustic imaging. **IEEE transactions on ultrasonics, ferroelectrics, and frequency control**, IEEE, vol. 61, n. 8, p. 1419–1432, 2014.

YI, S.; WU, Y.; WANG, Y. Esb-dmr beamforming under random matrix theory judgment principle. In: IET. **Radar Conference 2015, IET International**. [S.l.], 2015. p. 1–4.

YU, J.-L.; YEH, C.-C. Generalized eigenspace-based beamformers. **IEEE Transactions on Signal Processing**, IEEE, vol. 43, n. 11, p. 2453–2461, 1995.

ZENG, X.; CHEN, C.; WANG, Y. Eigenspace-based minimum variance beamformer combined with wiener postfilter for medical ultrasound imaging. **Ultrasonics**, Elsevier, vol. 52, n. 8, p. 996–1004, 2012.

ZENG, X.; WANG, Y.; YU, J.; GUO, Y. Correspondence-beam-domain eigenspace-based minimum variance beamformer for medical ultrasound imaging. **IEEE transactions on ultrasonics, ferroelectrics, and frequency control**, IEEE, vol. 60, n. 12, p. 2670–2676, 2013.

ZHAO, J.; WANG, Y.; YU, J.; GUO, W.; LI, T.; ZHENG, Y.-P. Subarray coherence based postfilter for eigenspace based minimum variance beamformer in ultrasound plane-wave imaging. **Ultrasonics**, Elsevier, vol. 65, p. 23–33, 2016.

ZHAO, J.; WANG, Y.; ZENG, X.; YU, J.; YIU, B. Y.; ALFRED, C. Plane wave compounding based on a joint transmitting-receiving adaptive beamformer. **IEEE transactions on ultrasonics, ferroelectrics, and frequency control**, IEEE, vol. 62, n. 8, p. 1440–1452, 2015.

ZIMBICO, A. J.; GRANADO, D. W.; SCHNEIDER, F. K.; MAIA, J. M.; ASSEF, A. A.; PIPA, D.; COSTA, E. T. Beam domain adaptive beamforming using generalized side lobe canceller with coherence factor for medical ultrasound imaging. In: IEEE. **Ultrasonics Symposium (IUS), 2017 IEEE International**. [S.l.], 2017. p. 1–4.

ZIMBICO, A. J.; GRANADO, D. W.; SCHNEIDER, F. K.; MAIA, J. M.; ASSEF, A. A.; SCHIEFLER, N.; COSTA, E. T. Eigenspace generalized sidelobe canceller combined

with snr dependent coherence factor for plane wave imaging. **Biomedical engineering online**, BioMed Central, vol. 17, n. 1, p. 109, 2018.

ZIMBICO, A. J.; GRANADO, D. W.; SCHNEIDER, F. K.; MAIA, J. M.; ASSEF, A. A.; JUNIOR, N. S.; COSTA, E. T. Joint adaptive beamforming to enhance noise suppression for medical ultrasound imaging. In: SPRINGER. **World Congress on Medical Physics and Biomedical Engineering 2018**. [S.l.], 2019. p. 233–237.

APPENDIX A – THE MV BEAMFORMER SOLUTION

In this appendix, the solution of the optimization problem to Minimum Variance (MV) beamformer or, simply, the Capon method is demonstrated. The power of a beamformer output can be expressed as in Eq. (A1).

$$f(\vec{w}) = \vec{w}^H R \vec{w} \tag{A1}$$

where R represents a real-valued symmetric matrix (i.e., the data CM). The function $f(\vec{w})$ which represents a real-valued component is subject to the constraint given by Eq. (A2).

$$\vec{w}^H \vec{a} = b \tag{A2}$$

In this context, the optimization problem can be formulated using the function $f(\vec{w})$ constrained to the equality ($\vec{w}^H \vec{a} = b$) representing $g(\vec{w})$, as in Eq. (A3) and Eq. (A4):

$$f(\vec{w}, \vec{w}^H) = \vec{w}^H R \vec{w} \tag{A3}$$

$$g(\vec{w}, \vec{w}^H) = \vec{w}\vec{a}^H + \vec{w}^H \vec{a} - 2b \tag{A4}$$

in this context, g is a dual function of f. The Lagrangian $\mathscr{L}(\bullet)$ can be expressed as in Eq. (A5).

$$\mathscr{L}(\vec{w}, \vec{w}^H, \lambda_o) = f(\vec{w}, \vec{w}^H) - \lambda_o g(\vec{w}, \vec{w}^H) \tag{A5}$$

where λ_o denotes the Lagrangian multiplier.

Inserting $f(\vec{w})$ and $g(\vec{w})$ into the Eq. (A5) we obtain Eq. (A6):

$$\mathscr{L}(\vec{w}, \vec{w}^H, \lambda_o) = \vec{w}^H R \vec{w} - \lambda_o (\vec{w}\vec{a}^H + \vec{w}^H \vec{a} - 2b) \tag{A6}$$

Therefore, taking the gradient of Eq. (A6) with respect to $\vec{w}$ we obtain Eq. (A7):

$$\nabla(\mathscr{L}) = \vec{w}_0^H R - \lambda_o \vec{a} = 0^T \tag{A7}$$

where $\nabla(\bullet)$ is the Gradient operator. The solution to the optimization problem can be represented as in Eq. (A8):

$$\vec{w}_0 = \lambda_o R^{-1} \vec{a} \tag{A8}$$

Performing appropriate substitution we obtain Eq. (A9)

$$\lambda_o(\vec{a}^H R^{-1} \vec{a}) = b \tag{A9}$$

which yields the solution to the optimization problem given by Eq. (A10)

$$\vec{w}_0 = \frac{bR^{-1}\vec{a}}{\vec{a}^H R^{-1}\vec{a}} \tag{A10}$$

If the directional constraints are set to be unitary(i.e., $b = 1$) then, the solution to the optimization problem is given by Eq. (A11):

$$\vec{w}_0 = \frac{R^{-1}\vec{a}}{\vec{a}^H R^{-1}\vec{a}} \tag{A11}$$

APPENDIX B – THE WIENER BEAMFORMER SOLUTION

In this appendix, we demonstrate the Wiener solution. In this work, it is assumed that the data is represented in terms of the Desired Signal (DS) and the additive noise plus interference components as follows ($\vec{x} = \vec{a}s_d + \vec{n}$). In order to obtain the Wiener post-filter (WPF) solution, the optimization problem of Eq. (B1) is solved in order to obtain the WPF beamformer weights as in Eq. (B1) (NILSEN; HOLM, 2010).

$$\vec{w}_{Wiener} = \arg\min_w E\left\{|s_d - \vec{w}^H\vec{x}|^2\right\} \tag{B1}$$

Using the Minimum Mean Squared Error (MMSE) criterion, the optimization problem finds the solution that minimizes cost function given by Eq. (B1) as in Eq. (B2):

$$MSE = \vec{w}^H R\vec{w} - 2s_d\vec{w}^H s_d\vec{a} + |s_d|^2 \tag{B2}$$

The solution Eq. (B3), can be obtained by taking the gradient of Mean Squared Error (MSE) to zero with respect to $\vec{w}$. This is known as the Wiener method:

$$\vec{w} = |s_d|^2 R^{-1}\vec{a} \tag{B3}$$

The MSE solution of Eq. (B3) which is extended in appendix C, defines the Wiener beamformer.

APPENDIX C – THE EXTENDED WIENER BEAMFORMER SOLUTION

In this appendix, we present the application of the Woodbury matrix in order to formulate the extended Wiener post-filter beamformer. The data Covariance Matrix (CM) components can be represented in terms of DS power and the Noise Plus Interference CM (NPICM) component as in Eq. (C1):

$$R = |s_d|^2 \vec{a}\vec{a}^H + E\{nn^H\} = |\mathrm{s}_d|^2 \vec{a}\vec{a}^H + R_n \tag{C1}$$

In Eq. (C2), the terms A, B, C and D (i.e., the factor BCD) represent the real values of an arbitrary matrix. The Woodbury matrix identity Eq. (C2), can be applied in order to accurately represent the inverted matrix

$$(A+BCD)^{-1} = A^{-1} - A^{-1}B(DA^{-1}B + C^{-1})^{-1}DA^{-1} \tag{C2}$$

Analogously, the data CM can be formulated as in Eq. (C3):

$$R^{-1} = (|\mathrm{s}_d|^2 \vec{a}\vec{a}^H + R_n)^{-1} = R_n^{-1} - R_n^{-1}|\mathrm{s}_d|^2(\vec{a}R_n^{-1} + \vec{a}^{-1})^{-1}\vec{a}^H R_n^{-1} =$$

$$= R_n^{-1} - \frac{R_n^{-1}\vec{a}\vec{a}^H R_n^{-1}}{\vec{a}^H R_n^{-1}\vec{a} + |\mathrm{s}_d|^{-2}} \tag{C3}$$

The terms of the CM, R can be inserted into the solution of the Wiener beamformer which is presented in appendix B formulated as in Eq. (B3). The Eq. (C4) and Eq. (C5) present the Wiener beamformer solution.

$$\vec{w}_{Wiener} = |s_d|^2 R^{-1}\vec{a} \tag{C4}$$

$$\vec{w}_{Wiener} = |s_d|^2 \left(R_n^{-1} - \frac{R_n^{-1}\vec{a}\vec{a}^H R_n^{-1}}{\vec{a}^H R_n^{-1}\vec{a} + |\mathrm{s}_d|^{-2}} \right)\vec{a} \tag{C5}$$

which results in Eq. (C6):

$$\vec{w}_{Wiener} = \frac{R_n^{-1}\vec{a}}{|s_d|^2 + \vec{a}^H R_n^{-1}\vec{a}} \tag{C6}$$

In appendix A it was demonstrated that the MV beamformer solution is given by Eq. (C7):

$$\vec{w}_0 = \vec{w}_{MV} = \frac{R_n^{-1}\vec{a}}{\vec{a}^H R_n^{-1}\vec{a}} \tag{C7}$$

where R_n can be used to represent R. Combining both solutions (i.e., Eq. (C6) and Eq. (C7)) we obtain Eq. (C8):

$$\vec{w}_{Wiener} = \frac{|s_d|^2}{|s_d|^2 + \vec{a}^H R_n^{-1}\vec{a}}\vec{w}_{MV} \tag{C8}$$

The MV output Power $\vec{a}^H R_n^{-1}\vec{a}$, is expressed in accordance with a predifined steering vector with directional constraints commonly set to be unitary, however, appropriate tranformations can be performed in order to obtain the MV output Power in terms of adaptive (i.e., the MV) weight vector as demonstrated in Eq. (C9):

$$\vec{a}^H R_n^{-1}\vec{a} = \vec{a}^H \frac{1}{R_n}\vec{a} = \left(\frac{1}{\vec{a}^H}\frac{R_n^{-1}\vec{a}}{R_n^{-1}\vec{a}}\right)^H \frac{1}{R_n}\left(\frac{1}{\vec{a}^H}\frac{R_n^{-1}\vec{a}}{R_n^{-1}\vec{a}}\right) = \vec{w}_{MV}^H R_n \vec{w}_{MV} \tag{C9}$$

where the factor in blue $R_n^{-1}\vec{a}$, represents a vector which is inserted in order to perform the transformations.

The wiener beamformer in Eq. (C10) can be represented in accordance with a set of adaptive weights $\vec{w}$ as follows:

$$\vec{w}_{Wiener} = \frac{|s_d|^2}{|s_d|^2 + \vec{w}_{MV}^H R_n \vec{w}_{MV}}\vec{w}_{MV} \tag{C10}$$